ANALYSIS OF ADHESIVELY BONDED COMPOSITE AEROSPACE STRUCTURES DEVELOPED BY LASER SURFACE TREATMENT

A Thesis Submitted to
the Graduate School of Engineering and Sciences of
İzmir Institute of Technology
in Partial Fulfillment of the Requirements for the Degree of

MASTER OF SCIENCE

in Mechanical Engineering

by
Kaan NUHOĞLU

June 2023
İZMİR

We approve the thesis of **Kaan NUHOĞLU**

Examining Committee Members:

Prof. Dr. Metin TANOĞLU
Department of Mechanical Engineering, İzmir Institute of Technology

---

Prof. Dr. Engin AKTAŞ
Department of Civil Engineering, İzmir Institute of Technology

---

Assoc. Prof. Dr. Mehmet SARIKANAT
Department of Mechanical Engineering, Ege University

19 June 2023

Prof. Dr. Metin TANOĞLU
Supervisor, Department of Mechanical Engineering, İzmir Institute of Technology

---

Prof. Dr. M. İ. Can DEDE
Head of the Department of Mechanical Engineering

Prof. Dr. Mustafa M. DEMİR
Dean of the Graduate School of Engineering and Sciences

ACKNOWLEDGMENTS

I would like to express my sincere gratitude and appreciation to my advisor Professor Dr. Metin TANOĞLU, for their contributions and guidance.

I would like to appreciate the entire project team, including my dear co-advisors Prof. Dr. Engin AKTAŞ and Assoc. Prof. Dr. Murat BARIŞIK, and support provider Scientific and Technological Research Council of Turkey (TUBITAK, Grant Number: 218M701).

I would also like to extend my gratitude to Turkish Aerospace Inc. (TAI) for providing materials and aerospace industry know-how.

I would like to acknowledge the support and expertise received from my friends and fellow researchers at IZTECH - Mechanical Engineering Department.

Foremost, I would like to emphasize my appreciation to my family for their unrequited support, love and belief.

ABSTRACT

ANALYSIS OF ADHESIVELY BONDED COMPOSITE AEROSPACE STRUCTURES DEVELOPED BY LASER SURFACE TREATMENT

Among the various joining techniques, adhesive bonding is a feasible alternative to mechanical fasteners to prevent incisions and discontinuity on aerospace structures. The performance of the bonded structures highly depends on the adhesion strength, which is directly related to the condition of the bonding surface. It is for this that laser surface treatment, a recently developing technique to improve bonding performance, has become suited for CFRP structures. Yet, predicting the failure strength and mechanism is vital for designing primary aircraft structures involving adhesively bonded composite structures. The scope of this paper consists of the validation and evaluation of adhesive bonding behavior in the case of joining between laser surface-treated CFRP structures, in particular, components of an aircraft wing box. To this end, both the experiment and numerical investigations of the secondary bonded coupons were examined. This study, in other words, includes experimentally revealing the bonding behavior through coupon and element-level mechanical test setups, as well as the simulation of those structures in the computer environment by performing FEA to predict the failure load and damage growth. In this regard, besides observing the effects of the laser surface treatment on the pure and mix-mode behaviors by means of the DCB, ENF, SLJ, and SSJ tests, identical specimens were numerically analyzed by utilizing macro-scale 2D and 3D models, employing the CZM technique. Meanwhile, a novel characterization study and the resulting TSL parameter identification method were achieved for an accurate numerical analysis. Eventually, in addition to the application methodology, the capabilities and appropriateness of the presented FEA method were discussed, comparing experimental and numerical results.

ÖZET

LAZER YÜZEY İŞLEMİYLE GELİŞTİRİLEN YAPIŞTIRMA BAĞLANTILI KOMPOZİT HAVACILIK YAPILARININ ANALİZİ

Çeşitli birleştirme teknikleri arasından yapıştırıcı ile birleştirme, havacılık yapıları üzerindeki çentikleri ve süreksizliği önlemesi nedeniyle mekanik bağlantı elemanlarına karşı uygun bir alternatiftir. Yapıştırma bağlantı yapıların performansı yapıştırılan yüzeyin durumuyla doğrudan ilişkilidir. Bu nedenle, yapışma bağlantı performansını iyileştirmek için son zamanlarda geliştirilen yeni bir yöntem olan lazer yüzey işleme tekniği CFRP yapılar için uygun hale gelmiştir. Fakat, kırılma mukavemetini ve mekanizmasını tahmin etmek, yapıştırıcıyla birleştirilmiş kompozit yapılar içeren uçak yapılarının tasarımı için hayati önem taşımaktadır. Bu tezin kapsamı, lazer yüzey işlemli uygulanmış CFRP yapıların, özellikle uçak kanat bileşenlerinin arasındaki yapışma bağlantı davranışının değerlendirilmesi ve doğrulanmasından oluşmaktadır. Bu amaçla, ikincil birleştirme yöntemi ile üretilmiş test kuponlarının hem deneysel hem de sayısal incelemeleri gerçekleştirilmiştir. Bu çalışma, kupon ve eleman düzeyinde mekanik test düzenekleri ile yapışma davranışının deneysel olarak ortaya konulmasının yanı sıra, bu yapıların sonlu elemanlar analizi sayesinde bilgisayar ortamında simüle edilmesi sonucunda hasar yükünün ve büyümesinin tahmin edilmesini içermektedir. Bu bağlamda, DCB, ENF, SLJ ve SSJ testleri ile lazer yüzey işleminin sade ve karışık mod davranışlar üzerindeki etkilerinin gözlemlenmesinin yanında, makro ölçekte 2D ve 3D modeller kullanılarak ve CZM tekniği sayesinde mekanik testlere özdeş geometriler sayısal olarak analiz edilmiştir. Bu esnada, yenilikçi bir karakterizasyon çalışması ve ortaya konulan TSL parametre tanımlama yöntemi sayesinde sayısal analiz başarılı bir şekilde beslenmiştir. Sonuç olarak, uygulama metodolojisine ek olarak, deneysel ve sayısal sonuçların karşılaştırılması ile uygulanan sonlu elemanlar yönteminin yetenekleri ve uygunluğu tartışılmıştır.

TABLE OF CONTENTS

LIST OF FIGURES

Figure **Page**

Figure **Page**

Figure **Page**

Figure **Page**

LIST OF TABLES

Table **Page**

LIST OF SYMBOLS AND/OR ABBREVIATIONS

CFRP	Carbon Fiber Reinforced Plastic
FEA	Finite Element Analysis
CZM	Cohesive Zone Modeling
TSL	Traction Separation Law
SLJ	Single Lap Joint
SSJ	Skin-Spar Joint
IR	Infrared
EPFM	Elastic-Plastic Fracture Mechanics
DIC	Digital Image Correlation
LST	Laser Surface Treated
LSUT	Laser Surface Untreated
DCB	Double Cantilever Beam
ENF	End Notched Flexure
MBT	Modified Beam Theory
CC	Compliance Calibration
NLPQL	Nonlinear Programming by Quadratic Lagrangian
CCD	Central Composite Design
DOE	Design of Experiments
IR	Infrared
VCCT	Virtual Crack Closure Technique
XFEM	Extended Finite Element Method
SEM	Secondary Electron Microscope
T_n^{max}	Maximum Tangential Cohesive Traction
T_t^{max}	Maximum Tangential Cohesive Traction
G_{IC}	Mode I Critical Strain Energy Release Rate
G_{IIC}	Mode II Critical Strain Energy Release Rate
k_I	Mode I Cohesive Stiffness
k_{II}	Mode II Cohesive Stiffness
d	Artificial Damping Coefficient
l_e	Cohesive Zone Mesh Size

l_{cz}	Cohesive Zone Length
δ_t^{max}	Mode I Maximum Cohesive Separation
δ_n^{max}	Mode II Maximum Cohesive Separation
P_{max}	Maximum Load
L	Bond Line Length
W	Bond Line Width
P	Load
δ	Crosshead Displacement
b	Specimen Width
a	Delamination Length
a_0	Initial Crack Length
m	Slope

CHAPTER 1

INTRODUCTION

Composites are, fundamentally, materials that are made from a combination of two or more different materials to create a new material with empowered properties, and often used in the aerospace, automotive, and construction industries since they offer several advantages over traditional materials, e.g., increased strength and durability, lightweight and resistance to corrosion [1]. Composite materials are used in various products, from aircraft wings and car bodies to golf clubs and tennis racquets; they are also used in military applications, such as bullet-proof vests [2]. The main reason makes composite materials a superior choice is that the mechanical or thermal properties of composites can be tailored to the specific needs of the application by varying the type and amount of the constituent materials [3].

Composite materials have been used in the aerospace industry for many years and are becoming increasingly popular in the application of aircraft components [4]. In particular, carbon fiber reinforced plastic (CFRP) composites are the most used ones in the constructions of fuselages and wings as they are much lighter than metals, such as aluminum or several alloys [5]. The use of composite materials in aircraft bodies is expected to grow in the future, as new technologies are developed to make use of their unique properties with relatively effortless manufacturing [67].

Adhesive bonding is a process in which two or more materials are joined together by an adhesive, which may be in the form of a liquid, gel, or film, and is typically applied to one or both surfaces and solidified to be joined [8]. It is a versatile joining method that can be used to join a variety of similar or dissimilar materials, including metals, plastics, and composites, on top of that, it offers many benefits over mechanical fastening. With the widespread use of composite materials, adhesive bonding has become a reliable joining technology in the aerospace industry since adhesive bonds are capable of withstanding the extreme temperatures and pressures encountered during flight; additionally, adhesive bonding is also resistant to vibration and shock [9,10].

Surface treatments are an important part of the adhesive bonding process. There are a variety of surface treatments that can be applied to surfaces prior to adhesive bonding in order to improve the bond strength [11,12]. Surface treatments can be divided into two main categories: physical treatments and chemical treatments. Physical treatments include roughening the surface with sandpaper or a grinding wheel in order to create microscopic irregularities that the adhesive can grip onto. Another physical treatment is plasma treatment, which uses high-energy plasma to modify the surface of the material to both remove the contaminations and create a rough surface. This treatment is often used on plastics and metals, and can improve the bond strength of both adhesive and welds. Chemical treatments typically involve cleaning the surface to remove any contaminants that could interfere with the bonding process, which can be done with solvents, detergents, or abrasive cleaners [13,14]. As an innovative new method, the laser surface treatment technique is being used to create a rough surface consisting of bare fiber strands, removing the matrix materials on top without damaging the fibers [15,16].

Several factors can affect the performance of adhesively bonded joints, such as the bond line thickness, the surface roughness of the substrates, and the cure temperature of the adhesive [17,18]. Adhesive bonded structures are being experimentally investigated by performing various joint configurations in different scales, e.g., single lap joint (SLJ), T joint, etc., in order to evaluate the performance of the bonding [19,20]. On the other hand, numerical analysis of the bonding behavior is being executed using analytical methods or employing Finite Element Analysis (FEA) technique in order to predict the failure strength and mechanism [21–23]. FEA provides a powerful tool for understanding and optimizing the performance of adhesively bonded joints. In the literature, among the various FEA techniques, the cohesive zone modeling (CZM) technique, a branch of damage mechanics, become the most widely used one due to providing several advantages over the continuum and fracture mechanics approach-based ones. In the CZM technique, one can simulate the bonding behavior by means of the relation between traction and corresponding separation between adjacent surfaces, which is also called traction separation law (TSL) [24–27].

1.1. Objective and Approach

This thesis's objective consists of validating and evaluating the adhesive bonding behavior of the laser surface-treated carbon fiber reinforced plastics (CFRP) composite aircraft structures via using finite element technique to perform conservative prediction of the failure load and damage growth. The specific objectives are as follows;

- Performing mechanical analysis of the adhesively bonded aerospace structures in coupon and element test setups.
- Executing experimental investigation of the adhesively bonded skin-spar relation in aircraft wing-box.
- Investigating the effects of the laser surface treatment application on the adhesive bonding behavior of CFRP structures.
- Numerically simulating the adhesively bonded CFRP aerospace structures.
- Developing an innovative and successful finite element analysis methodology to examine the aircraft components' bonding behavior.
- Characterizing the adhesive bonding under both mode I and mode II behavior for different surface conditions.
- Revealing the behavior of leaser surface treated parts by transferring the effects of treatment application to finite element analysis.
- Employing the CZM technique in order to perform accomplished simulations of the crack initiation and propagation in the bonding areas.
- Developing compatible analysis methods for the different scale investigation of the adhesively bonded aircraft components.

Such objectives above are overcome by executing both experimental and numerical analyses of the secondary bonded CFRP parts using structural adhesive. In this regard, this thesis includes, in the first place, general information about bonded aircraft structures and the implementation of several surface treatment methods, on top of that, existing numerical analyzing techniques to validate the behavior of the composite bonded joints. For the exact purpose of the conservative prediction of crack initiation and damage growth on different level specimens, subsequently, two different level bonded joint tests,

which are Single Lap Joint (SLJ) and Skin-Spar Joint (SSJ) tests are investigated. Given that, 3D FEA of aforementioned specimens has been developed, using the CZM method to achieve effective and relatively effortless failure analysis. As the particular exigency of this circumstance, DCB and ENF tests are, too, executed in order to introduce the CZM parameters for specific surface conditions; thus, both the chemical and mechanical contribution of laser surface treatments to the bonding performance is transferred to the FEA.

1.2. Outline

In the continuation of Chapter 1, where a general introduction to the processes and scientific foundations carried out in this study is made, the main sections that form the basis of this thesis stars with Chapter 2, which states detailed research regarding fundamental concepts and relevant literature covering the main topics of this study, e.g., adhesive bonding, composite joint bonding methods, surface preparation, failure analysis of the adhesive bonded joints, cohesive zone modeling. In the continuation, experimental works covering laser surface treatment, manufacturing the adhesively bonded specimens, and experimental results have been given in Chapter 3. Thereafter, as one of the most critical parts of the present study, bonding characterization works have been covered under a separate heading in Chapter 4. In the literature, though being quite crucial, the determination of the CZM parameters for a specific condition is often skipped by assumptions; therefore, the characterization part have evaluated under a main heading to show the quality and comprehensiveness of the present study. Then the thesis structure continues with Chapter 5, which states the applied finite element analysis methodology - the primary focus of this study. In this chapter, examined numerical analysis technique for the adhesively bonded and laser surface treated composite coupon and element level setups has been given in detail; meanwhile, created 3D orthotropic composite models and implementation of the CZM technique in the specimens have been given in this chapter. Afterward, Chapter 6 gives the results of the presented FEA methodology while stating the force-displacement, stress distributions, maximum strength values and comparisons of the experimental and numerical results. Then finally, this thesis ends with conclusions and recommendations in Chapter 7.

CHAPTER 2

FUNDAMENTAL CONCEPTS AND RELEVANT LITERATURE

In this chapter, comprehensive literature research is conducted on the cognition of adhesively bonded composite aircraft structures and bonding performance improvement techniques such as surface treatment. Besides concerning fracture mechanics basics and theories regarding the failure of composite materials, numerical analysis techniques to predict damage initiation and propagation on the bonded surfaces are clarified further. On top of that, the reason behind choosing the laser surface treatment process to enhance the joint performance and selecting the Cohesive Zone Modelling (CZM) technique to perform numerical simulations of the bonded composite joints is explained in detail.

2.1. Adhesive Bonding

The main definition of adhesive bonding is the joining of substrates, known as adherents, by means of an adhesive material that creates a bond between the surfaces [9]. Adhesive bonding, essentially, provides transferring load from one part to another, which lend helps to abolish stress concentrations caused by fastener holes; thus, ensuring the spreading of the load evenly over the joint makes it fairly superior over the mechanical fasteners, such as bolting and riveting [28]. Rather than relying on the melting and fusing of the parts as with welding, adhesive bonding joints use a bulk adhesive material to stick two or more structures together. The bonding phenomenon forms between the two phases, also called the interphase region, with two main mechanisms: chemical bonding and mechanical interlocking [29,30]. The bonding can also be described as the mutualist combination of the primary and secondary chemical bond formation and interlocking mechanism between adhesive and rough bonding surfaces, illustrated in Figure 1 [31].

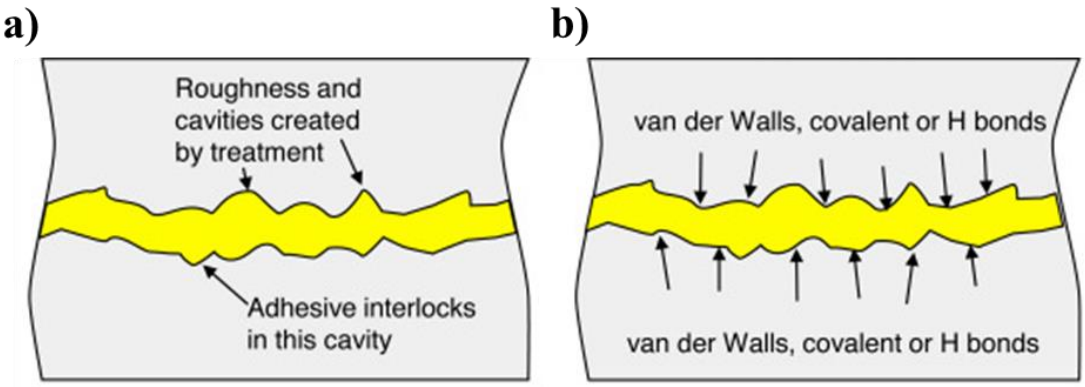

Figure 1.a) Mechanical interlocking, b) chemical bonding mechanisms (Source: A. Yudhanto et al., 2021 [31]).

Adhesive joining could certainly enable the reduction of the number of mechanical fasteners; therefore, the adhesive bonding technique, largely, the greatest option for light weighting a compound structure while joining both similar and dissimilar metals and composites, such as steel, magnesium, plastic, aluminum and carbon fiber reinforced plastics (CFRP) [8,32]. Apart from preventing stress concentration and aiding in weight reduction, many more advantages and disadvantages of the adhesive joining over the mechanical fasteners are summarized in Table 1.

Table 1. Comparison of mechanical fastening and adhesive bonding.

Advantages	Disadvantages
Mechanical Fastening	
• No special surface preparation needed or ultra-clean handling operations. • Strength not adversely or irreversibly affected by thermal cycling or high • Presents no unusual inspection problems for joint quality. • Can be disassembled easily, without destruction of the adherends.	• Machining of holes in the composite, so weakening the part. • Concentrates stress on the bearing surfaces, causing 'stress-raisers' that can initiate failure. • Not generally as strong as bonded joints unless joining thick laminates. • Increases the weight of the assembled structure, reducing joint efficiency. • Honeycomb selection is often dictated by fastener sizes. • Protruding fasteners can disrupt aerodynamic surfaces.
Adhesive Bonding	
• Distributes load over a larger area than mechanical joints, reducing average stress and stress concentration. • Machining in joint area can be avoided, so the adherends are not weakened. • Minimises added weight to structure. • After first loading, bonded joints show less permanent set than equivalent mechanical joints. • Good elevated temperature creep resistance with correct adhesive selection. • Enables design of smooth external (aerodynamic) surfaces. • Creates integrally sealed joints with low sensitivity to crack propagation. • Large areas of bonded joints are often less costly than mechanical joints. • Enables assembly of dissimilar materials prone to galvanic corrosion, given consideration of any differences in thermal expansion (thermal stresses).	• More difficult to inspect completely by non-destructive testing (NDT). • Careful design needed to eliminate peel loadings. • Accurate mating of adherends needed to give efficient structural bonds. • Permanent - not easily disassembled. Thermal cycling and high humidity can affect the strength. • Special surface preparation needed and clean handling prior to bonding.

2.2 Adhesive Bonding in Aerospace Industry

It is nearly beyond the bounds of possibility that design and produce any transportation vehicle, which moves whether on the ground, water or air, that does not involve a sort of a joint. Joints are, generally, take place in transition between not only primary structures but also minor parts attached to the main body. Due to the inherently being a large structure, an aircraft body is, essentially, manufactured from the joining of many relatively smaller elements, e.g., stringers, ribs, spars, clips, etc., that become the primary aircraft structures such as wing and fuselage [33–35]. A typical military aircraft wing structure, including spar and rips, is illustrated in Figure 2.

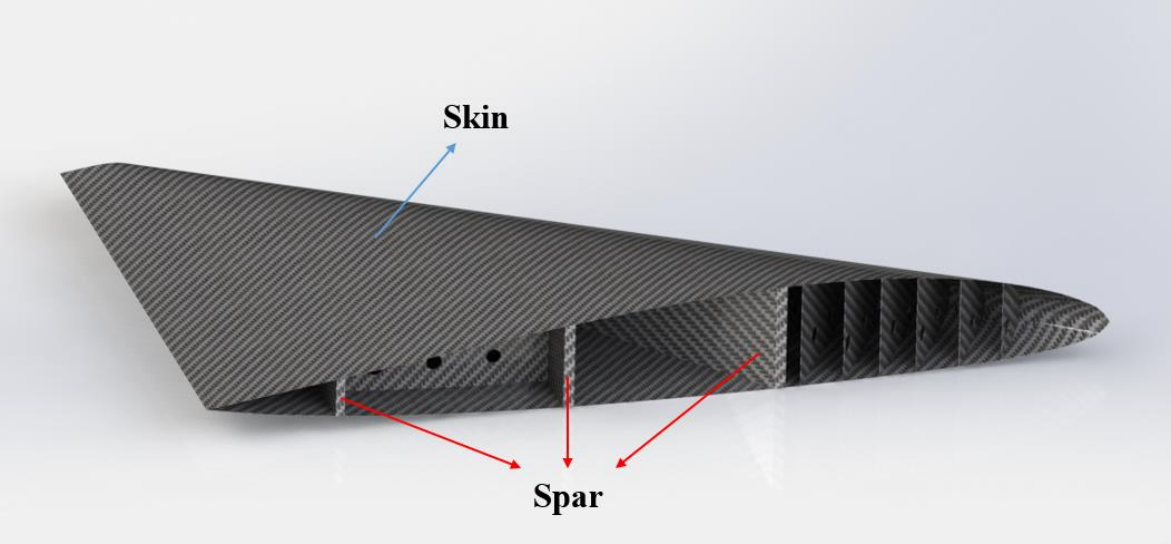

Figure 2. Illustration of a typical military aircraft wing-box.

Aircraft have evolved over time, creating new ways to bond and fasten structural parts together. Despite the fact that mechanical fasteners are still used, the demand for adhesive joining has grown significantly due to the design flexibility and reduced weight in composite primary and secondary structural assemblies [10]. Nowadays, whit the widespread use of new and modern materials, especially composites, adhesives have become highly considerable for aircraft design engineers. Figure 3 shows the primary structural parts manufactured with the adhesive joining technique in the SAAB 340 aircraft [36].

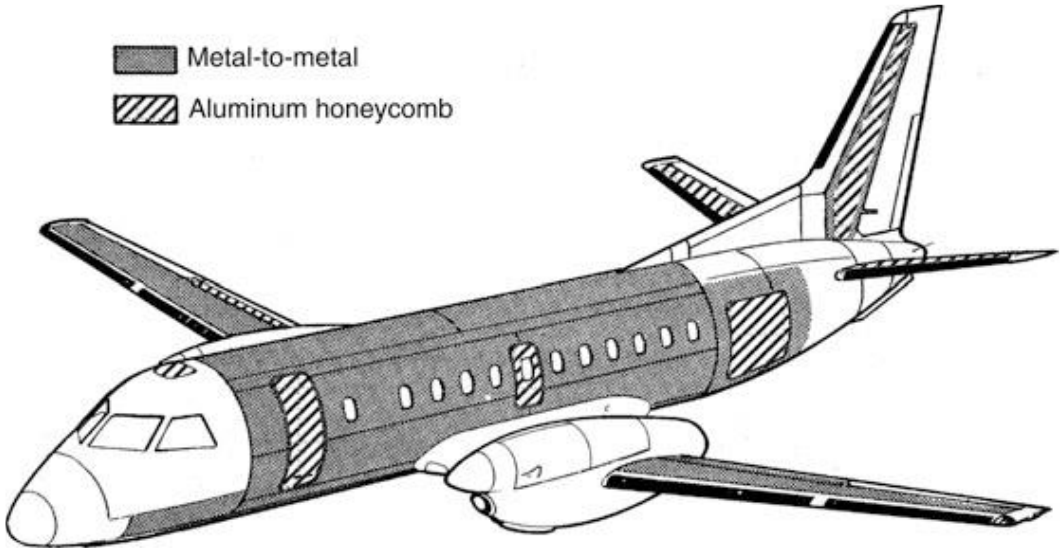

Figure 3. Adhesive bonded structures of SAAD 304 (Source: Hart-Smith al., 2019 [36]).

To give an example of the utilization and advantages of adhesive bonding in aircraft structures, Figure 4.a. illustrates the comparison of the stiffening effects of bonded and riveted joints, particularly skin and spar confection and Figure 4.b. shows the comparison of the formed stress distributions around the bonded and fastening area of the adhesive bonded and riveted assemblies; the changing of the stress distribution and consisted stress concentration around the hole can also be clearly seen in Figure 4 [36].

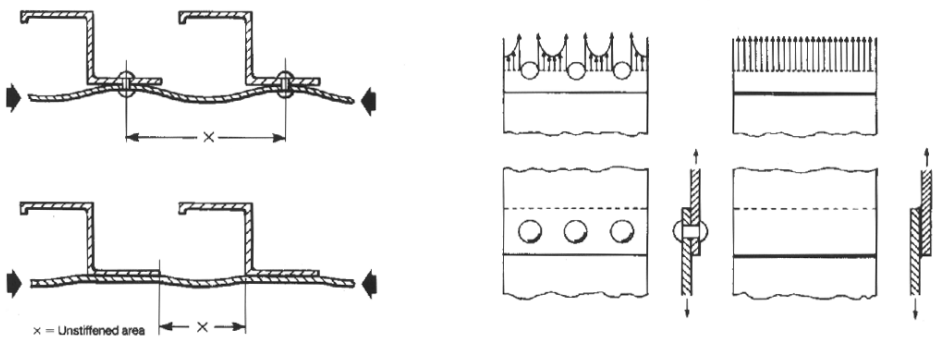

Figure 4. a) Comparison of the stiffening effects of bonded and riveted joints, b) comparison of the formed stress distributions of the bonded and riveted assemblies (Source: Hart-Smith et al., 2011 [36]).

2.2.1. Adhesive Bonded Joints

In aerospace applications, in order to investigate structural behaviors of the aircraft components step by step, the building block approach has become an essential technique, which uses a pyramid concept ranging from coupon level to full-scale structure (Figure 5) [36]. This approach, basically, provides confidence and efficiency to the engineers while designing both primary and secondary structures, due to its progress with the knowledge gained at each level [37].

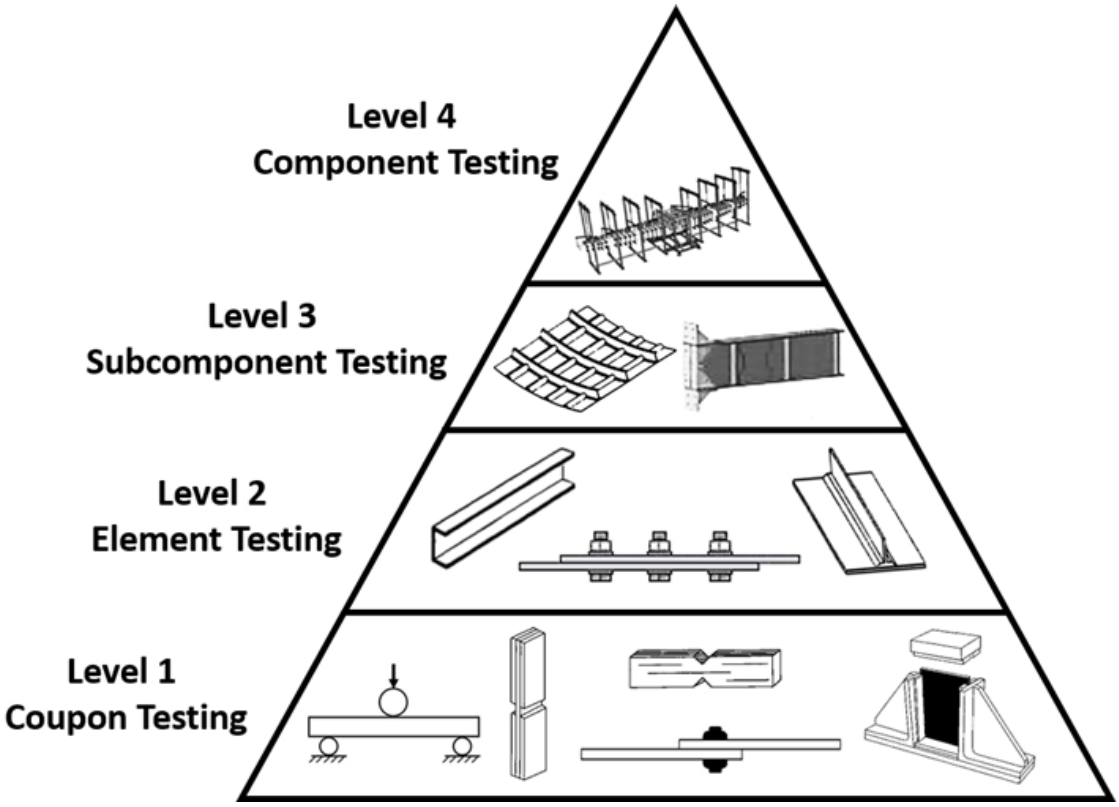

Figure 5. Building block approach for aerospace applications (Source: K. R. Hamm et al., 2022 [37]).

In the literature and aerospace industry, in order to test adhesive bonded structures at the coupon level, several types of bonded joint types are being used [38,39]. Each joint type is devised to evaluate the bonding behavior under the varied load cases. Figure 6 states the schematic illustration of the main coupon-level adhesive joint types found in

the literature [40]. Between those types, Single Lap Joint (SLJ) configuration enables the observation of both peel and shear stress together and provides simplicity; therefore, SLJ is the most commonly analyzed one in the literature [41].

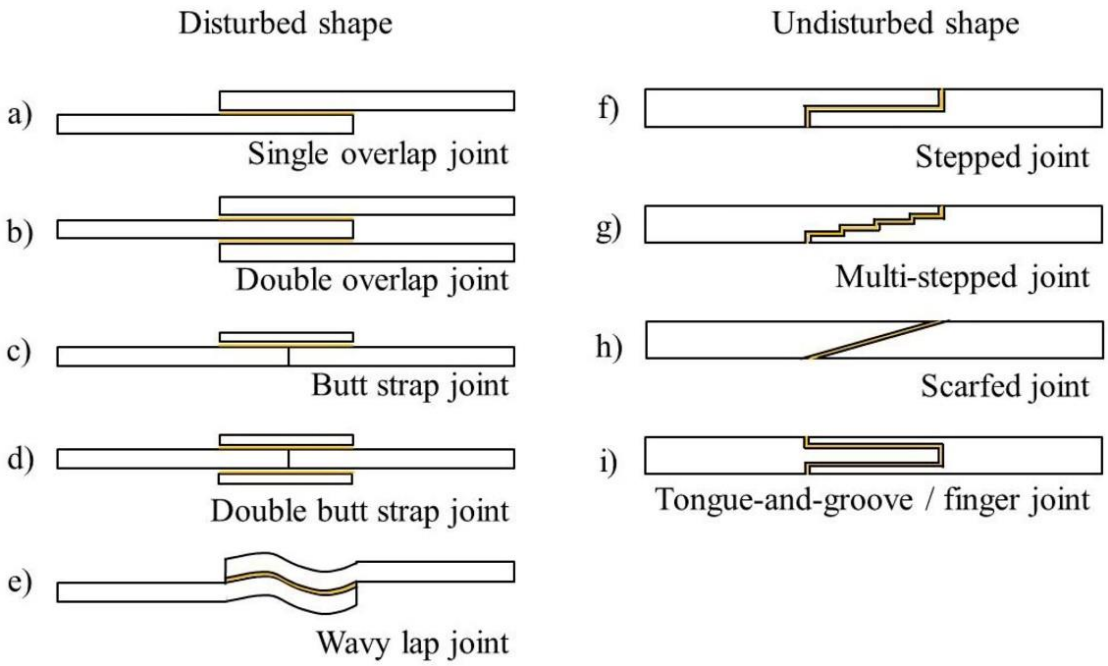

Figure 6. Coupon level adhesive joint types (Source: T. Ribeiro et al., 2016 [41]).

Additionally, there is also a considerable variety of different types of adhesively bonded joints at the element level, designed for the exact purpose of investigating adhesive bonding performance under both pure and compound loading scenarios. Figure 7 states the different types of element-level adhesive bonding joint configurations. In the aerospace wing-box components testing applications, which is the scope of this study, T joints are the most often used ones in order to investigate, in particular, skin-stiffener and skin-spar interactions [42].

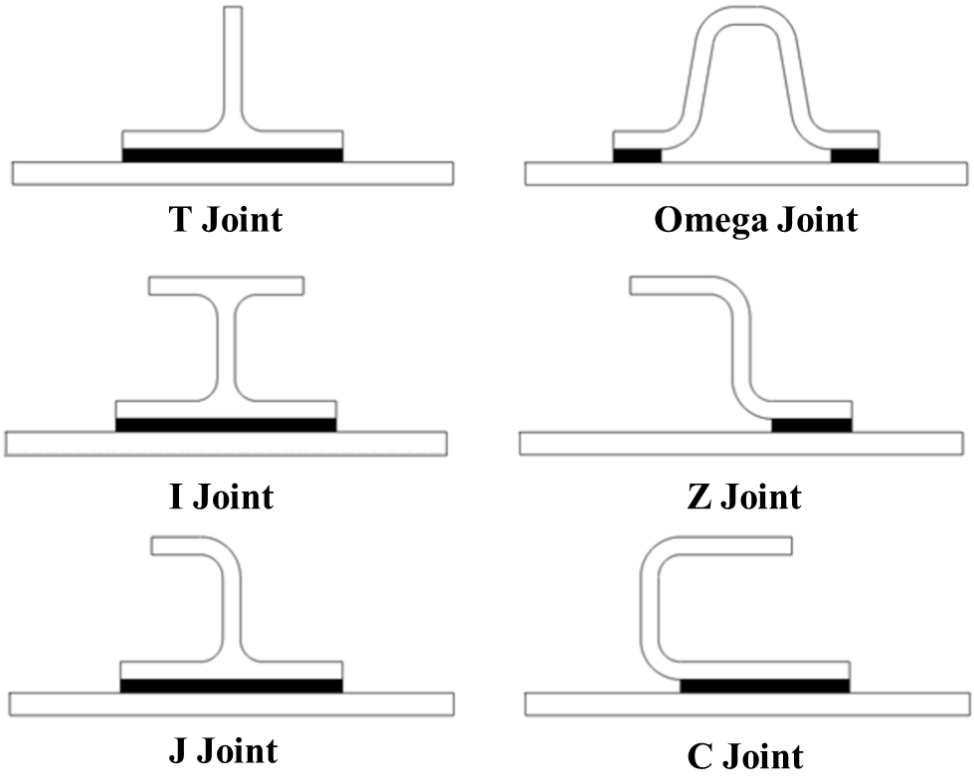

Figure 7. Element-level adhesive bonding joint types (Source: L. Zhou et al., 2016 [42]).

2.3. Composite Joint Bonding Methods

Composite materials, particularly CFRP composites, can be joint with mainly three different manufacturing methods: Co-curing, Co-bonding, and Secondary bonding [43]. The main factor that creates the difference between these methods is the curing order of the composite substrates and the adhesive material. If the bonding of the two composite parts is provided by curing composite parts and adhesive together, it is called Co-cure [44]. The co-curing method has several advantages, e.g., manufacturing complex composite geometries at one stage, which reduces process time. The second method is Co-bonding, which involves the joint of two cured and uncured substrates, curing them together with adhesive material. The last method is Secondary Bonding, which is the most used one in both industry and literature [45,46]. It is basically joining the pre-cured composite substrates, just curing the adhesive in between. A summary of the different joining methods and schematic illustration can be found in Figure 8 [47].

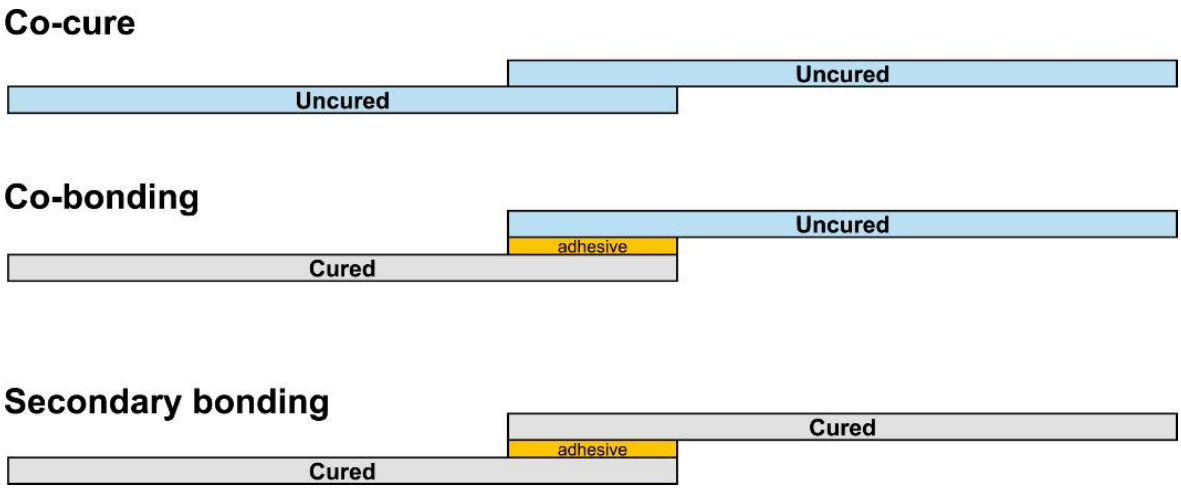

Figure 8. Schematically illustration of the joining methods (Source: S. Lim et al., 2020 [16]).

2.4. Surface Preparation

The most important step of manufacturing adhesive bonded structures is surface preparation prior to the joining [48]. The conditions of the adjacent surfaces, unfortunately, play a vital role in the bonding performance and can completely change the behavior of the adhesive structures under different operating conditions. In this regard, one can enhance the surface of the substrates in order to improve bond strength, which allows the bonded structure to withstand higher loads without failure [30]. In the industry and literature, there are three main methods in order to provide that: The first one is removing contaminants from the surface and the second is to roughen the surface using abrasion, and the third is increasing surface energy employing special treatment methods. [483015].

Grease, oil or contaminants are removed from the surface of the substrates using a suitable solvent such as isopropyl alcohol, methyl ethyl ketone, acetone [49]. The surface shall be degreased and cleaned before and after any other treatment method to remove contaminants. One can utilize abrasion on the surface of the substrates in order to increase surface roughness, which leads to better wetting, on top of that, provides a mechanical key for the adhesive material. To achieve that, either grit blasting or sanding to roughen the adjacent surfaces, and the selection of the method mainly depend on the material characteristics of the substrates to be bonded. For plastics whit a low surface energy, it may be necessary to modify the surface chemistry to better adhesion. On the other hand,

plasma and corona treatments work by increasing the surface energy of the substrates, which makes it easier for the adhesive to fully wet the surface and form an integral bond line [5051]. Some very low surface energy plastics may not respond well to plasma treatment; one shall use several specialist chemical surface treatments, such as acids or bases, in order to achieve surface activation for the adhesive bonding [52]. Figure 9 schematically illustrates the effects of the various surface treatment methods on the CRPF substrates [53].

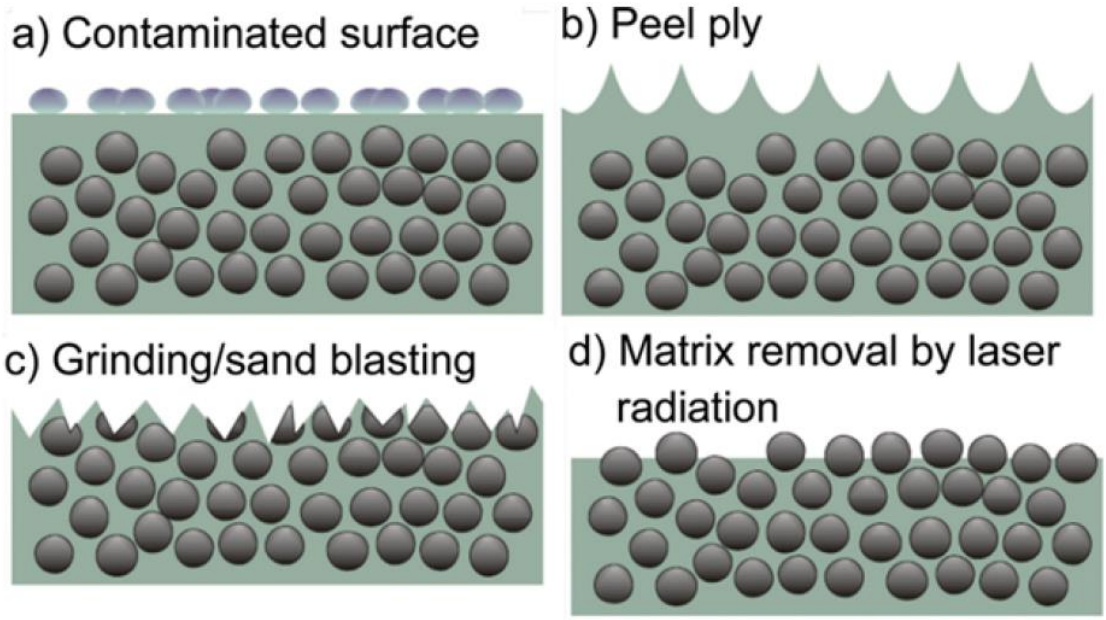

Figure 9. Effects of the various surface treatment methods on the CRPF substrates (Source: F. Fischer et al., 2012 [53]).

The selection of an appropriate surface treatment should be based on considerations such as substrate materials, the manufacturing process and method, performance requirements, workplace environments and safety factors.

Laser surface treatment is a cutting-edge method for processing materials that shows great promise in adhesive bonding of carbon fiber reinforced polymer (CFRP) structures. By means of focusing high-energy produced by laser beams on specific locations, this technique removes contaminants from the surface and increases roughness in order for stronger mechanical interlocking [54]. At the point where today's laser technologies have come, the amount of heat transferred by the laser beam to the desired

location of the surface can be controlled by many different parameters, such as laser power, pulse width, wave length [55,56].

In the literature an industry, various types of laser surface treatment methods and equipment are being used, which are suitable for particular applications and materials [57,58]. For instance, as the earliest type of laser treatment technique, CO_2 lasers have prevalent use in order to modify the surface of polymer-based composite materials. Instead, Ultra Violet (UV) lasers are, on the other hand, being used to remove the top matrix layer; surface contaminations can also be removed in this way. Yet, having high application and equipment cost makes UV laser technique less preferable among the other laser surface treatment methods [59]. As an alternative, due to their being time and cost efficient, infrared (IR) lasers attract engineers' attention to use on the fiber reinforced polymer (FRP) composites [60–62]. Still, process parameters must be determined and optimized for the specific substrate materials and surface conditions to remove the polymer matrix section without damaging the fiber strands. Figure 10 illustrates the application of the IR laser surface treatment technique on the CFRP campsite material [63].

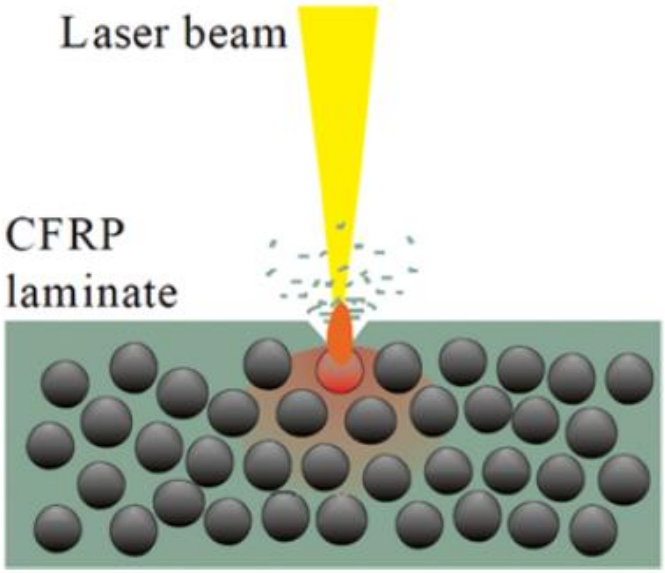

Figure 10. Application of the IR laser surface treatment technique on the CFRP campsite (Source: F. Fischer et al., 2012 [53]).

2.5. Adhesive Bonded Joints Failure Types

Adhesive bonded FRP composite joints can fail in various modes; according to the ASTM D5573 standards [64], failure is observed, fundamentally, in seven different types: adhesive failure, cohesive failure, thin-layer cohesive failure, fiber tear failure, light-fiber tear failure, stock-break failure, and mixed failure. Figure 11 represents the schematic illustration of the adhesive bonding failure modes on the FRP SLJ geometry [43].

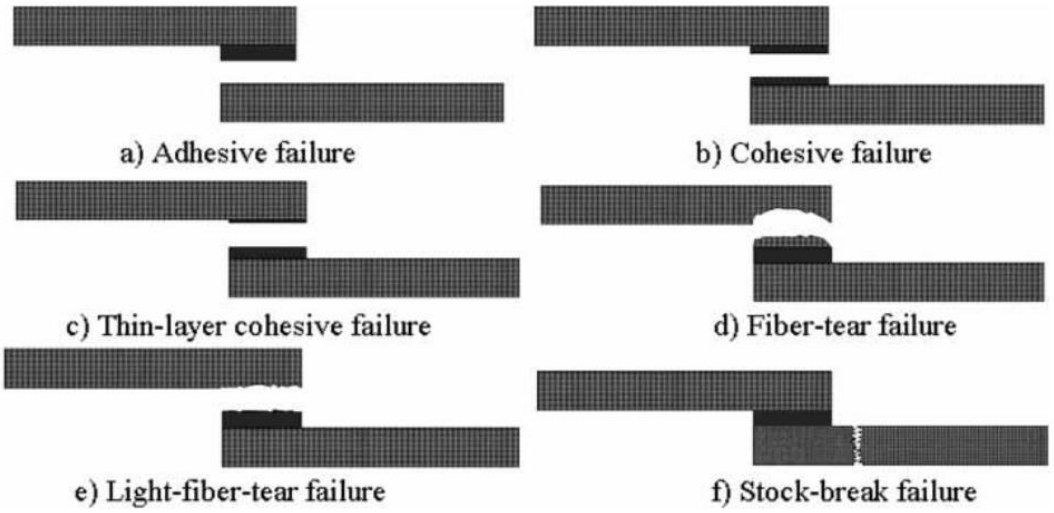

Figure 11. Schematically illustration of the adhesive bonding failure modes (Source: S. Budhe et al., 2017 [43]).

One can summarize the failure modes, basically, under three main headings: Cohesive Failure, Adhesive Failure and Adherent Failure [65]. First, if the failure occurs within the adhesive itself, it is called cohesive failure. This failure mode is often observed due to the relative weakness of the adhesive material over the substrates. The second major one is adhesive failure, which is debonding between the adhesive and substrate interface. It commonly happens because of erroneous joint producing, insufficient surface cleaning or inappropriate adhesive selection. Lastly, if one of the bonded materials fails outside the joint, it is called adherent failure. In that scenario, the failure strength of the adhesive and bond is greater than the substrates; therefore, when stress is applied, substrates break earlier than the bonds. Given that, it depends on largely strength of the

adherent material, in addition, this failure behavior is mostly seen in the composite materials as interlaminar failure or delamination. There are, on top of that, slightly more complex cases, e.g., cohesive fracture very near the interface or fracture jumping from one interface to the other, which are called mix-failure mode [43,44].

2.6. Failure Analysis of the Adhesive Bonded Joints

Fundamentally, it is desired by structural design engineers that the adhesive bonded structures in any construction shall withstand static or cyclic loads without any damage in line with the requirements determined [66]. In addition to the safety considerations, optimum material usage has enormous vitality in order to reduce the weight and cost of the structure; in other words, using reliable design methodologies by predicting the limits of the structure provides efficiency. Therefore, it is curial to determine the strength limits of the structure with testing, in particular, analyzing the bonded components prior to manufacturing [67]. There are, obviously, two main methods in order to mathematically analyze the adhesive bonded structures: Analytical analyzing methods and numerical analyzing methods. The earliest work about analyzing adhesive bonded structures was done by Volkersen [68] in 1938 by means of ordinary governing equations to solve simple differential equations and assuming adhesive and adherents are linear elastic. Yet, due to the nonlinear behavior and anisotropy, the analytical analysis of the adhesive bonded joints becomes quite complicated when working with composite substrates. In such conditions, as a numerical analysis method, the FEA technique is quite suitable and frequently used [21,23]. As of the author's knowledge, one of the first research on numerical analysis of the adhesive bonded structures via using the FEA technique was conducted by Adams et al. [69–72].

Today, the FEA of the adhesive bonded joints have formed within the framework of three different branches of mechanics: Continuum Mechanics, Fracture Mechanics and Damage Mechanics. In the following, general information and consideration of the three main branches, additionally, the comparison of them is given.

2.6.1. Continuum Mechanics Approach

Between the FEA methods for the analysis of the bonded structures, the relatively basic and most widely used one is the Continuum Mechanics approach [73]. In this method, after the find out the stress and strain distributions, failure prediction is done by comparison of the maximum allowable stress and strain values of the material or exploiting different failure criteria, e.g., Maximum principal stress theory, Tsai–Hill failure criterion [74]. In this approach, in other words, there is no separation observed between adjacent surfaces since the whole structure is continuous.

Adams et al. [75] have successfully used the continuum mechanics method to FEA of the joint strength and failure prediction. Lee and Lee [76] have analyzed adhesive bonded tubular single lap joint with steel-steel adherend by comparing occurred maximum shear stress and adhesive material maximum bulk shear strength. Silva et al. [77–79] demonstrated from both the numerical and analytical analysis of the Single Lap Joint geometry that maximum shear stress criteria is merely effective while using brittle adhesive materials. Given that, stress based failure criteria are unsuitable for the analysis of the ductile adhesive material since bonds can withstand higher loads even if the adhesive part yields. Therefore, Hart-Smith and Adams [8081] utilized the maximum principal strain criteria for a ductile adhesive material to analyze bonding behavior; those studies show that strain-based criteria are more appropriate than the stress-based ones to analyze ductile adhesives. In addition, Zhao et al. [82,83] used a criteria based on the strain energy, which is the area under the stress-strain curve, and showed that it is one of the most convenient methods due to the utilization of both stress and strain components.

In the continuum mechanics approach, due to the assuming the body is continuous and perfectly bonded, sharp edges formed at the corners of the overlap region create singular points involving infinite stress or strain values, also called stress and strain singularity points; thus, FEA cannot give results at these points [84]. Figure 12 shows stress distribution at the corner of the overlap region in a precracked and non-precracked cases derived by the continuum mechanics approach [84]. As can be seen, instead of being finite, σ_y values are infinite at the crack initiation point, which become stress discontinuities at the crack tip.

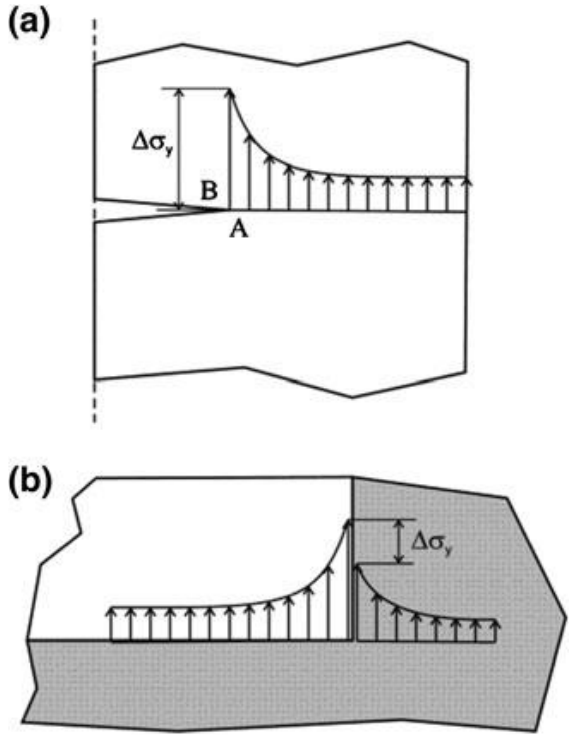

Figure 12. Stress distribution at the corner of the overlap region in a a) precraced and b) non-precracked cases (Source: F. J. P. Chaves et al., 2013 [84]).

2.6.2. Fracture Mechanics Approach

Generally, Fracture mechanics deals with crack initiation and propagation in a material. In contrast with Continuum Mechanics, a method that design procedures based on only various maximum stress criterias, fracture mechanics determines failure based on the interaction between the applied energy and formed crack, using methods based on solid mechanics [9]. Instead of the magnitude of stress or strain, fracture mechanics is concerned primarily with the distribution of stresses and displacements in the vicinity of a crack tip. Fracture mechanics is suitable in order to analyze the failure of brittle materials under certain circumstances. In this way, the crack would grow under applied stress until it encounters the complete fracture; the fracture criterion involves only a material parameter related to the near-tip stress field and energy of the structure [85]. There are three different ways that fracture can occur: Mode I, Mode II, and mode III, which are called fracture modes and schematically represented in Figure 13.

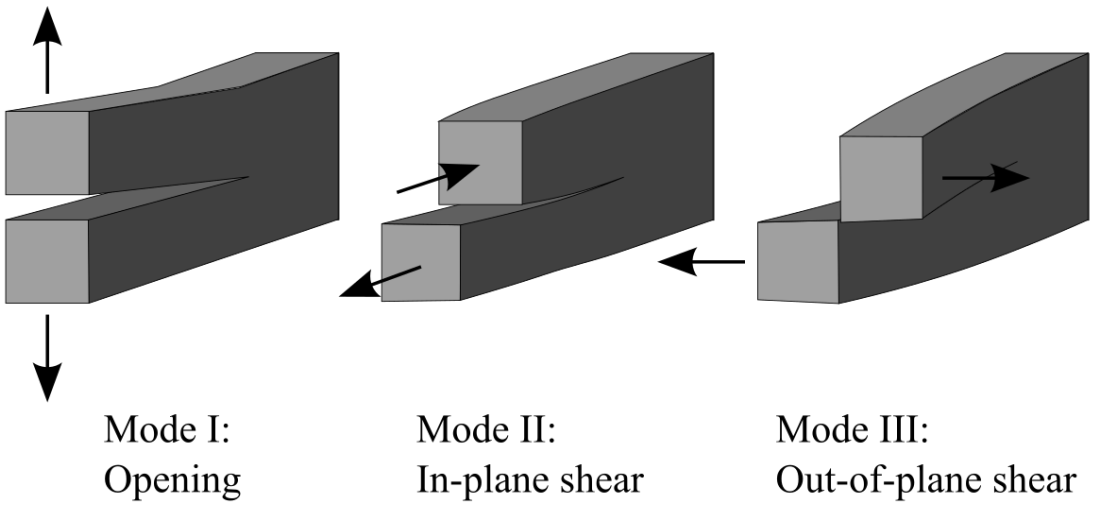

Figure 13. Three different fracture modes.

Fundamentally, fracture mechanics is divided into two groups: Linear Elastic Fracture Mechanics (LEFM) and Elastic-Plastic Fracture Mechanics (EPFM). LEFM was first introduced by A.A. Griffith [86] at the beginning of the 19th century in order to describe the brittle failure phenomenon. Griffith showed that materials have various defects, such as flaws, micro cracks; and those defects cause stress concentrations to exceed maximum allowable stress values at that regions. After that, G. R. Irwin [87] conclude that plasticity has great importance while working with ductile materials. On top of that, he discovered the stress intensity factor phenomenon, which is the quantity of required fracture energy for failure. In the EPFM, unlike LEFM, nonlinear behaviors of the materials under the applied loads are included, considering the effects of the plastic zone on the imitation and propagation of the crack [85]. Given that, more inclusive equations have been produced to investigate the materials that show both elastic and plastic behavior. The earliest works that have been suggested by Irwin claim the crack extension resistance curve, which is also called R-curve. The R-curve method, basically, is revealed in order to describe crack growth and failure as stable and unstable, respectively, using the interaction between total energy dissipation rate and crack length [88]. On the other hand, there is a another relatively new method that assuming the crack growth is non-linear elastic proposed by James R. Rice [89] in the 1968 called J-integral.

Rybicki and Kanninen [90] proposed the Virtual Crack Closure Technique (VCCT), one of the most widely used techniques for the numerical study of fracture situations today, by extending the works of Irwin. While using the VCCT technique in the FEA applications, fundamentally, the analysis uses energy release rates for different failure modes (G_I, G_{II}, G_{III}) in order to split the adjacent nodes when the critical value is reached. By doing so, the sum of the energy release rates for particular modes becomes the total energy release rate of that fracture case. Figure 14 shows the illustration of the crack imitation and propagation while using the VCCT technique in a 3D FEA [91].

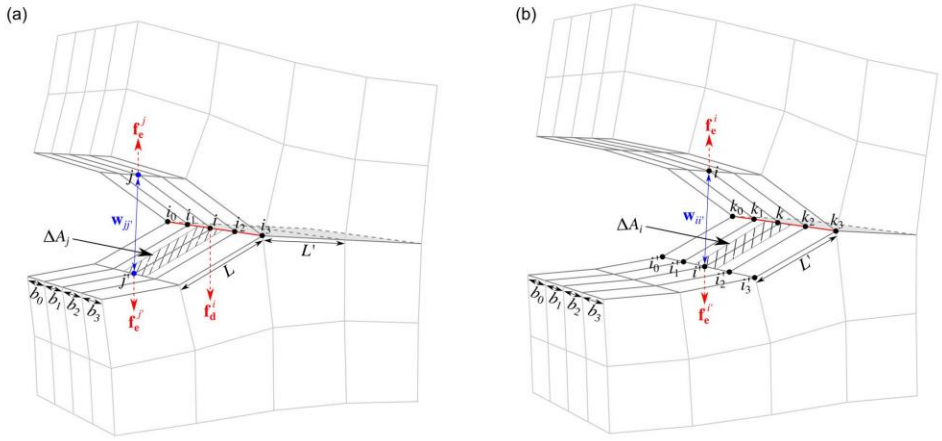

Figure 14. Illustration of the VCCT technique in a 3D FEA. a Crack initiation. b Crack propagation (Source: H. Wu et al., 2021[91]).

There is a new method that is most recently being used for the FEA of the crack initiation and propagation based on the fracture mechanics approach, which means failure governed by energy release rates, called the Extended Finite Element Method (XFEM) [92]. XFEM is, in other respects, a numerical method that involves local enrichment of the nodes close to the discontinuity, using the concept of partition unity. This method is a very useful one to use in FEA since it allows mesh manipulation and adjusts the approximate space, incorporating enriched nodes across the discontinuity, so that there is no need for mesh refinement while the crack grows in a material [93]. The first attempt at proposing XFEM was made by Belytschko and Black [93], and then it was extended by Moës and Dolbow [94] in 1999; it is currently being implemented into various FEA software day by day.

2.6.3. Damage Mechanics Approach

If looking at the fracture occurrence detailed, particularly in the adhesive bonded joints, one can observe that the failure initiates as micro cracks at the interface region among the adjacent surfaces, which cause a reduction in the transferred load and drop on the applied stress in the macro structural stress-strain behavior [9]. Damage mechanics provides the gradual simulation of the fracture from crack imitation to complete debonding by means of implementing bonding behavior [43]. Therefore, it is an emerging and frequently employed method by structural analysis engineers while executing FEA of the bonded joints; however, it is an obligation to use this approach more accurately that develop reliable parameter identification techniques and prevent FEA-solving issues, such as convergence difficulties [85].

2.6.3.1. Cohesive Zone Modelling

Although the use of LEFM techniques in FEA yields acceptable results, engineers have increasingly focused on Cohesive Zone Modelling (CZM) as a superior method within damage mechanics. CZM offers many advantages over continuum and fracture mechanics approaches, making it widely used for simulating adhesive bonding and interfacial behavior between composite material plies under both static and cyclic loads [43,85]. The CZM was initially introduced by Barenblatt [95] and Dugdale [96] separately during the late 1950s. This technique, fundamentally, represents the bonding behavior as not a conventional stress-strain curve but the interaction between cohesive traction and crack opening displacement [97]. Fortunately, it is fairly easy to implement this technique in any FEA software in order to analyze fracture behavior for various types of materials and cases, in particular, adhesive bonded joints. Today, one can find CZM technique as already implemented in many FEA solver software currently in use; thus, CZM can be used by employing different types of cohesive elements in the contact areas [98]. Figure 15 shows the typical utilization of the cohesive elements in a SLJ geometry in order to simulate both cohesive and adhesive fracture behavior [85].

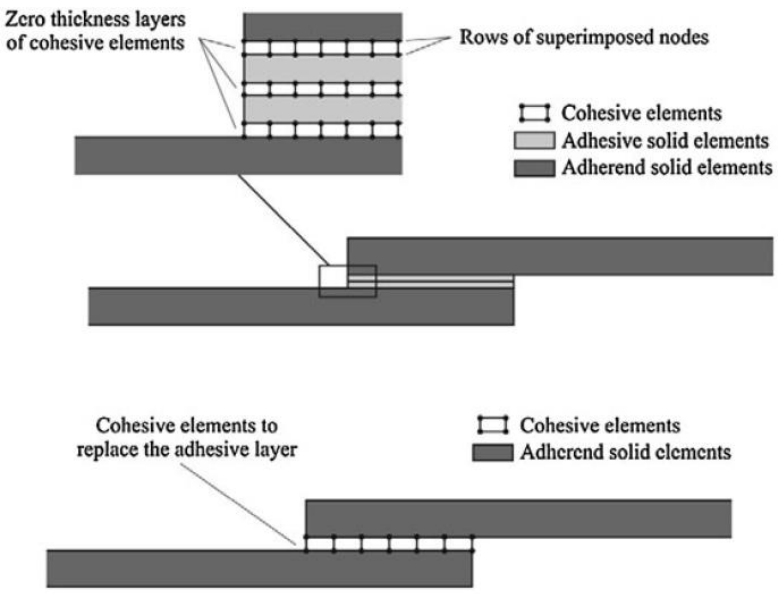

Figure 15. Different types of utilization of the cohesive elements in FEA of the adhesive bonded SLJ geometry (Source: L. F. M. da Silva et al., 2012 [85]).

Through the use of cohesive elements that implement bonding behavior, the simulation of surface separation between adjacent nodes can be achieved without the need for node merging or defining an initial crack. This is accomplished by employing predetermined CZM laws, also known as traction separation laws (TSL). TSLs represent the loading and softening behavior of bonding through linear or nonlinear curves that illustrate the interaction between cohesive traction and separation [99]. Figure 16 shows the typical bilinear traction separation law for mode I failure.

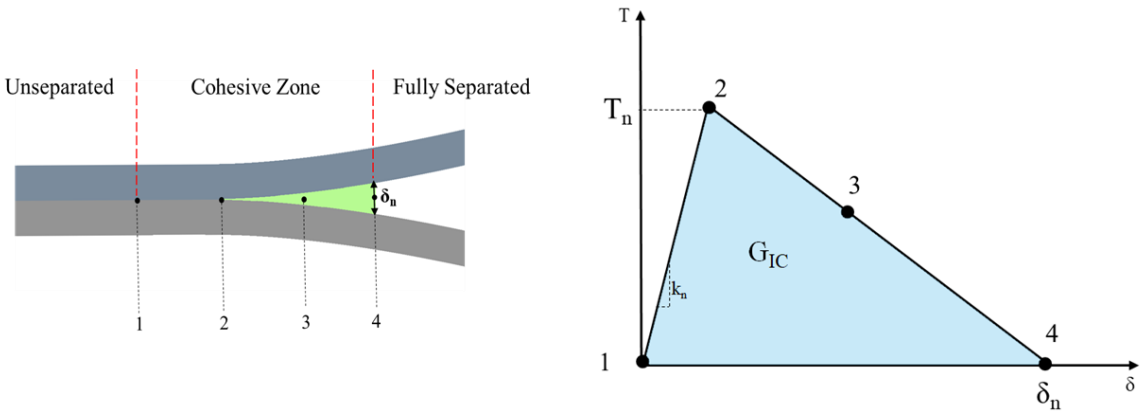

Figure 16. Illustration and graph of a typical bilinear traction separation law.

To put it simply, the TSL curve can be divided into two stages. Initially, the load is gradually increased until it reaches its critical value, also known as the maximum cohesive traction (T_{max}). After that, the behavior shifts to a softening stage, which persists until the maximum cohesive separation value (δ_{max}) is reached. At this point, complete separation is observed. The area under the TSL curve represents the critical strain energy release rate (GC), which is calculated by:

$$G_C = \frac{1}{2} T_{max} \delta_{max} \tag{1}$$

The interaction between traction and corresponding separation can be mathematically expressed as follows:

$$T_i = k_i \delta_i \ \ (i = n, s, t); \ \begin{Bmatrix} T_n \\ T_s \\ T_t \end{Bmatrix} = \begin{bmatrix} k_n & 0 & 0 \\ 0 & k_s & 0 \\ 0 & 0 & k_t \end{bmatrix} \begin{Bmatrix} \delta_n \\ \delta_s \\ \delta_t \end{Bmatrix} \tag{2}$$

Where k_n, k_s and k_t are the cohesive stiffness values, which corresponds to the slope of the TSL curve. Figure 17 represents the TSL curves for each mode I, mode II and mode III behavior.

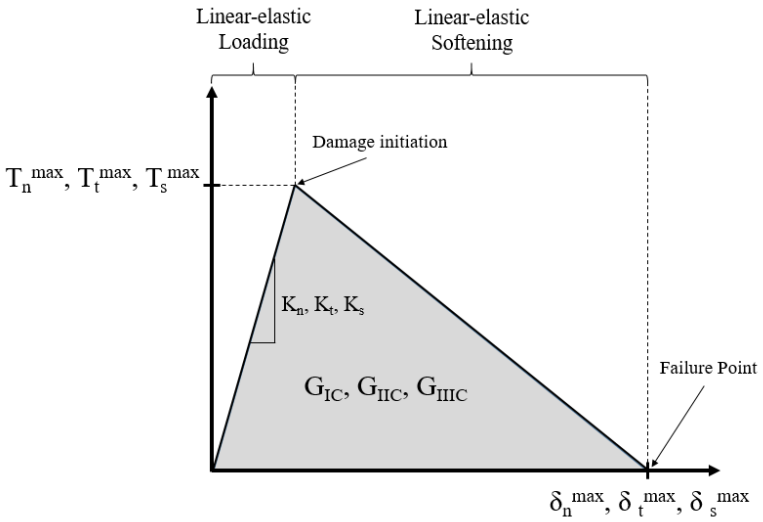

Figure 17. TSL curves for each mode.

Though bilinear TSL is the most widely exploited one, there are various types of TSL curves in order use for different kinds of materials and cases, which are polynomial, exponential, and trapezoidal [99]. Different TSL curves are presented in Figure 18. The main reason for the widespread use of bilinear TSL is being met the need for computational efficiency and very close to the real bonding behavior of brittle adhesive materials; yet, when analyzing the behavior of a ductile adhesive, the literature recommends exploiting exponential or trapezoidal TSL curves [100].

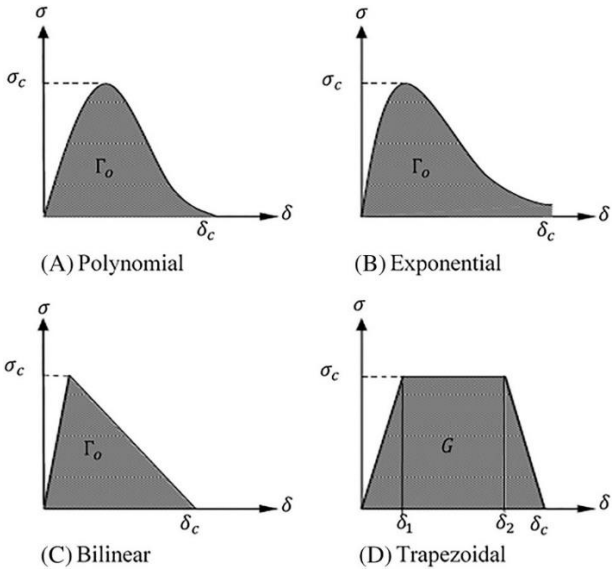

Figure 18. Various types of the TSL curves (Source: J. Zhang et al., 2012 [100]).

Obviously, the bonded joints exhibit not just pure mode I ore mode II type failure but mix-mode failure, too, often seen. In the case of bonded joint analysis where forces act from different directions act, mix-mode analysis shall be used in order to conduct a proper simulation. While computing mix-mode behavior, generally, two different criteria are begin used in the literature to combine mode I and mode II failure: Stress based and Energy based criteria. The stress-based one is the quadratic nominal stress criterion, which is mathematically expressed as follows [98]:

$$\left\{\frac{\langle T_n \rangle}{T_n^0}\right\}^2 + \left\{\frac{\langle T_s \rangle}{T_s^0}\right\}^2 = 1 \qquad (3)$$

In the quadratic nominal stress criterion, the bonding behavior switches to the softening stage with the fulfillment of the eq. 3. By doing so, damage initiation and propagation under mix-mode conditions would be simulated. Mix-mode bilinear TSL is illustrated in Figure 19.

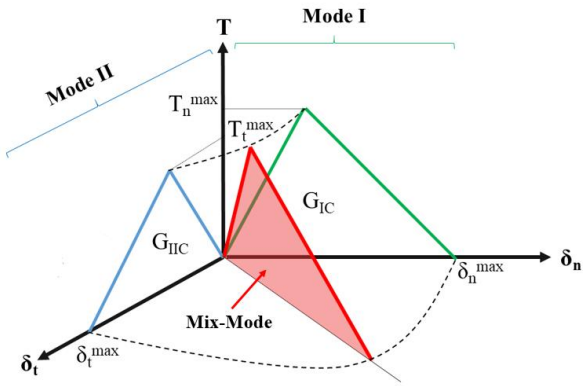

Figure 19. Graphical representation of mix-mode bilinear TSL.

The other method, combined energy criterion, which is an energy-based one, takes into account critical energy release rates for both mode I and mode II behavior and combines them in order to initiate and propagate the crack in the case of mix-mode loading. Combined energy criterion can be represented as:

$$\frac{G_I}{G_{IC}} + \frac{G_I}{G_{IIC}} = 1 \qquad (4)$$

While;

$$G_I = \int T_n d\delta_n \quad , \quad G_{II} = \int T_t d\delta_t \qquad (5)$$

Where G_I and G_{II} are normal and tangential energy release rates, T_n and T_t are maximum cohesive tractions and δ_n and δ_t are maximum cohesive displacements for mode I and mode I behavior, respectively.

There are numerous studies that employ the CZM technique in order to execute numerical analysis on the adhesive bonded components, in particular, SLJ coupons [24,101,102]. As a brief mention of the most known ones, Li et al. [103,104], Blackmanet al. [105], and Liljedahl et al. [106] studied the use of the CZM technique in the analysis of the mix-mode behavior, executing FEA of the different types of joint geometries. They showed, additionally, the appropriateness and accuracy of the failure prediction by means of the CZM technique. de Moura et al. [107] proposed the comparison of the continuum damage model and CZM technique by analyzing the pure mode I and mode II behaviors. They used, on top of that, a trapezoidal TSL curve in order to simulate a ductile adhesive bonding behavior. J. Diaz et al. [108] considered the accuracy of FEA to simulate adhesively bonded joints under static load. They tried to compare the performance of several modeling techniques for the joint made of two CFRP adherend bonded by an epoxy film adhesive layer. Ligang Sun et el. [109] and MD Banea et al. [110] studied CZM for the simulation of the composite bonded joints. M.Z. Sadeghi et al. [111] showed the comparison of the different modeling techniques, analyzing SLJ geometry. There are also many more studies that use CZM to analyze micro, meso and macro scale bonding behavior under different loading scenarios while using different materials [112–120].

2.6.3.1.1. Cohesive Zone Parameters

While utilizing the CZM technique can result in significant advancements in numerical analysis of fracture occurrences in adhesive bonded structures, it is essential to obtain specific CZM parameters to define bonding behavior. However, identifying these parameters can be a challenging process as it requires various experimental characterizations or calibration procedures to ensure accurate compatibility with analysis results [44].

The CZM parameters correspond to the curve of the TSL boundaries for mode I and mode II behavior, which are maximum normal cohesive traction (T_n), mode I critical strain energy release rate (G_{IC}), maximum tangential cohesive traction (T_t), mode II critical strain energy release rate (G_{IIC}) for the fracture energy based calculation. Additionally, separation distance-based calculations can be used, defining contact displacements (δ_n, δ_t) values instead of critical strain energy release rates [66]. In the

literature, there is no standardized experimental method available, yet many studies have been published by means of defining CZM parameters. There are, mainly, three data reduction methods being used to determine CZM parameters: property determination method, inverse method, and direct method. In the following, general information and consideration of the three main methods are given [43].

On the whole, three data reduction methods are being exploited to find out CZM parameters: property determination method, inverse method and direct method. The property determination method, basically, relies on the estimation of the CZM parameters, considering related bulk mechanical tests; this technique, due to the inherently yielding inaccurate results, is not recommended by the literature. In the inverse method, the parameters are determined by comparison of the experimental and numerical test results, particularly load-displacement curves, using various nonlinear programming techniques. The direct method, on the contrary, can be summarized as the determination of the CZM parameters for each mode, crying out, generally, two main bonding characterization tests, which are DCB and ENF. The DCB test, which is the quite known mechanical test standardized to measure mode I fracture toughness of the unidirectional composites, is being used to characterize the bonding behavior at normal directions. ENF test, which is also the standardized method to measure mode II interlinear fracture toughness, is being used for the characterization of the bonding behavior at the shear direction. Nevertheless, it is an obligation to employ a compelling optical measurement technique called digital image processing (DIC) whilst carrying out the DCB and ENF test in order to measure crack propagation [43,44,66]. Figure 20 presents the schematic illustration of the determining CZM parameters exploiting the direct method [112].

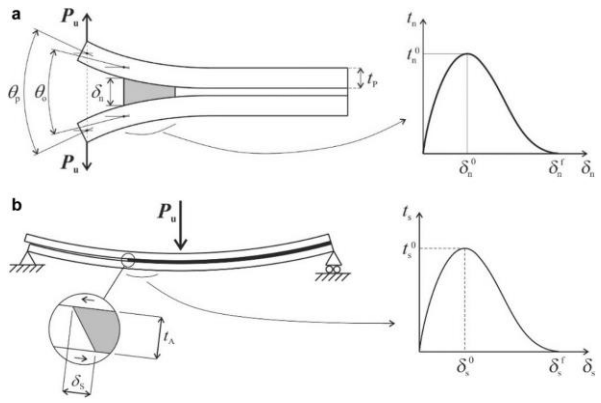

Figure 20. Schematic illustration of the determining CZM parameters exploiting DCB and ENF tests (Source: D. F. O. Silva et al., 2012 [112]).

CHAPTER 3

EXPERIMENTAL WORK

Not only to examine the behavior of the adhesively bonded CFRP composite structures but characterize the bonding phenomenon for the specific situations and conditions, in the different scale and load scenarios, quite assorted experimental test setups were prepared and analyzed. Beyond evaluating the mechanical performance of the adhesively bonded CFRP composite systems, obviously, the exalted purposes behind the experimental works are feeding the finite element analysis and assessing the compatibility of the present numerical method. Nonetheless, the presented mechanical test setups are shedding light on the adhesive bonding behavior in every aspect, on top of that, propounding both positive and negative consequences of the laser surface treatment technology on the CFRP composite materials, which will be discussed in the experimental results section in the following.

3.1. Laser Surface Treatment

As state-of-the-art, laser surface treatment application was utilized in order to improve the bonding performance between the CFRP composite structure used for aerospace applications. It is widely agreed upon that the surface conditions of the joining parts have intense effects on the strength of the bonded components. Between the various surface treatment operation techniques currently applied, laser surface treatment is a method that has just started to be utilized and is being continued to develop [121]. This technology is, basically, based on the forming of rough surfaces in order to enhance the bonding performance, increasing the mechanical interlocking by means of allowing the adhesive to seep into these protruding surfaces [63,122,123]. In pursuit of this, by employing laser beam energy, the main achievement for the CFRP composite structures is the removing the resin rich surface from the top of the bonding surfaces in order to create a rough area consisting of bare fiber strands.

Laser surface treatment technology, fundamentally, utilizes the ablation ability of the laser beam by means of creating concentrated energy density in a small area - a laser point [60]. By courtesy of heating the specifically designated area, the surface of the adherents in this study, selective removal of the resin reach zone on top of the CFRP surfaces was achieved. Through this laser surface application, especially applied for a CFRP material, it was crucial the operate the application without effectuate break or damage on the fiber strands since those fiber strands will be the main structural elements of the adhesive bonding [121]. This laser ablation action, on top of that, creates oxidation on the fiber strands; as a result, provided chemical groups on the bonding surfaces enhance the chemical adhesion [63,124,125].

In addition to increasing the bonding performance by means of creating different topologies on the surface, laser surface treatment also allows the operation of removing contaminants by cleaning the surface, which requires a great deal of effort during the manufacturing process of adhesive bonded structures. On top of that, From the point of view of industrial use and mass production, it is quite appropriate to make laser surface treatment a part of manufacturing in industrial applications since it does not require complicated operations and can be easily adapted to automatic production processes [126]. At the point where today's laser technologies have come, the amount of heat transferred by the laser beam to the surface can be controlled by many different parameters, such as pulse duration, pulse energy and repetition rate; in addition to these, the response of materials to laser wavelength also differs. This allows the surfaces to be processed with a precision that cannot be achieved with any other technique [127].

In this study, laser surface treatment application executed via employing an infrared (IR- Ytterbium) nanosecond laser machine (FLAST-NanoMARK-50w). The laser surface treatment on the CFRP composite adherent surfaces for all experimental test coupons investigated in this study - such as DCB, ENF, SLJ and SSJ specimens - prior to the joining. The dimensions of the laser treatment setup and operational boundaries, which are the limitations of the present laser device, are illustrated in Figure 21.

The ablation setup does not have integrated data acquisition and image processing systems. Instead, optical microscope and SEM techniques were utilized after the treatment operation to provide image processing.

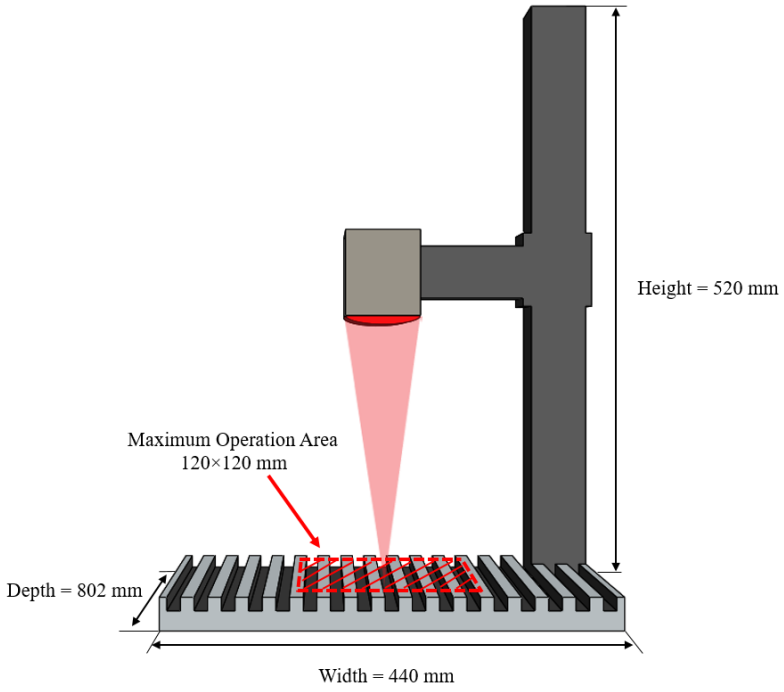

Figure 21. Illustration of the laser treatment setup and operational boundaries (Source: İplikçi, Hande, et al. 2023 [128]).

In the laser surface treatment setup and processing strategy for the proper ablation, one must consider certain critical parameters and limitations. Certainly, one of the most important factor is achieving maximum surface roughness while minimizing fiber damage. On top of that, it is also crucial to carefully adjust the laser focus to obtain the desired treated surface. To achieve this, adjustments were done for the height of the laser optic head for each surface to be treated. However, we are limited by the maximum height the optic head of the laser system can reach. The laser optical head can only move within a limited area for focusing, which is determined by the movement distance of the focusing elevator (64 x 140 x 610 mm). Additionally, the maximum machining space in the x-y plane for this work is the scanning field of 120 × 120 mm^2.

In this work, in order to carry out laser surface treatment operation on the surfaces of each DCB, ENF, SLJ and SSJ specimens, prior to the bonding process, the laser machine parameters applied with the following: wavelength of 1064 nm, frequency of 100 kHz, spot diameter 30 nm and pulse width of 100 ns. On top of that, while executing laser treatment, the laser power was adjusted to 20 W and the laser speed was 10000 mm/s with a frequency of 100 kHz. During the laser surface treatment carried out with

successive point shots, the distance between the two laser points was set to 0.2 mm. This distance, indeed, was obtained as the optimum result of trying various lengths. At the same time, the aforementioned laser surface treatment machine parameters dedicated in the previous works, a focused study on laser surface treatment and its effects on materials, in order to achieve the selective removal of the epoxy without damaging fibers [127]. In that study, optimum parameters to be used for CFRP material were revealed by İplikçi et al. [127], applying mechanical tests or secondary electron microscope (SEM) and optical microscope characterizations on coupons produced using different parameters. Laser surface treatment equipment can be seen in Figure 22 while eluting surface treatment on a CFRP plate.

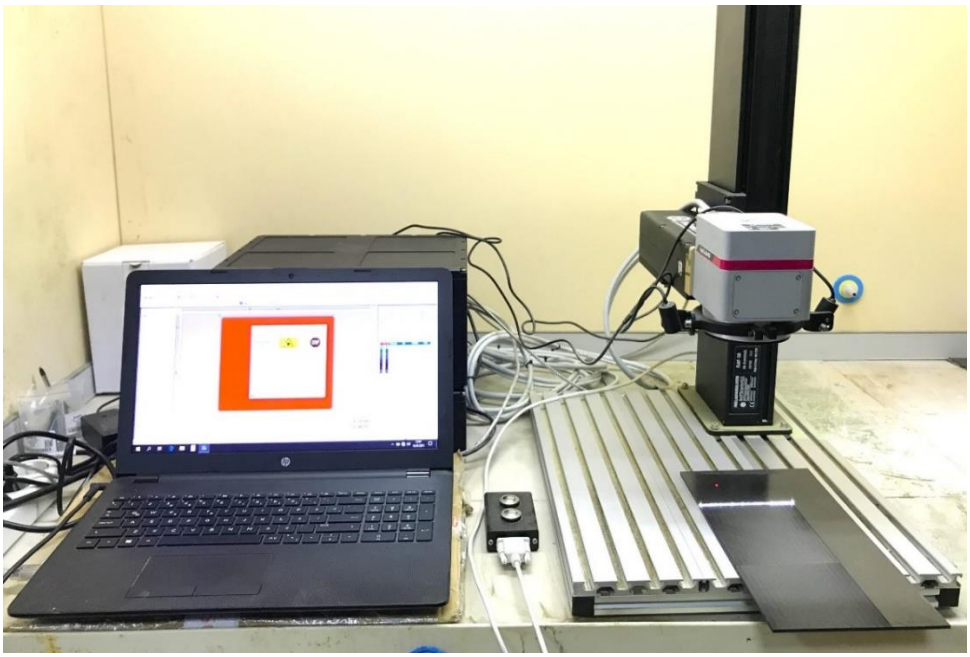

Figure 22. Laser surface treatment equipment during operation.

The secondary electron microscope (SEM) images of both leaser surface treated (LST) and untreated (LSUT) surfaces were taken in order for a better and deep examination of the changes occurring at the surface of the CFRP material. Figure 23 shows the SEM images taken from the laser surface treated adherents according to the aforementioned optimum laser application parameters. In Figure 23, SEM pictures taken from the İplikçi's work [127], the laser surface treated CFRP surface view from above can be seen with different scales.

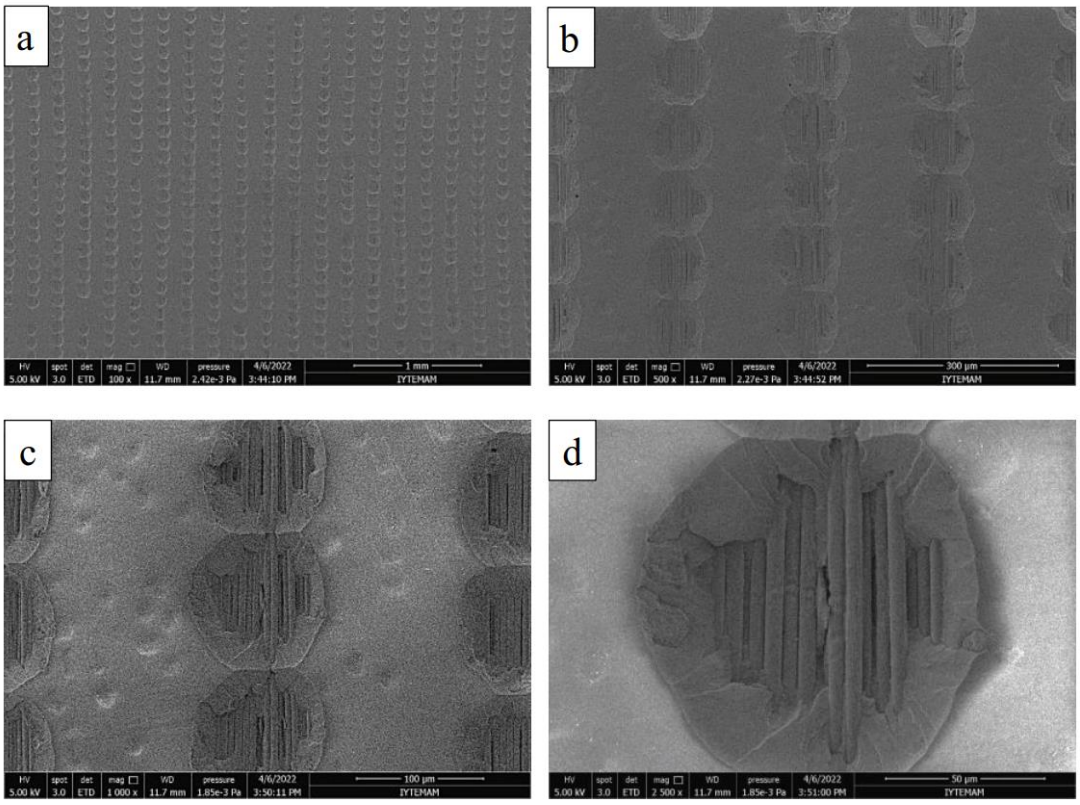

Figure 23. SEM images of treated surfaces from the front faces (Source: İplikçi, Hande, et al. 2023 [128]) .

The SEM images in Figure 24 and Figure 25 present the side view of the laser surface treated CFRP surfaces. The SEM image results can be concluded as it is observed that selective removal of the epoxy on top of the surface is achieved by means of the aforementioned optimum parameters without damaging the carbon fiber strands. With the help of the applied 0.2 mm laser offset distance, the hollow topology structure that continues regularly in a row is accomplished.

The created cavities and removed epoxy on top of the adherent's surface can be clearly seen in Figure 25 with the dimensions of the resulting cavities.

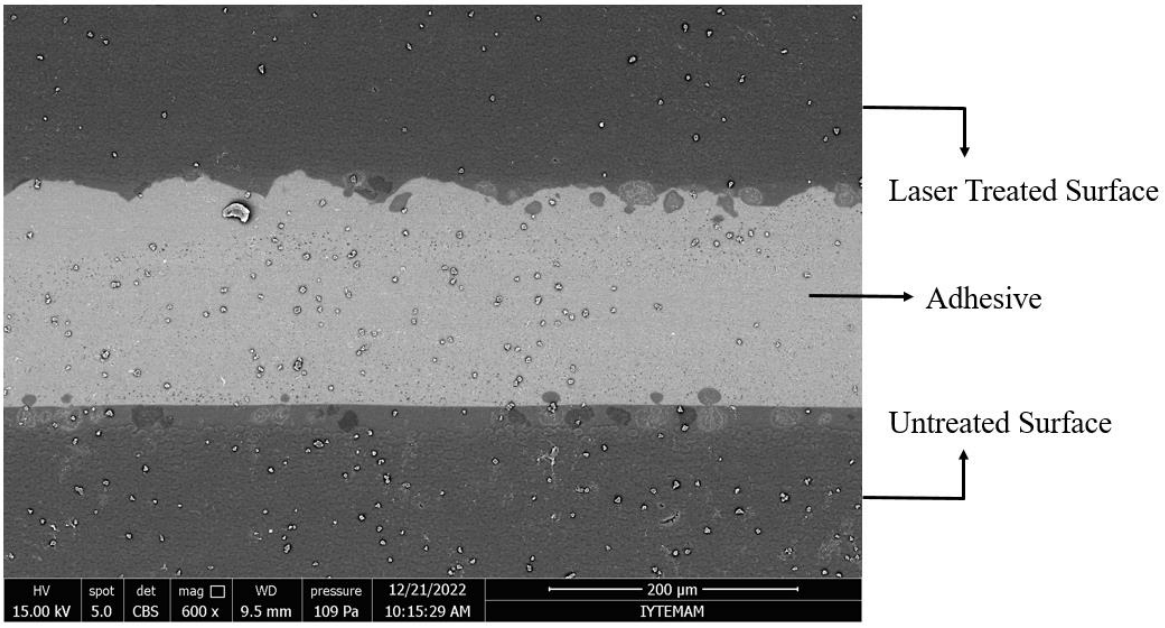

Figure 24. SEM images of treated surfaces from the side view.

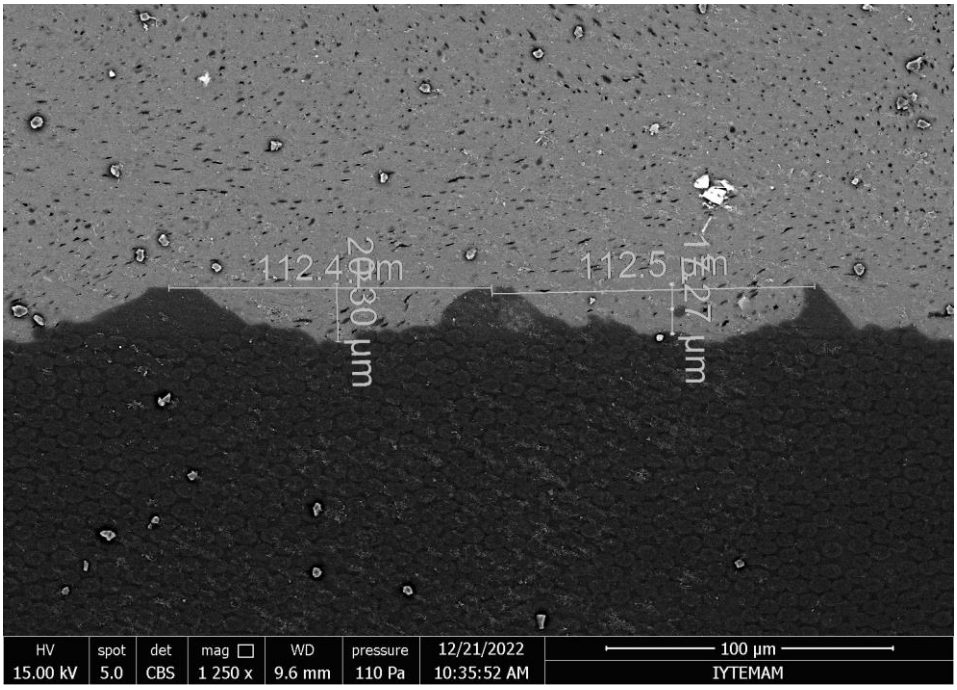

Figure 25. Created cavities on top of the CFRP surface.

3. 2. Adhesive Bonded Specimens

In this study, primarily, mixed mode fracture behavior was measured using two different specimen geometries. It is for this that Single Lap Joint (SLJ) specimens at the coupon level and Skin-Spar Joint (SSJ) specimens at the element level were experimentally analyzed. In order to create the SLJ and SSJ specimens made of CFRP composites, prepregs and epoxy adhesives were sourced from high-performance components widely used in aircraft structures, at the same time, specimens were manufactured at Turkish Aerospace Industry (TAI) facilities according to aerospace industry standards. For all specimens, three plies of epoxy film adhesive were placed between adjacent surfaces to achieve the same adhesive thickness. The details of both SSJ and SLJ geometries, as well as manufacturing techniques and specifications, are given in the following.

3.2.1. Single Lap Joint (SLJ) Specimen

Due mainly to observing the shear intensity behavior of the adhesively bonded adherents, SLJ specimens were produced according to ASTM D5868 standard. CFRP parts were manufactured using unidirectional laminates made of carbon/epoxy HexPly^{TM} M91/34%/UD194/IM7-12K prepregs (HEXCEL PRIMETEX^{TM}, Connecticut, USA); and laminates were placed as [45/0/-45/90/-45 /45]s stacking sequences. Mechanical properties of a cured UD lamina provided by HEXCEL^{TM} official datasheet [129], which has a cured ply thickness of 0.184 mm, are stated in Table 2. Figure 26 illustrates the typical dimensions of the SLJ specimen, additionally, ply configuration for both the CFRP adherents and epoxy film adhesive.

Table 2. Mechanical properties of the one cured lamina of HexPly M91/34%/UD194/IM7-12K prepreg. [129]

Property	Direction	Value
Elastic Modulus (GPa)	X	165
	Y	8.8
	Z	9.4
Shear Modulus (GPa)	XY	5.5
	YZ	4.5
	XZ	5.5
Tensile Strength (MPa)	X	2980
	Y	105
	Z	105
Compressive Strength (MPa)	X	1860
	Y	100
	Z	100
Shear Strength (MPa)	XY	60
	YZ	32
	XZ	60
Poisson's ratio	XY	0.228
	YZ	0.48
	XZ	0.228

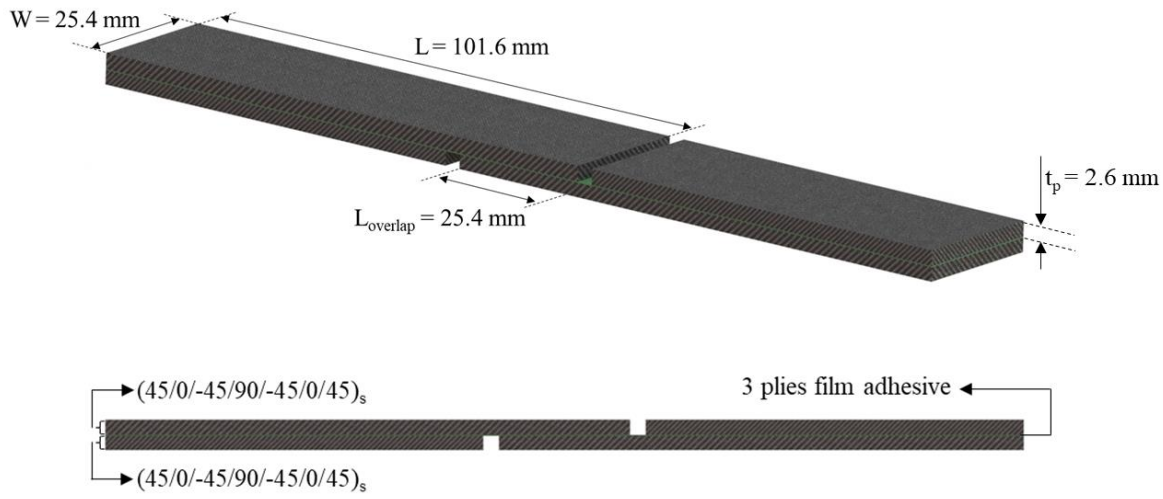

Figure 26. Illustration of typical dimensions of the SLJ specimen and ply configuration for both the CFRP adherents and epoxy film adhesive.

The CFRP parts were manufactured by employing the autoclave technique with a curing stage of 180 °C, and 7 bar for 2 hours, and again bonding operation was carried out by means of autoclave curing operation at 180 °C & 3 bar for 2 h. Overall 14 SLJ coupons were produced and seven of them were subjected to laser surface treatment - from both adjacent surfaces – prior to joining operation. As the details of the autoclave operation, the curing cycles for both adherent made of HexPly^{TM} M91/34%/UD194/IM7-12K prepregs and joining executed with FM300K film adhesive are shown in Figure 27 and Figure 28, respectively.

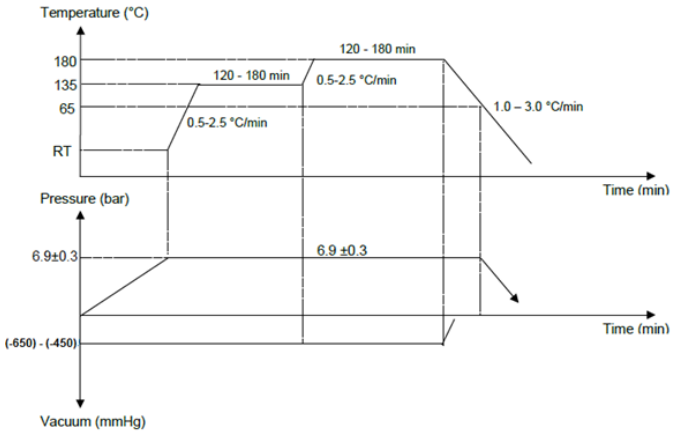

Figure 27. Curing cycle for the autoclave manufacturing of the adherents.

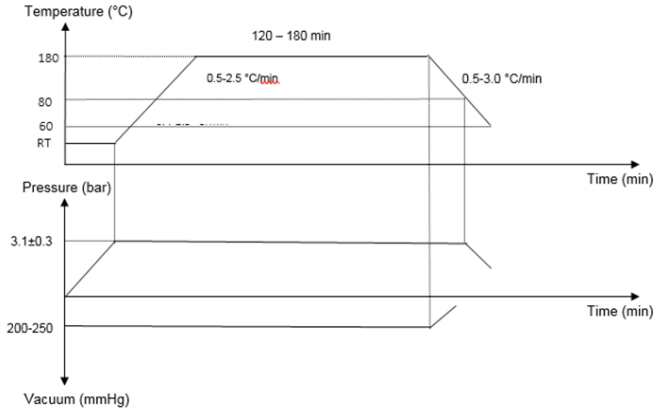

Figure 28. Curing cycle for the autoclave manufacturing of the joining.

Entire SLJ coupons bonded using three plies of FM300K™ (Solvay, Belgium) structural epoxy film adhesive corresponding to 0.6 mm thickness. The mechanical properties of the FM300K film adhesive are given in Table 3, which are provided by SOLVAY™ official datasheet and literature. [130,131]

Table 3. Mechanical properties of the FM300K film adhesive. [130,131]

Property	Symbol	Value
Tensile Yield Strength (MPa)	*f*	14.2
Tensile Modulus (GPa)	γ	2.4
Shear Modulus (GPa)	G	0.9
Poisson's Ratio	ν	0.35

As a mechanical test setup, in order to evaluate the shear intensity behavior of the adhesively bonded CFRP specimens, lap shear tests were executed according to ASTM 5868 [132] standard. Within the laboratory conditions (23±2 C at 50%+-5 relative humidity), the lap shear strength test was carried out using MTS Landmark™ Servo hydraulic test equipment (Static ± 250 kN) (Figure 29). During the test, the load was applied to the specimen through displacement control; the upper grip was fixed whilst the lower grip moved with the 1.3 mm/min crosshead speed rate. Figure 29 presents the lap shear test picture from the beginning of the test and at the time of fracture occurrence, which is a

point when double curvature occurs on the contact region of the specimen – a situation is seen due to the appearing moment on the specimen and creates peel stress concentrations at the tips of the contact region; this phenomenon will be discussed in detail in the numerical simulation sections.

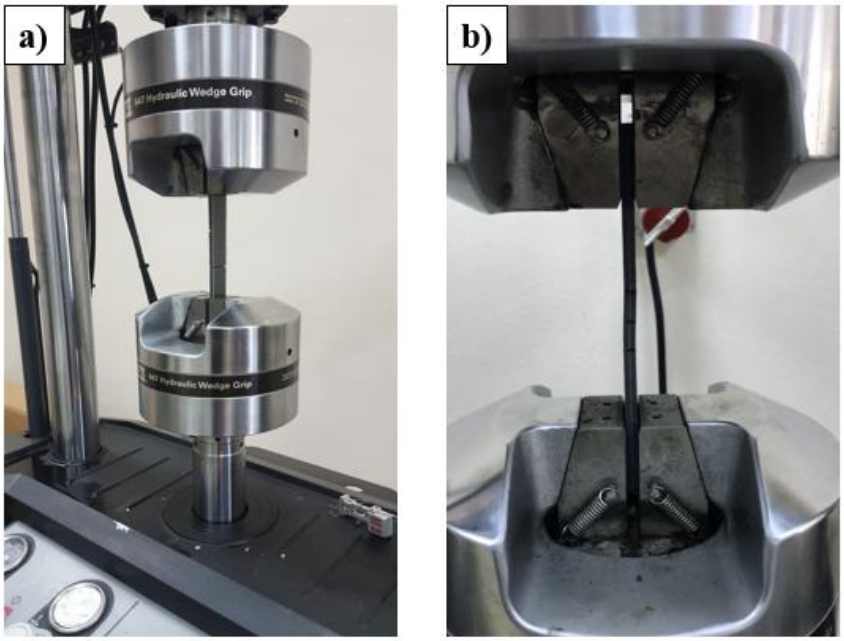

Figure 29. Lap shear test picture a) from the beginning of the test and b) at the time of fracture occurrence.

3.2.2. Skin-Spar Joint Specimen

Spars are the primary structural parts of the skeleton of the aircraft wing-box. The main purpose of the spars in the wing is to ensure integrity and stiffness. The spars, in other words, can be thought of as the beams of the aircraft wing, which connect the fuselage and wings and transfer the load from one to another. During a casual flight, the skin and spar parts, which are in direct connection with each other, are exposed to different types of loads on the contact area. In order to simulate the relationship between adhesively bonded skin and spar structures, a novel Skin-Spar Joint (SSJ) test setup was created due to the lack of standard specimen and test setup in the literature.

This newly designed test setup, mainly, intends to assess peel intensity behavior at the element level scale. Though the skin-spar connection primarily exposes to peel stress during the up and down movement of the wing, in addition to the shear behavior measured in the SLJ test, the peel behavior of the bonded CFRP coupons is evaluated in this test setup.

Presented SSJ test setup, in addition, was selected as an optimum between the many great deals of tried configurations whilst changing many circumstances: skin and spar thicknesses, loading types, specimen geometries, boundary conditions, measuring system, auxiliary units, etc. Figure 30 summarizes the tried various test setups, specimens and configurations.

Figure 30. Various SSJ test setups, specimens and configurations have been tried.

SSJ coupons were manufactured by using woven CFRP composite laminates with stacking sequence sequences of $[45/0/45/0]_{4s}$ for the skin, and $[45/0/45/0/45]_{s}$ for the spar parts. Carbon/epoxy based HexPly^{TM} M21/40%/285T2/AS4C-6K prepregs (HEXCEL PRIMETEX^{TM}, Connecticut, USA) prepregs, which are the most widely used prepregs in the aerospace industry in order to produce aircraft components, were used for SSJ specimens. Unlike SLJ specimens, woven fabrics were chosen due mainly to investigate the bonding behavior for not only UD but woven structures. The mechanical properties of a single cures lamina, a ply with a thickness of 0.285 mm, are given in Table 4; those properties, on the other hand, are taken from HEXCEL^{TM} official datasheet [129]. The general structure and detailed dimension information of the SSJ specimen are illustrated in Figure 31.

Both skin and spar parts were manufactured using the autoclave technique according to the industry standards and prepregs official technical datasheet. The autoclave process was performed by curing stage at 180 °C, and 7 bar for 2 hours. After producing the skin and spar parts, divergent parts joined together using three plays of FM300K (Solvay^{TM}, Belgium) structural film adhesive, curing in the oven at 180 °C & for 2 h, again according to the suggestion of the official datasheet of the adhesive. While joining the skin and spar parts, in order to adhere to the composition of the Single Lap Joint specimens, laser surface treatment was applied and unapplied Skin-Spar coupons bonded together, which corresponds to 0.6 mm bond-line thickness. Overall, eight specimens were produced, consisting of four laser surface treated and four untreated. The manufactured SSJ specimens and one coupon are shown in Figure 32.

Table 4. Mechanical properties of the one cured lamina of HexPly M21/HS/40RC/T2 /AS4C /285 /6K prepreg [129].

Property	Direction	Value
Elastic Modulus (GPa)	X	61.3
	Y	61.3
	Z	6.9
Shear Modulus (GPa)	XY	19.5
	YZ	2.7
	XZ	2.7
Tensile Strength (MPa)	X	805
	Y	805
	Z	50
Compressive Strength (MPa)	X	509
	Y	509
	Z	170
Shear Strength (MPa)	XY	125
	YZ	65
	XZ	65
Poisson’s ratio	XY	0.04
	YZ	0.3
	XZ	0.3

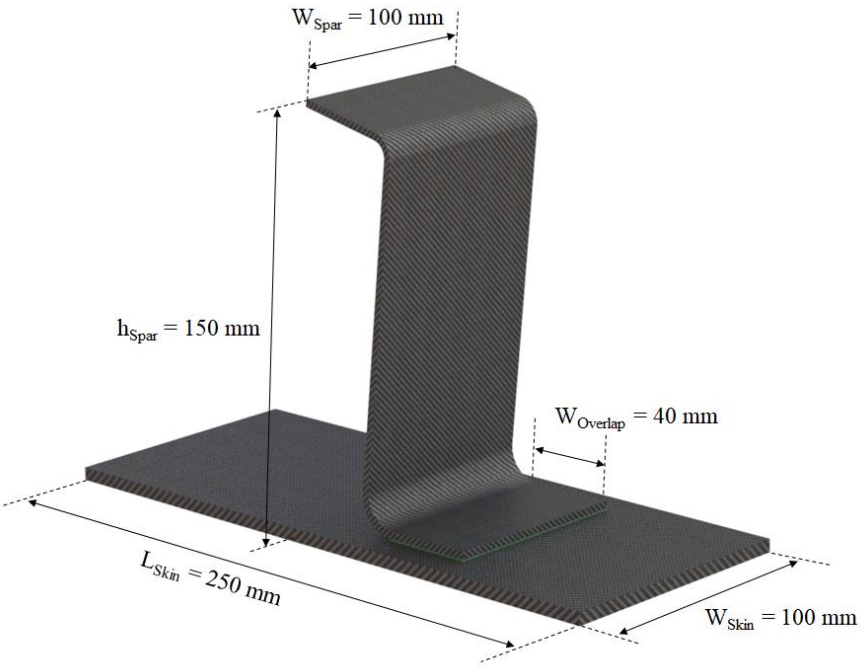

Figure 31. Illustration of the SSJ specimen with the dimensions.

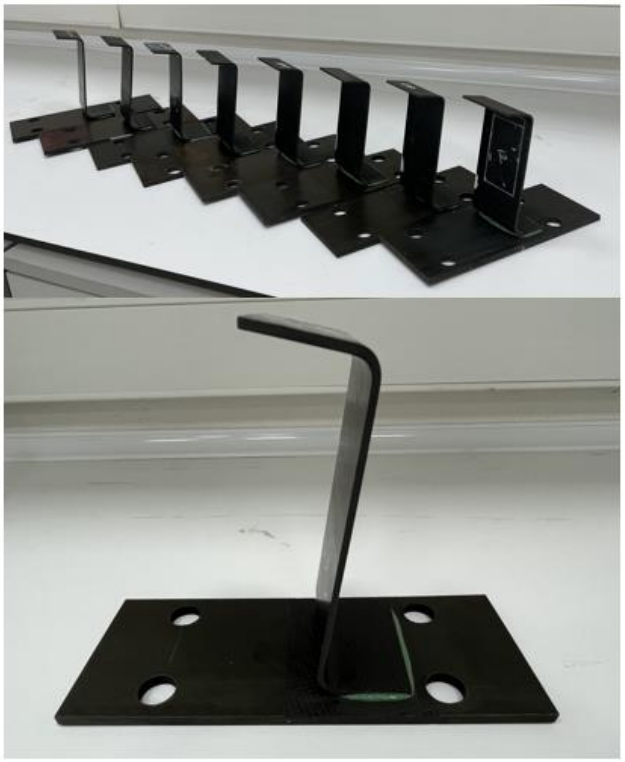

Figure 32. SSJ test specimens.

Within the laboratory conditions - 23±2 C at 50%+-5 relative humidity - pull-off strength test was carried out using Shimadzu^{TM} test equipment (Static ±5 kN). As boundary conditions, the spar part is fixed to the ground using clamps at two sides while the skin part is moved by the upper grip with a 1 mm/min crosshead speed rate. The speed rate was chosen as 1 mm/min in order to prevent the irregular force-displacement behavior caused by a sudden fracture that may occur as a result of abrupt crack propagation. In order to acquire the load-displacement (P-δ) data, the relative displacement between the skin and spar part was recorded by video extensometer. A gripping apparatus was designed to provide fitness among the spar and the upper grip by means of suppressing the angled structure on the upper portion of the spar. This design is, fundamentally, enables vertical upward movement on the specimen. In order to acquire the load-displacement (P-δ) data, the relative displacement between the skin and spar part was recorded by video extensometer employing markers in designated areas on both the skin and spar bodies, as can be noticed in Figure 33, as black lines on a white background.

Figure 33. Image from SSJ joint specimen test moment.

3.3. Experimental Results

This section presents the experimental results of the SLJ and SSJ test specimens. The load-displacement curves and maximum stress values are introduced and comprised of the laser surface treated (LST) and laser surface untreated (LSUT) surface conditions. Besides revealing the behavior of the adhesively bonded CFRP composite structures and the effects of the laser surface treatment on both the normal and shear performance of the joints, acquired data will be utilized for comparison of the experimental and numerical analysis results in Chapter 7. That is why the load-displacement graphs are given instead of stress-strain curves, unlike usual; however, the maximum stress values are given, too, in order for a better comparison between LST and LSUT surface configurations.

3.3.1. Single Lap Joint (SLJ) Experimental Results

Figure 13 presents the load-displacement curves of the SLJ test; both LSUT and LST configurations are given in Figures 34a and 34b, respectively. As can be seen that load-displacement curves of the adhesively bonded CFRP SLJ coupons show nearly linear elastic behavior from the beginning of the test to the fracture moment where, at the same time, the point that maximum reaction force is observed; in the continuation, the abrupt load drop is observed accompanied by a brittle fracture.

It was monitored that the maximum load (P_{max}) values diversified in the range of 5-9 kN for the LSUT configuration and 10-12 kN for the LST configuration. The maximum displacement values changed in the range of 0.25-0.35 for the LSUT and 0.45-0.55 mm for the LST surface conditions. With regards to this, when correlating the different surface conditions, one can easily notice that LST specimens display enhanced joint execution, as proven by the increase in maximum load and maximum displacement values at the point that fracture occurs.

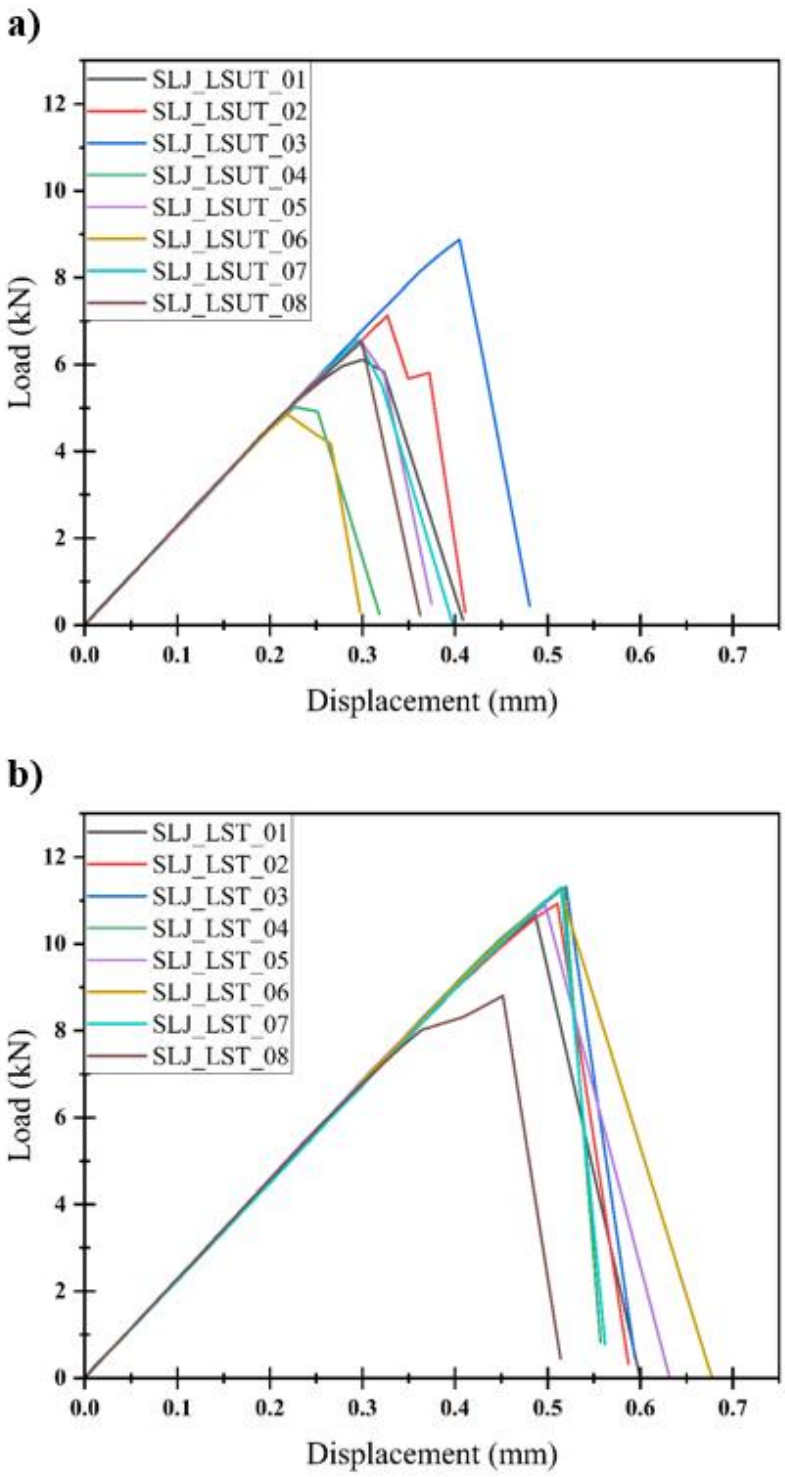

Figure 34. Load-displacement curves of the SLJ specimens for a) LSUT and b) LST surface configurations.

Figure 35 indicates and compares the maximum average shear strength values for the SLJ specimens in LSUT and LST configurations. The average maximum shear strength values are calculated as follows:

$$\tau = \frac{P_{max}}{L\,W} \tag{6}$$

Where L is bond line length, W bond line width.

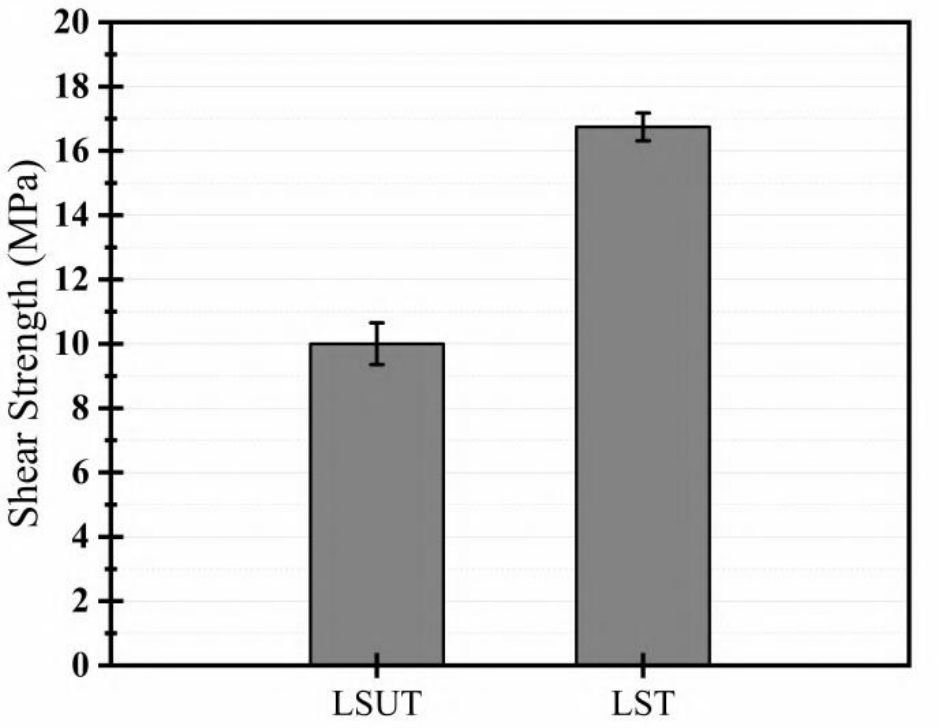

Figure 35. Comparison of the maximum average shear strength values for the SLJ specimens in LSUT and LST configurations.

As can be seen from the maximum average shear strength values of the LSUT and LST specimens, it is clear that the performance of the adhesively bonded SLJ specimens are enhanced. This means that the strength improvement due to the laser surface treatment application was perceived as approximately 65% on the secondary bonded SLJ specimens.

Additionally, in order to examine the fracture mode in detail and to fully understand the factors causing the debonding, the photos of the SLJ coupons after the failure are given in Figure 36. The after-failure images of the bonding region of the SLJ specimens set forth that the failure mode was changed by means of laser surface treatment application. As can be observed from the comparison of LSUT and LST SLJ specimens (Figure 36), for the LSUT specimens, the adhesive material is evenly distributed on the two adjacent surfaces in integrity, exhibiting a typical adhesive failure. In contrast, as the most apparent proof of an improvement in the strength of the adhesion, there were immensely interfacial debonding segments detected in the laser surface treated specimens. Moreover, a cohesive fracture pattern was also noticed in some portions.

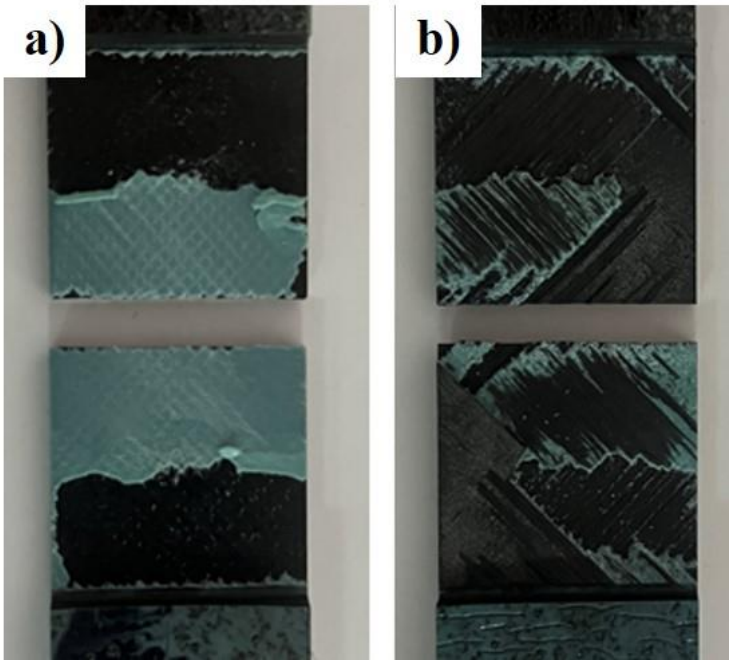

Figure 36. The after-failure images of the bonding region of the SLJ specimens for the a) LSUT b)LST configurations

3.3.2. Skin Spar Joint (SSJ) Experimental Results

The load-displacement graphs of the Skin Spar Joint specimens in both LSUT and LST surface conditions are given in Figure 37. While recording the displacement values with the video extensometer, exceptionally noisy curves were obtained; therefore, after recording force-displacement curves, linear curve fitting was applied to avoid noisy

graphs. The results of the SSJ test indicate that the maximum force assorted around 2800-4500 for the LSUT and 2600-4000 N for the LST configurations. The maximum displacement values were also observed in the range of 0.16-0.25 mm for the LSUT and 0.3-0.5 mm for the LST and LST surface conditions. As the main inference of the SSJ test results, differing from the SLJ test, in contrast to SLJ test results, when different configurations are compared, it is apparently seen that no considerable bonding performance enhancement arises by means of the laser surface treatment application. This is mostly derived from the manufacturing technique – an out-of-autoclave method – utilized while curing the joining of SSJ test coupons. In other words, somehow, the out-of-autoclave method inhibits the profit taken from laser surface treatment.

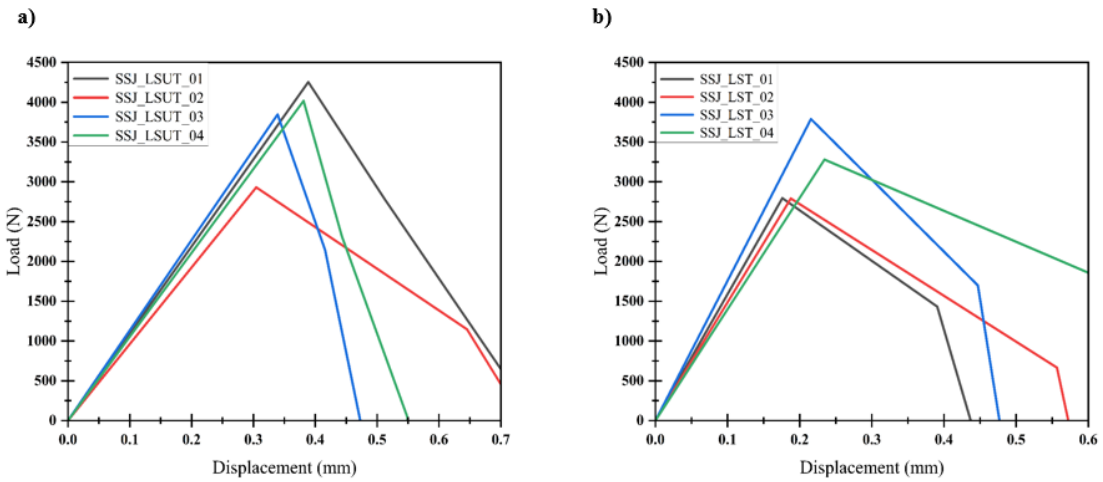

Figure 37. The load-displacement graph of the Skin Spar Joint specimens for a) LSUT and b) LST surface conditions.

Figure 38 indicates and compares the maximum average shear strength values for the SLJ specimens in LSUT and LST configurations. The average maximum shear strength values are calculated as follows:

$$\sigma = \frac{P_{max}}{L\,W} \tag{7}$$

The comparison of peel stress values for specimens with LSUT and LST surface configurations indicates that the laser surface treatment application did not positively affect the peel strength magnitudes of the SSJ specimens.

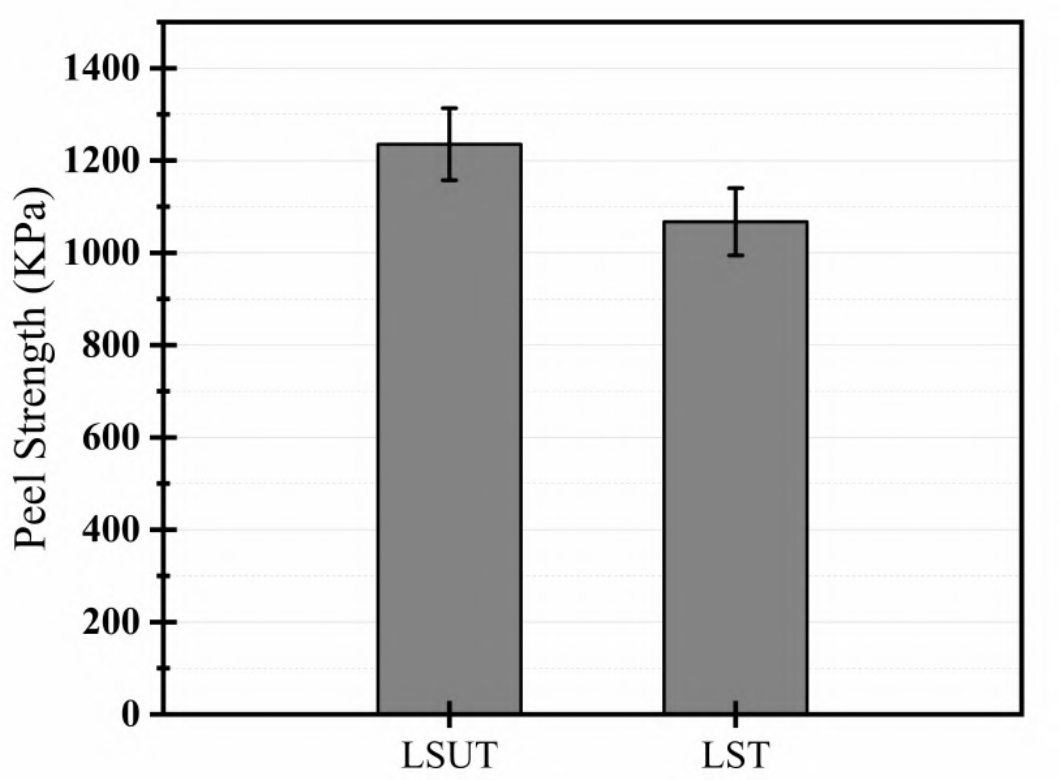

Figure 38. Comparison of the maximum average shear strength values for the SLJ specimens in LSUT and LST configurations.

Figure 39 represents, moreover, the after-failure surface pictures of SSJ test specimens. After failure surfaces, too, were studied in order to investigate the fracture mode comprehensively and to adequately grasp the factors inducing the debonding patterns. As can be seen, predominantly cohesive fracture formation was detected in both LSUT and LST surface conditions, yet, it is obvious that, in the LST specimen's surface, laser surface treatment application creates debonding failure portions. These debonding areas are the main explanation for not observing considerable performance enhancement on the LST configuration.

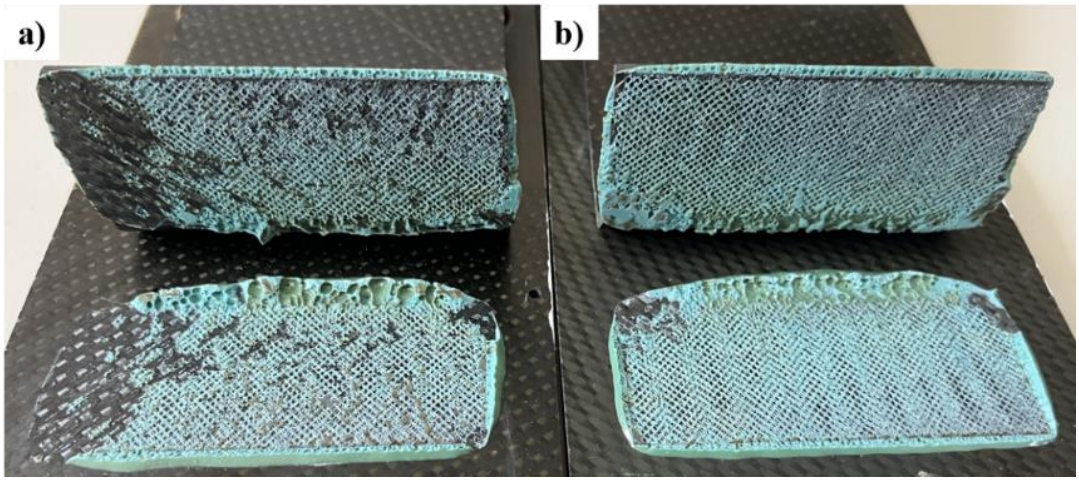

Figure 39. After failure surface images of the SSJ specimens for a) LST and b)LSUT configurations.

CHAPTER 4

BONDING CHARACTERIZATION

In the literature, though there are various studies employing the CZM technique to study adhesive bonding, values taken from other studies or somehow estimated have been used as cohesive parameters in the vast majority of carried out studies. Yet, in order to provide proper prediction whilst executing numerical analyses, without doubt, working with exact and accurate parameter values – which are the values that must be for work-specific conditions - is crucial. It is for this that obtaining CZM parameters according to not only adherent and adhesive materials but actual surface conditions plays a vital role in the reliability of the numerical analysis result. Therefore, while executing FEA by employing the CZM technique, it is an obligation to carry out a characterization study on the bonding, considering the materials and contact area status used.

As a conventional method of determining CZM parameters by means of bonding characterization study, entire parameters are being evaluated by conducting either only experimental or numerical study. The general approach while executing experimental bonding characterization work is, basically, the identification of the Critical Strain Energy Release Rate (G_C) values by measuring interlaminar fracture toughness magnitudes during both the mode I and mode II tests, according to the corresponding ASTM standards. Thereafter, as the difficult part of using just an experimental study, Maximum Cohesive Traction (T^{max}) values must be obtained via carrying out sophisticated crack growth measuring work by employing Digital Image Correlation (DIC) systems – a system that comprises using relatively expensive equipment. On the other side, as an alternative option to the experimental operation, one can utilize numerical procedures in order to obtain CZM parameters. This numerical work, fundamentally, involves nonlinear curve fitting methodology executing various optimization techniques.

This study follows an amalgamation of experimental and numerical methods to identify CZM parameters for mode I and mode II behavior. This is all to say, Critical Strain Energy Release Rate (G_C) values were evaluated through experimental DCB and ENF tests, obeying and using the calculation methods in the corresponding ASTM

standards. However, Maximum Cohesive Traction (T^{max}) values were estimated by means of the calibration procedure comparing numerical and experimental works via inverse fitting methodology. This contemporary novel method was created primarily to maintain both accuracy and simplicity whilst executing a bonding characterization study through combining the benefits of the two unlike methods. In essence, this technique suppresses the DIC equipment requirement in the experimental work; furthermore, the accuracy and computational work of the FEA has become improved due mainly to determining only the traction values using the inverse method.

4.1. Bonding Characterization - Experimental Work

In order to examine the bonding characterization study, two different test setups, DCB and ENF, were utilized. The Double Cantilever Beam (DCB) and End Notched Flexure (ENF) tests were used for the investigation of mode I and mode II bonding behavior, respectively.

Specimens were prepared following the ASTM D5528 [133] standard in order for the manufacturing the DCB test coupons. The DCB specimens were made of two bonded CFRP adherents. The adherents consist of nine unidirectional laminas with 0° plies stacking sequences. Each specimen was manufactured together with a 50 mm initial debond length, an unadhered part at the head of the coupon. For manufacturing the ENF test coupons, specimens were prepared following the ASTM D7905 [134] standard. As with the DCB specimen, the ENF specimens were made of two bonded adherents that had nine unidirectional plies 0° plies stacking sequences, with an initial debond length of 50 mm. Figure 40 represents the illustration of both DCB and ENF specimens, including dimensions.

HexPly M91/34%/UD194/IM7-12K prepregs (HEXCEL PRIMETEX™, Connecticut, USA) – a UD carbon-epoxy prepreg which generally used for cutting-edge high technology aerospace applications – was employed for the production of the both DCB and ENF test coupons. Moreover, UD adherents were joined together by means of three plies of FM300K™ (Solvay, Belgium).

FM300K^{TM} adhesive material, too, is one of the most widely used structural epoxy film adhesive where high bonding performance is expected. The using three layers of film adhesive corresponds to a total 0.6 mm bond-line thickness.

While being stick to the aerospace industry standards and materials official datasheet, The composite laminates were manufactured using the autoclave technique at 180 °C & 7 bar for 2 h, as well as CFRP adherents were joined together with curing by autoclave process at 180 °C & 3 bar for 2 h. Those pressure, time and heating quantities are, meanwhile, same as the SLJ and SSJ specimens, which are the main test setups for the experimental part of this work. Obviously, The principal reason behind using the same curing conditions is to make cartelization specimens identical to the main test coupons.

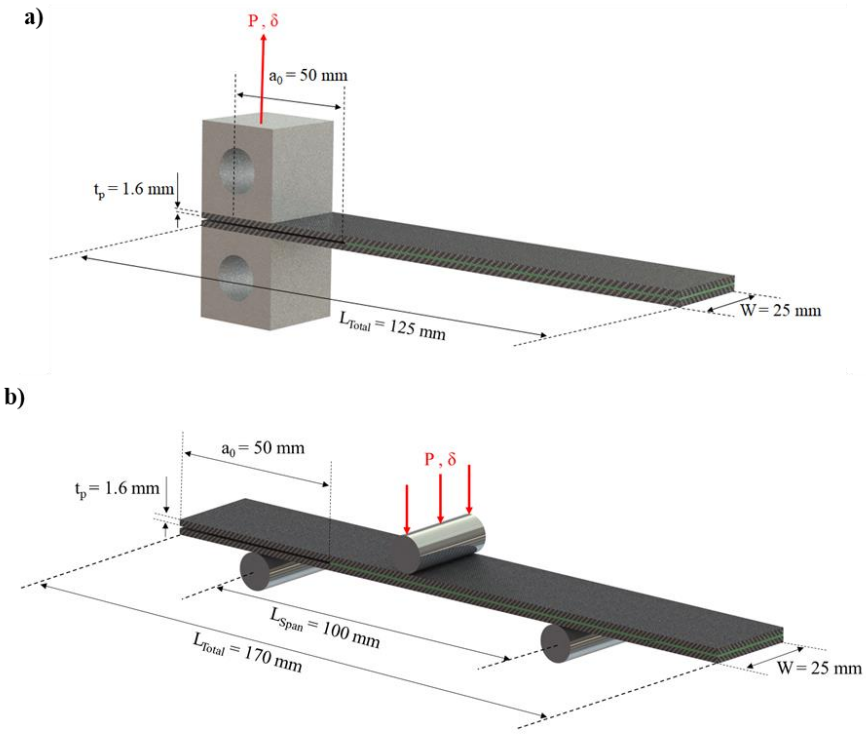

Figure 40. Illustration of the DCB and ENF specimens with dimensions.

Twelve specimens were tested for the ENF experiment, including six laser surface treated (LST) and six untreated (LSUT) coupons. For the DCB test, on the other hand, a total of eight tests were carried out, consisting of four LST and four LSUT surface

conditions. As a test setup for the DCB and ENF tests, within the laboratory conditions (23±2 C at 50%±5 relative humidity), mode I, and mode II (Fracture Toughness – Static) tests were performed using Shimadzu^{TM} AGS-X (Static ± 5 kN) tensile testing machine. For the DCB test, 5mm/min and ENF test 0.8 mm/min constant crosshead speed were utilized as given in corresponding standards. As a output, force-displacement curves are created with using recorded crosshead displacement and force values. Figure 41 gives test moment images of both the DCB and ENF tests.

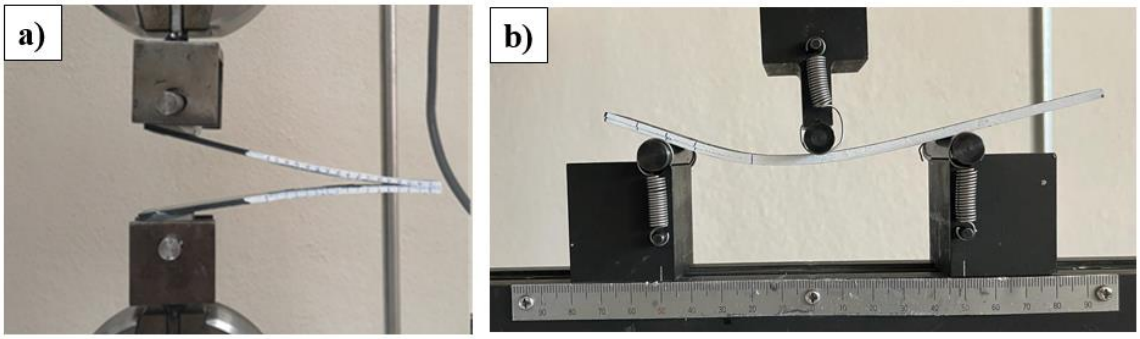

Figure 41. Test moment images of both the DCB and ENF tests.

The load-displacement curves of both LSUT and LST DCB specimens are given in Figure 42. DCB test results indicate that the average maximum load (P_{max}) values were detected as 42.08 N for the LSUT and 68.5 N LST for the LST surface conditions. Similarly, as can be seen in Figure 43, the mean value of P_{max} was detected as 736.3 N for the LSUT, and 904.8 N for LST ENF specimens. Overall, by means of the laser surface treatment technique, around 63% and 23% performance enhancement provided for adhesively bonded mode I and mode II behavior, respectively.

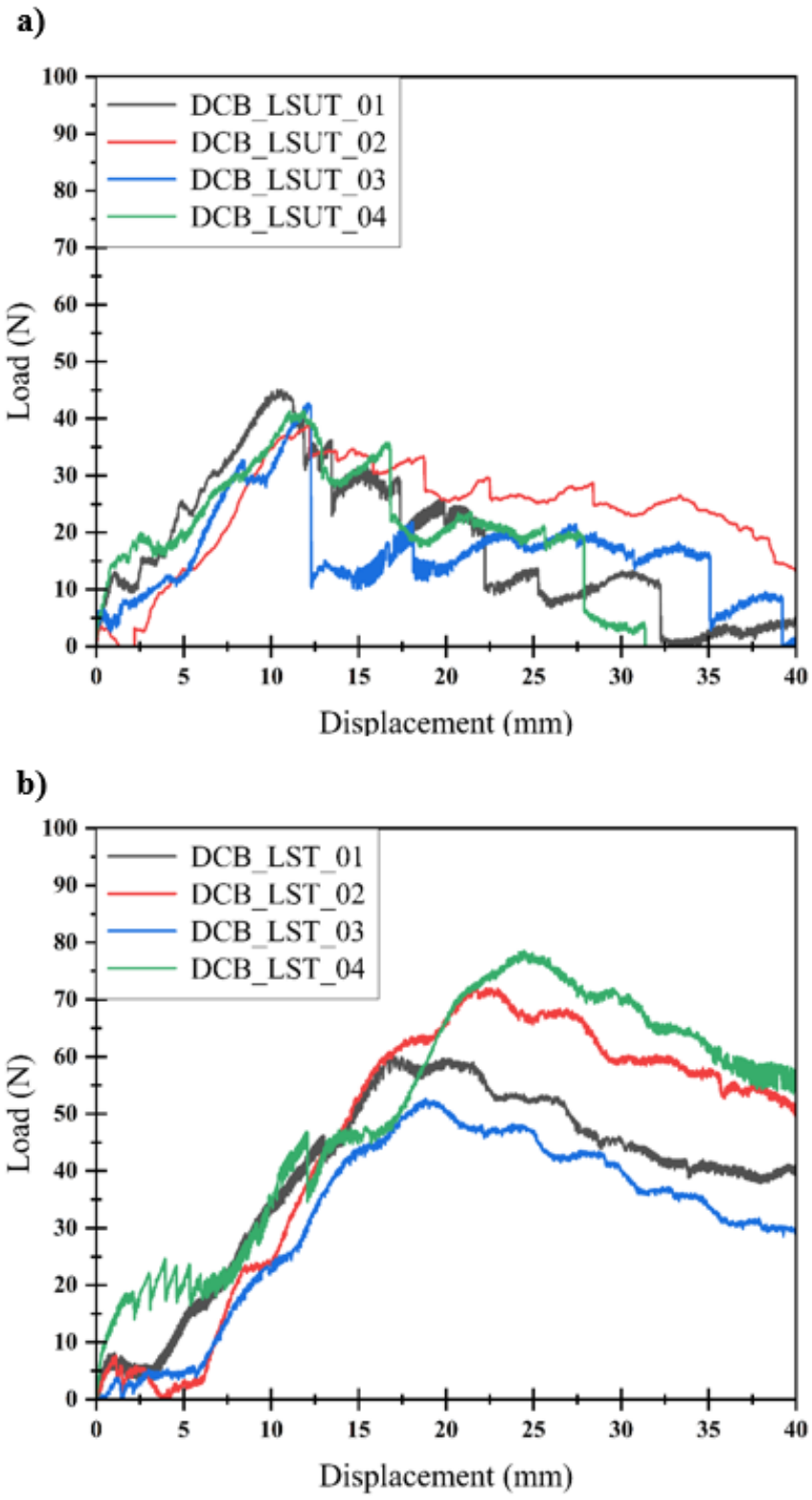

Figure 42. Load-displacement curves of the DCB specimens in a) LSUT and b) LST conditions.

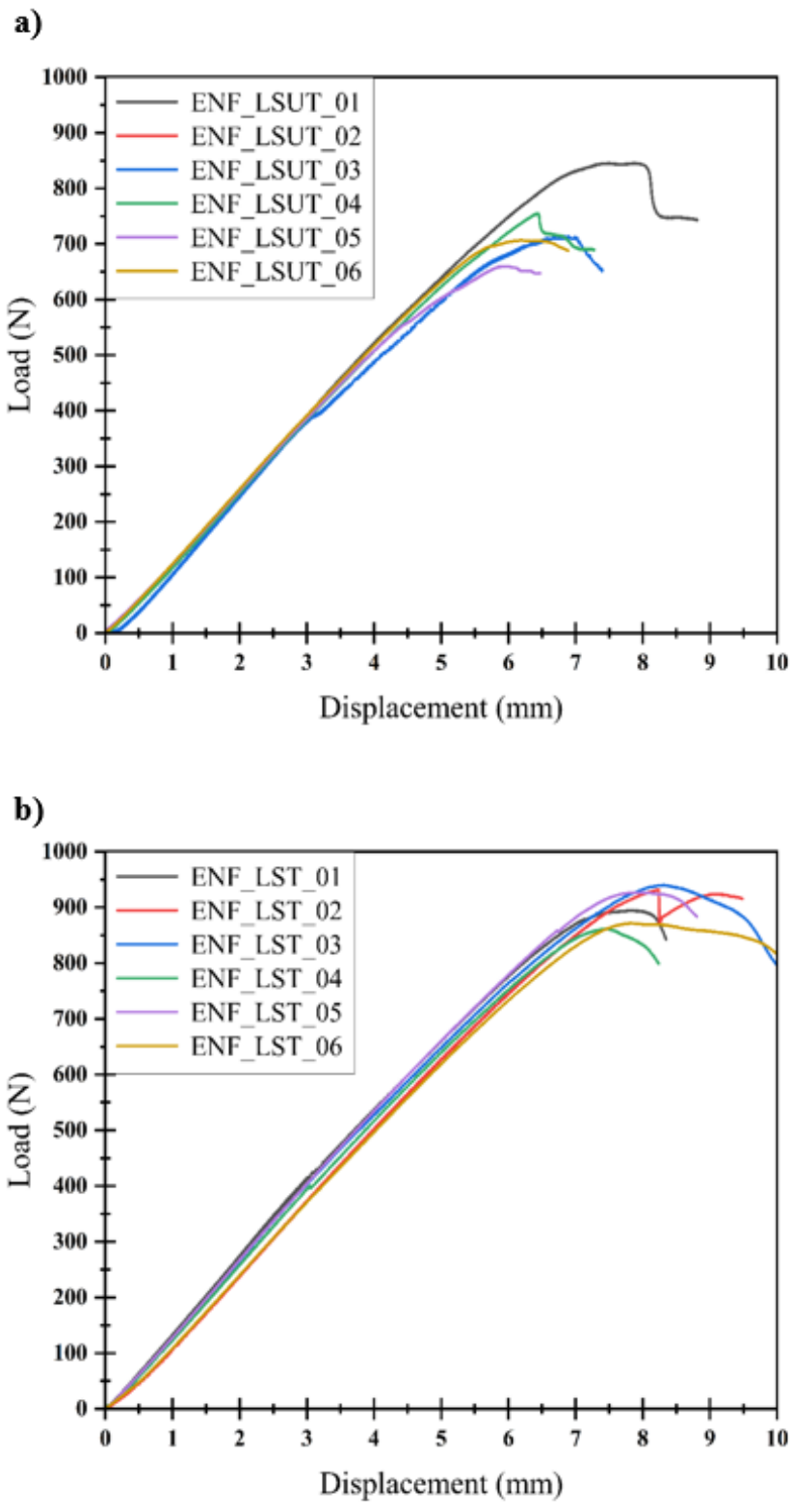

Figure 43. Load-displacement curves of the ENF specimens in a) LSUT and b) LST conditions.

As the main focus of the bonding characterization study, the G_{IC} and G_{IIC} values were evaluated from the DCB and ENF tests, utilizing the corresponding methods found in the standards. For the calculation of the G_{IC} value from the DCB test, there are three data reduction methods present in the ASTM D5528 standard [133]: modified beam theory (MBT), compliance calibration method (CC), and modified compliance calibration method (MCC). According to the aforementioned standard MBT is being suggested since results exhibit the most prudent outcomes for 80% of the specimens that were tested; hence, G_{IC} values calculated from MBT as follows:

$$G_{IC} = \frac{3P_{max}\delta}{2b(a + |\Delta|)} \tag{8}$$

P is the applied load, δ is the crosshead displacement, b is the specimen width, a is the delamination length (crack length), Δ is a value that is determined experimentally, generating a least squares plot of the cube root of compliance ($C^{1/3}$) as a function of delamination length. At the same time, for the mode II adhesive bonding characterization study, the G_{IIC} value was calculated via employing Compliance Calibration (CC) calculations in accordance with the ASTM D7905 standard [134], as follows:

$$G_{IIC} = \frac{3m(P_{max}a_0)^2}{2b} \tag{9}$$

Where m is the slope of the linear fit of compliance versus crack length cubed data, a_0 is the initial crack length, and b is the specimen width. In order to use as the Mode I and Mode II Critical Strain Energy Release Rate parameters, the average values of G_{IC} during crack propagation - G_{IC} propagation ($G_{IC,\,prop}$) - were taken, instead of G_{IC} initiation ($G_{IC,ini}$) value, which corresponds the value of GIC at the delamination onset. Hence the mean G_{IC} and G_{IIC} values determined from the DCB and ENF tests results as 396 and 1803 (J/m^2) for the LSUT configuration and 969 and 2666 (J/m^2) for the LST configuration. Therefore, it can be clearly seen that the G_{IC} and G_{IIC} values increased by about 144% for Mode I and 48% for Mode II behavior. Overall, it can be concluded as

the laser surface treatment technology empowered the mode I and mode II mechanical performance for the adhesively bonded CFRP structures at coupon level testing. Figure 44 presents G_{IC} - delamination length graphs for the LSUT and LST surface configurations.

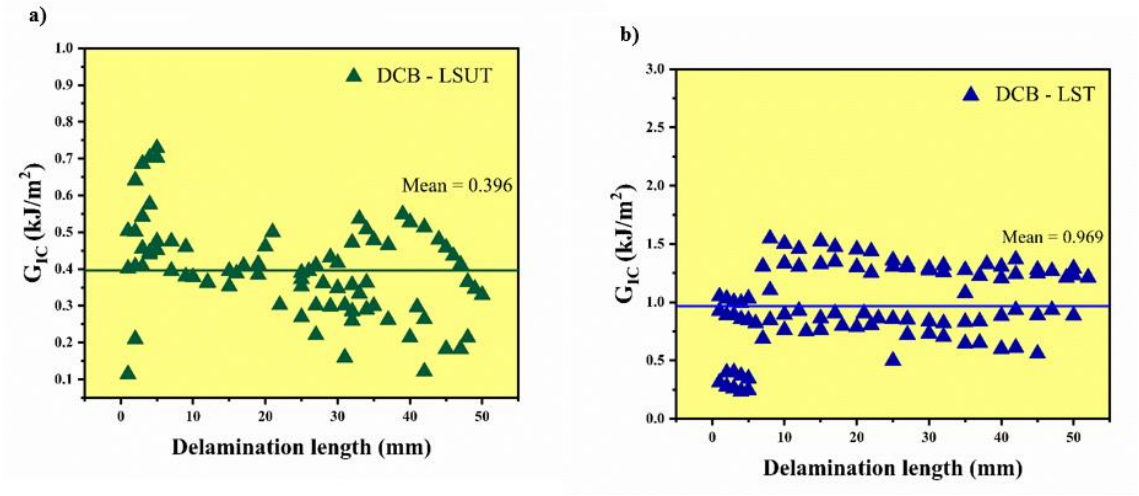

Figure 44. G_{IC} - delamination length graphs of DCB specimens for the LSUT and LST surface configurations.

4.2. Bonding Characterization - Numerical Work

FEA of both the DCB and ENF experimental tests were done in order for the numerical arm of the characterization study. To this end, 2-D FE models of each test were created and analyzed. The main reason behind executing the 2-D analysis is to provide computational efficiency to the nonlinear optimization study, which was done for the curve fitting operation. To build FE models, the exact same laminate stacking and dimensions of the aforementioned DCB and ENF specimens, as can be seen in Figure 4, were utilized. Bonding regions of the models were created using finer mesh size in order to provide a balance between the accuracy and computational work (Figure 45). The mesh size was selected as 0.3 mm. The mesh size calculation method for the CZM applications, given in detail in Chapter 6, was used determination of the mesh size. Instead of modeling bulk adhesive parts between the adherents, as has been done for the main FEA study in the section, the bondlines was modeled as single zero-thickness contact region that CZM

implemented. This setting, without doubt, was done in order for the being ensure the simplicity and accuracy of the optimization study. Figure 45 shows the created 2D models, finer mesh application on the contact region and utilization of the cohesive zones.

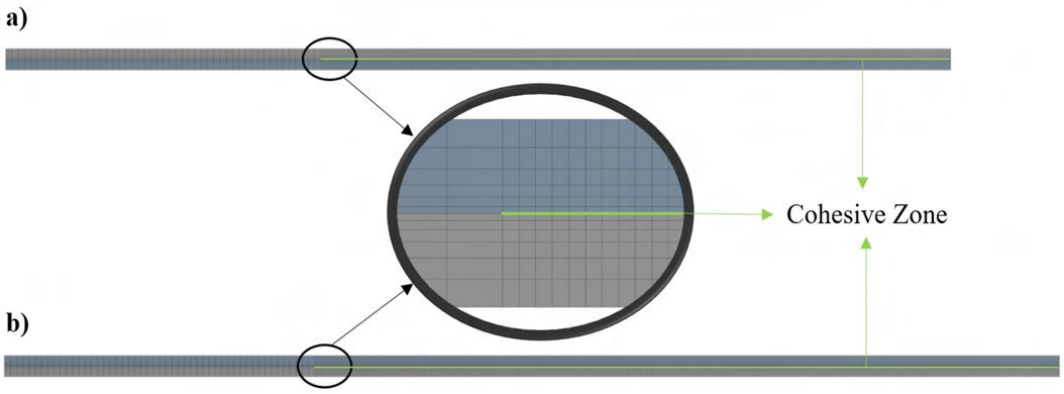

Figure 45. FEA models and mesh details of the a) DCB and b)ENF specimens.

Top and bottom adherents were created using UD CFRP composite laminas for both DCB and ENF specimens with only the 0° plies stacking sequences. Coupon parts were modeled as orthotropic and linear elastic using the material properties given in Table 2. Adhesive bonding behavior was implemented in the analysis by means of bilinear TSL, and analysis was generated under static loads with displacement control considering geometrical non-linearities. The details of the implementation and settings of the CZM technique whilst executing adhesive bonding of the CFRP composite specimens are presented in Chapter 6. Figure 46 shows the boundary conditions of the FEA of the DCB and ENF tests.

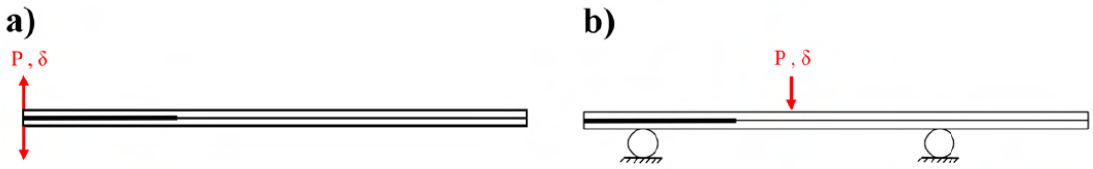

Figure 46. Boundary conditions of the DCB and ENF analysis.

2-D static FEA performed as large deformation analysis using sparse matrix direct solver while considering nonlinear geometric effects by using the full Newton-Raphson solution procedure. Automatic time stepping was used for the displacement increment during the analysis for all degrees of freedom via 1000 substeps as a maximum and 200 substeps as a minimum. Element type was adjusted as PLANE183 for the adherents and CONTA172 for the debonding contact with plane stress option. The penalty method was used as the contact algorithm and the contact detection was provided on Gauss integration points; here is the need to manually define the contact stiffness values in order for the use of ANSYS 18.1 version. The deformed FEA deformation results for the DCB ENF specimens are presented in Figure 47.

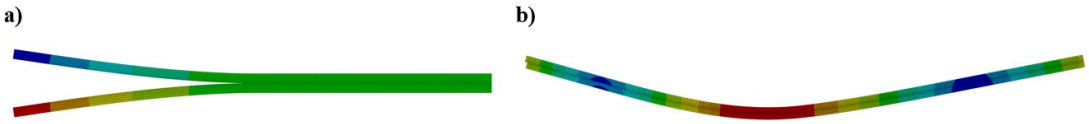

Figure 47. The deformed FEA models for a) DCB and b) ENF specimens.

In order to determine accurate maximum normal and tangential cohesive traction values, curve fitting was applied between the experimental and numerical force-displacement curves; it is for this that an optimization study was carried out using the ANSY software optimization module. For the experimental test results for each test, load-displacements curves and G_C values are used as constraints while, as cohesive parameters, corresponding maximum normal and tangential cohesive traction values were searched as variables. The Nonlinear Programming by Quadratic Lagrangian (NLPQL) method, a gradient-based algorithm to provide refined local optimization results, was employed. The parameters were identified after the FEA was run, and then Response Surface Optimization commenced. In this regard, Central Composite Design (CCD) based Design of Experiments (DOE) was created with five design points by utilizing Genetic Aggregation. As an example, the workbench scheme of the optimization study DCB specimens is given in Figure 48 - a similar scheme was used for ENF specimens.

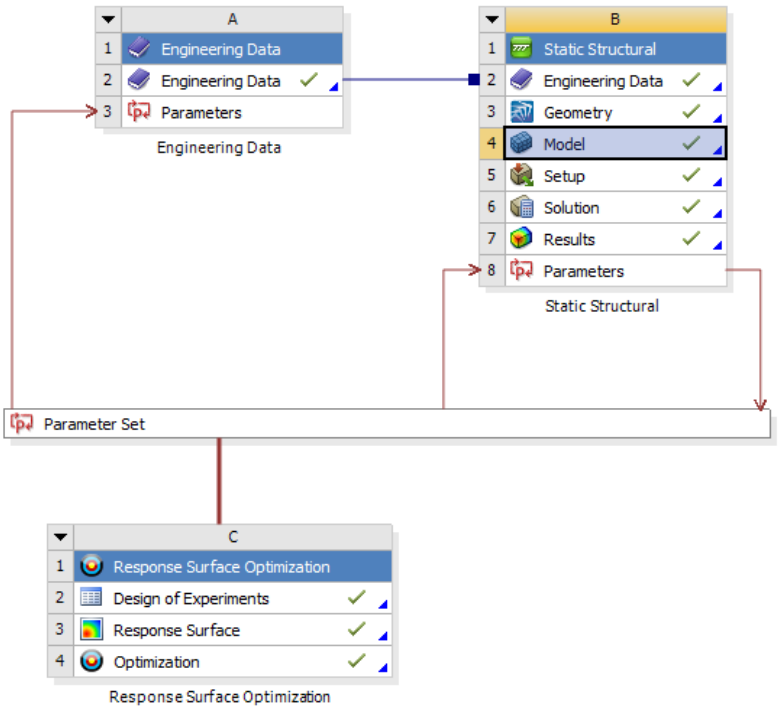

Figure 48. Workbench scheme for the optimization study of the DCB test.

The CZM parameters, above all, specific to the CFRP materials, adhesive type and surface conditions unearthed by means of the applied collective bonding characterization method using experimental results and numerical optimization works are summarized in Table 5.

Table 5. CZM parameters for LSUT and LST surface conditions.

Parameter	Symbol	LSUT Specimen	LST Specimen
Maximum Normal Cohesive Traction (MPa)	T_n^{max}	11.6	32.5
Maximum Tangential Cohesive Traction (MPa)	T_t^{max}	20.5	34.2
Mode I Critical Strain Energy Release Rate (J/m^2)	G_{IC}	396	969
Mode II Critical Strain Energy Release Rate (J/m^2)	G_{IIC}	1803	2666
Mode I Cohesive Stiffness (N/mm^3)	k_I	15000	15000
Mode II Cohesive Stiffness (N/mm^3)	k_{II}	4000	4000

CHAPTER 5

FINITE ELEMENT ANALYSIS METHODOLOGY

Numerical analysis of both adhesively bonded CFRP composite SLJ and SSJ geometries were examined using Finite Element Analysis (FEA) technique. For this purpose, ANSYS Inc. Products Release 18.1 FEA software was employed in order to predict the load-displacement curves, stress distribution, and detailed failure investigation of the specimens, carrying out static-structural simulations. In all executed analyses, same as aforementioned experimental test specimens and conditions, three-dimensional FEA models were created and analyzed. In order to observe bonding behavior Cohesive Zone Modeling (CZM) technique was incorporated into the analysis under static loads. Due to the occurring geometrical nonlinearities because of the debonding, which also can be expressed as contact nonlinearity, analyses were run in a nonlinear computations frame. Through the CZM parameters obtained from the bonding characterization studies for the laser surface treated bonding, the change of mechanical behavior in the case of laser treatment enhancement was presented.

In both SLJ and Skin-Spar Joint analysis, force direction changes as the deformation occurs, which transforms the cases into nonlinear analysis due to the debonding formation. While wielding the implicit solver, it is seen that embedding cohesive elements to simulate the separation of two bonded surfaces possesses convergence difficulties by virtue of utilizing the Newton-Raphson method to solve nonlinear static analysis. In order to overcome such convergence issues, usually seen in crack initiation points, one must use automatic stabilization to stabilize the interface delamination [131,135]. In ANSYS software, automatic stabilization is provided as an artificial damping coefficient (d), which is chosen 0.0001s in this study, in order to be as close as to the zero and also be smaller than the minimum step size to avert the aberrance of the numerical results by minimizing the effect of the artificial damping [98].

While executing any kind of FEA, it is crucial to properly define the mesh structure to achieve accurate results within a minimum time; herewith, discretizing the bodies with optimum element size is indispensable to catch the ideal trade-off between

precision and efficiency. Particularly in the adhesively bonded CFRP composite material analysis with CZM application, due to the being mostly computationally costly since the analysis of the debonding is nonlinear, and the materials are orthotropic. Therefore, in order to find out the optimum mesh size in the designated areas while executing FEA with CZM, instead of performing mesh sensitivity analysis, one can estimate proper cohesive zone mesh size (l_e) by using Turon's approach [136] as follows:

$$N_e = \frac{l_{cz}}{l_e} \tag{10}$$

Where l_{cz} is the cohesive zone length and l_e is the mesh size in the direction of crack propagation. The l_{cz} value can estimate from the following:

$$l_{cz} = ME\frac{G_c}{T^2} \tag{11}$$

Where E is the Young modulus of the material, G_c is the critical energy release rate, T is the maximum interfacial strength, and M is a parameter that depends on each model.

The M value was chosen as 1, since the Hillerborg's model suggests it for similar applications; and also, as suggested by Turon, the N_e value was selected as 3 [136–138]. With regard to this, the corresponding optimum mesh sizes for the adhesive bonding area have become 0.32 mm for the SLJ specimens and 0.8 mm for the SSJ specimens. While the contact areas were discretized according to the calculations above, the rest of the models meshed via using higher mesh sizes in order to provide computational efficiency since the CZM applications require high computational power inherently – mostly because of the nonlinear calculations. The mesh density, in other words, was adjusted in the contact areas to be high relative to the rest of the part, and a smooth transition was applied between the different zones which have dissimilar mesh sizes. On top of that, while executing the debonding simulation by means of creating contact points between the two

parts, the Gauss points are employed; therefore, the meshes and nodes were directly matched in order to provide confrontation and proper contact detection.

As the most compelling part of employing the CZM technique, convergence challenges may arise while executing nonlinear FEA. These convergence issues mostly emerge in the beginning of the softening stage, where the fracture first observe, due mainly to the abrupt stiffness transforms. For that reason, the step size setting is curial for the simulation of the adhesive bonding with CZM. In other words, besides the mesh density definition, the load or displacement incrementation in a dedicated time can highly affect the simulation outcomes. However, at the same time, too much step size increases the solution time and computational work. It is for this that, in this study, to create the tradeoff between step size and solution time, displacement incrementation optimization, too, was done in order to reduce the solution time of the nonlinear analysis and obtain accurate results. To this end, automatic time stepping, an algorithm that provides adding additional load increment during the analysis if the convergence is not obtained, was used with the minimum sub-step size of 300.

5.1. Single Lap Joint Geometry

3-D FEA model of the SLJ geometry was created adhering to the experimental specimens, as can be seen in Figure 49; it is for this that top and bottom CFRP composite adherents and bulk adhesive part were modeled separately via using unidirectional carbon epoxy composite laminates and homogeny epoxy adhesive. Therefore, CFRP adherents were modeled as orthotropic and linear elastic, on the other hand, the bulk adhesive part was modeled as linear elastic.

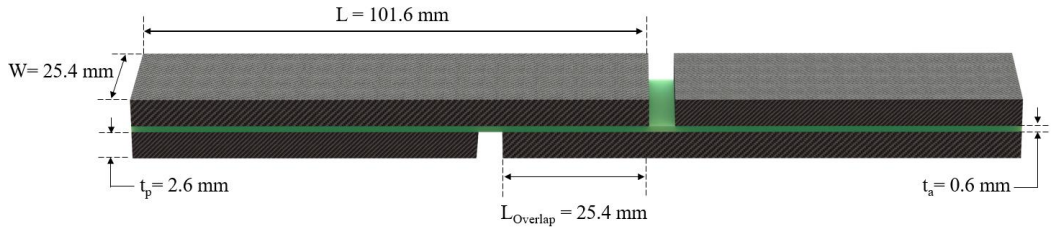

Figure 49. 3-D illustration of the SLJ geometry with dimensions.

While the CFRP parts were discretely meshed for each ply according to the after-mentioned stacking sequences of the experimental coupons, the bulk adhesive part, too, was discretely meshed to be three ply through the thickness due mainly to three ply of adhesive employed in the experimental specimens. Figure 50 shows the meshed SLJ FEA models.

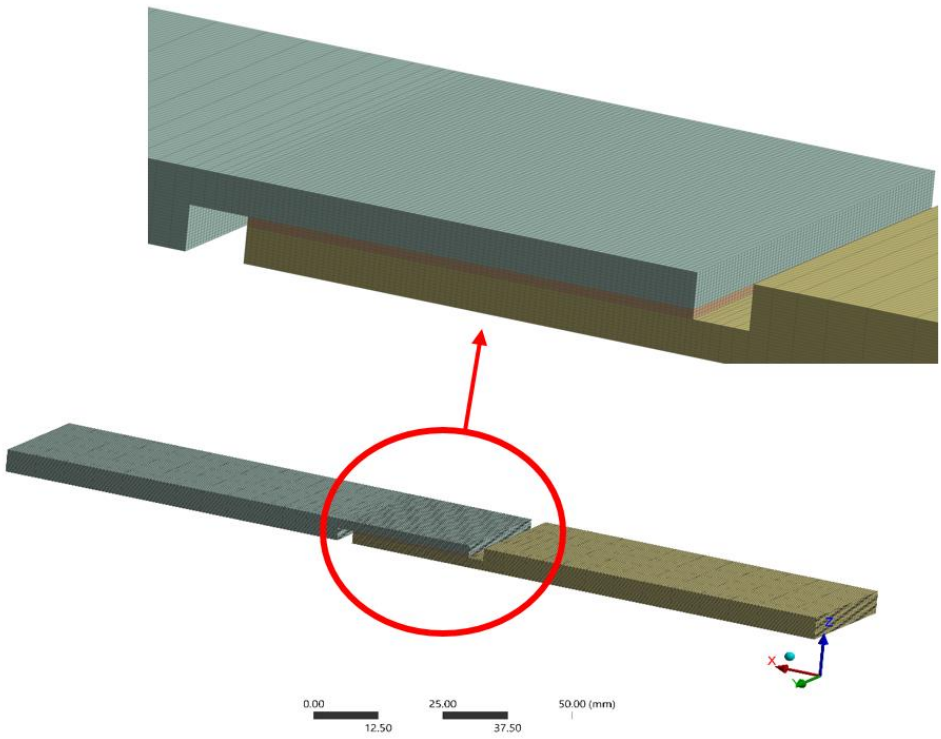

Figure 50. Mesh details of the SLJ FEA model.

In order to simulate the interphase region in the adherents and adhesive contact area, cohesive elements were placed on the contacts, as illustrated in Figure 51. Both adherents and adhesives were modeled by employing eight-node solid elements (SOLID185), at the same time, 3-D eight-node zero thickness contact elements (CONTA174) were placed in the contact regions (Figure 51). By implementing bilinear traction separation law to the contact elements CZM technique is become incorporated with the analysis. As the fundamental requirement of the FEA method, optimum mesh size was couched considering the balance between the computational work and accuracy of the analysis, therefore, higher mesh refinement was applied on the overlap region where debonding occurs.

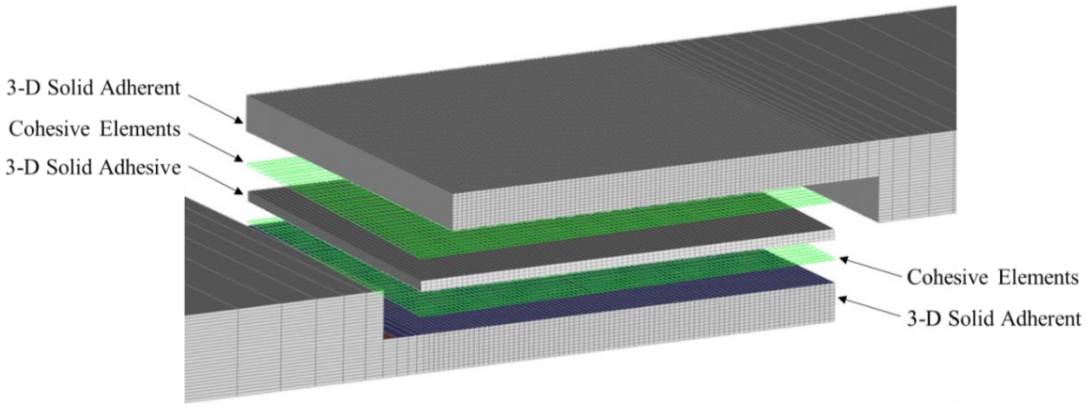

Figure 51. Details of the SLJ model.

As boundary conditions, identical to the experimental test conditions, the tensile force was applied through uniform displacement along the longitudinal axis, whereas the opposite edge is completely fixed (Figure 52).

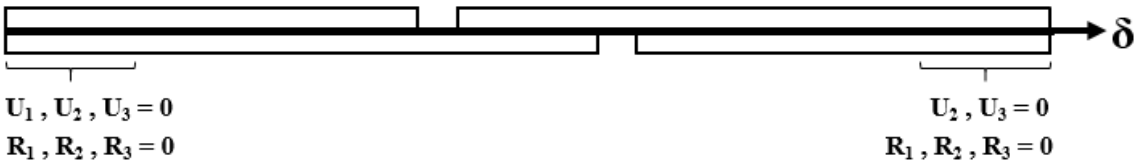

Figure 52. Boundary conditions for the SLJ test analysis.

5.2. Skin-Spar Joint Geometry

3-D FEA models of the SSJ geometry was created as identical to the experimental specimens, as can be seen in Figure 53; for this purpose, CFRP composite skin/spar parts and bulk adhesive part were modeled separately via using woven carbon epoxy composite laminates and homogenous epoxy adhesive. Hence, CFRP parts were modeled as orthotropic and linear elastic, as well as bulk adhesive was modeled as linear elastic. AS in the SLJ models, while CFRP parts were discretely meshed for each ply according to

the aforementioned stacking sequences of the experimental coupons, bulk adhesive part was discretely meshed to create three ply in the through the thickness direction because of three ply of adhesive employed in the experimental specimens. Figure XX shows the meshed SSJ FEA models.

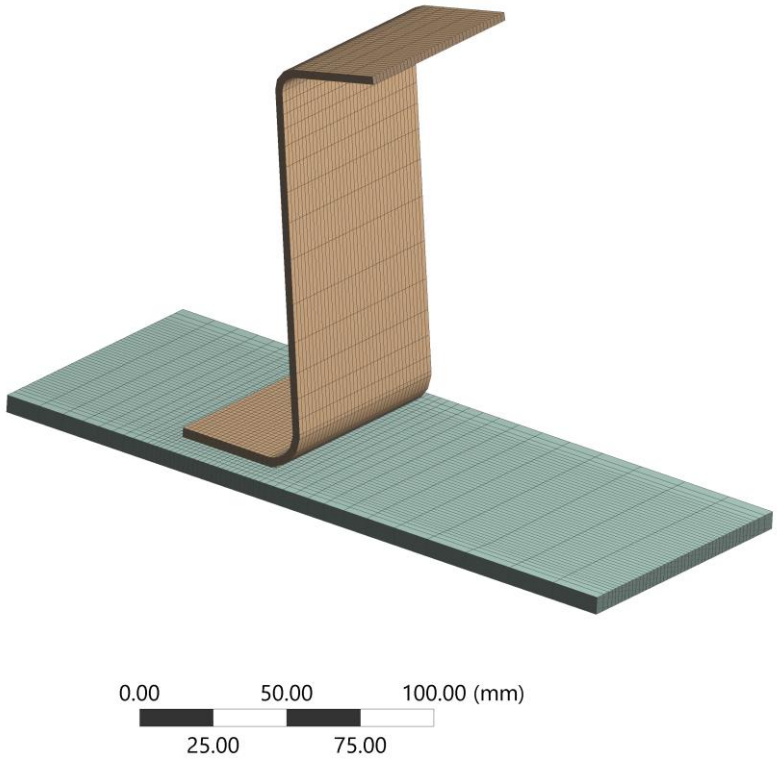

Figure 53. Mesh details of SSJ specimen FEA models.

Cohesive elements were placed on the contacts in order to simulate the interphase region in the adherents and adhesive contact area, as illustrated in Figure 54. Both adherents and adhesives were modeled by employing eight-node solid elements (SOLID185), meanwhile, 3-D eight-node zero thickness contact elements (CONTA174) were placed in the contact regions (Figure 54). By implementing the bilinear traction separation law to the contact elements, the CZM technique has become incorporated into the analysis. On top of that, higher mesh refinement was applied on the overlap region where debonding occurs to provide optimum mesh size considering the tradeoff between the computational work and the accuracy of the analysis.

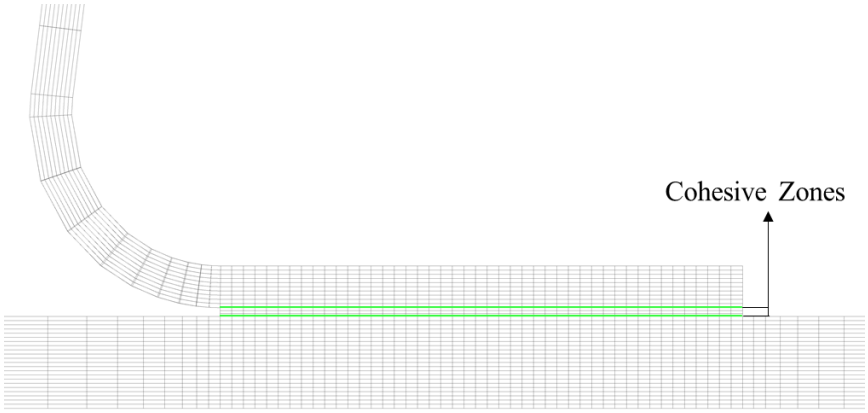

Figure 54. Details of the SSJ FEA model.

As boundary conditions, a tensile force was applied through uniform displacement from the upper incline part of the spar while the skin part was completely fixed (Figure 55).

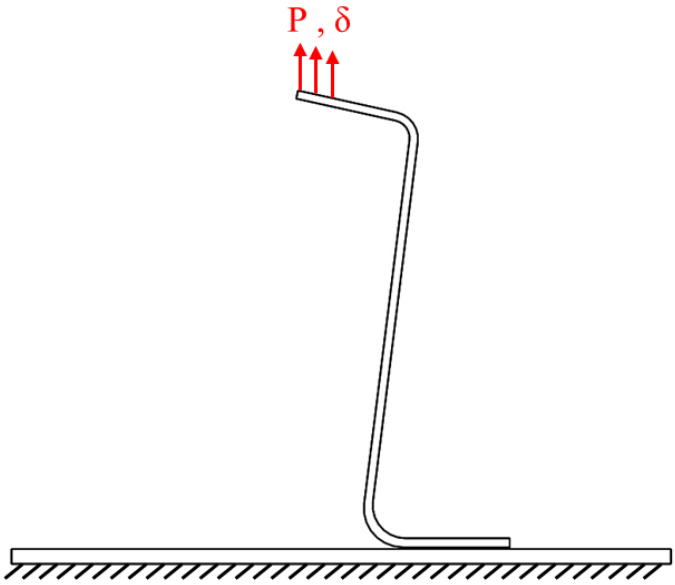

Figure 55. Boundary conditions of the SSJ analysis.

CHAPTER 6

RESULTS AND DISCUSSION

This section contains the results of the executed finite element analysis for both the Single Lap Joint (SLJ) and Skin-Spar Joint (SSJ) coupons, presenting load-displacement curves, strength magnitudes, stress gradient on the bonding surfaces and stress-time graphs. In this way, as a result of applied FEA methodology – numerical analysis of the adhesively bonded CFRP composite structures using CZM technique – the crack initiation and propagation formed in the interface between adhesive and adherents was simulated on the not only coupon level but element level test setup models. On top of that, experimental and numerical results are compared in order to investigate the compatibility of the presented FEA methodology for the analysis of the laser surface treated adhesively bonded CFRP structures. Thus, the accuracy and pertinence of the processes that start with the characterization and then include modeling and analyzing are discussed.

6.1. SLJ FEA Results

Figure 56 presents the numerical load-displacement results - for the LSUT and LST configurations - obtained through nonlinear FEA employing cohesive elements placed on both the upper and lower contact regions between the adhesive and adherents.

Deformed 3-D FEA models, which are at the point where the complete debonding occurs, can be seen in Figure 57. Besides being an execrated representation in order to provide a better understanding of the debonding, the given deformation results belong to the exact moment of the failure, which is a moment that maximum load is detected.

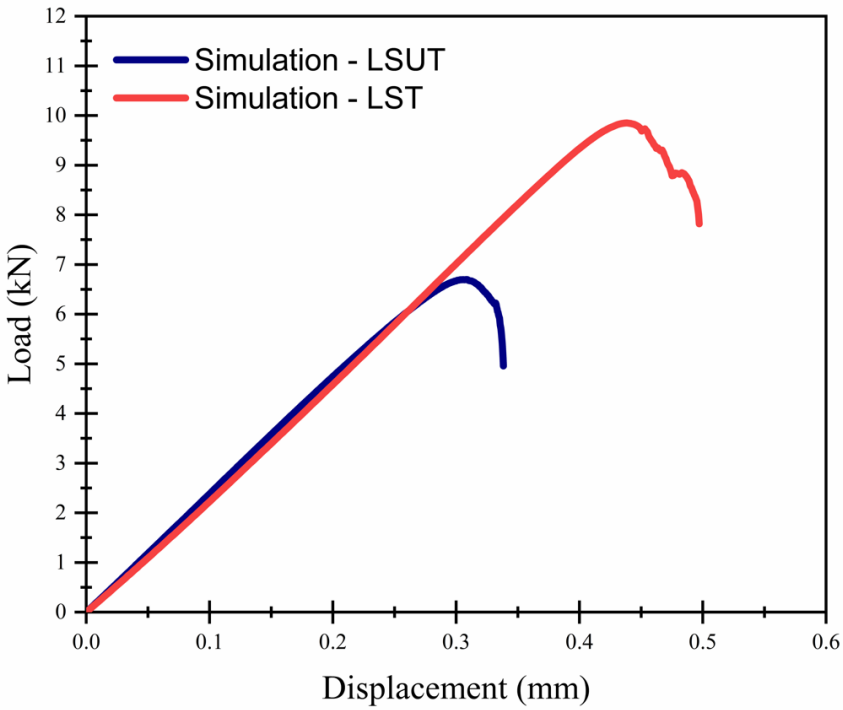

Figure 56. Load-displacement results for the LSUT and LST configurations.

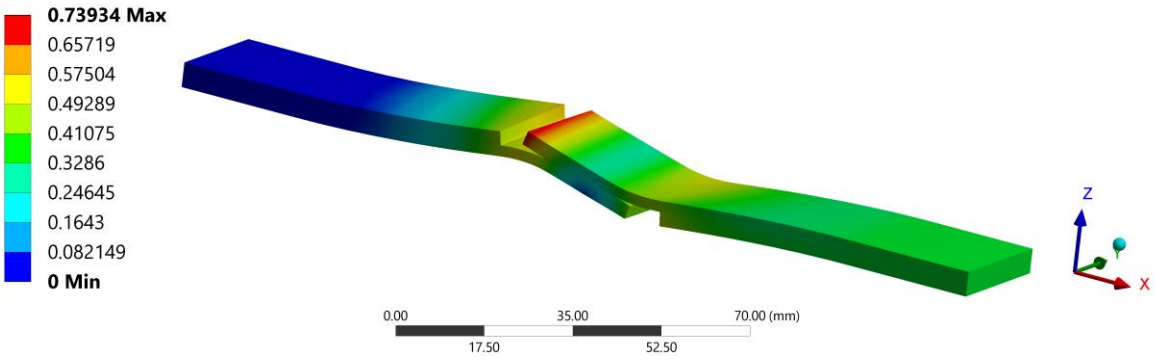

Figure 57. Deformed 3-D SLJ FEA model.

The comparisons of the experimental and FEA results are given in Figure 58, comparing load-displacement values of the adhesively bonded SLJ coupon with LSUT and LST surface conditions.

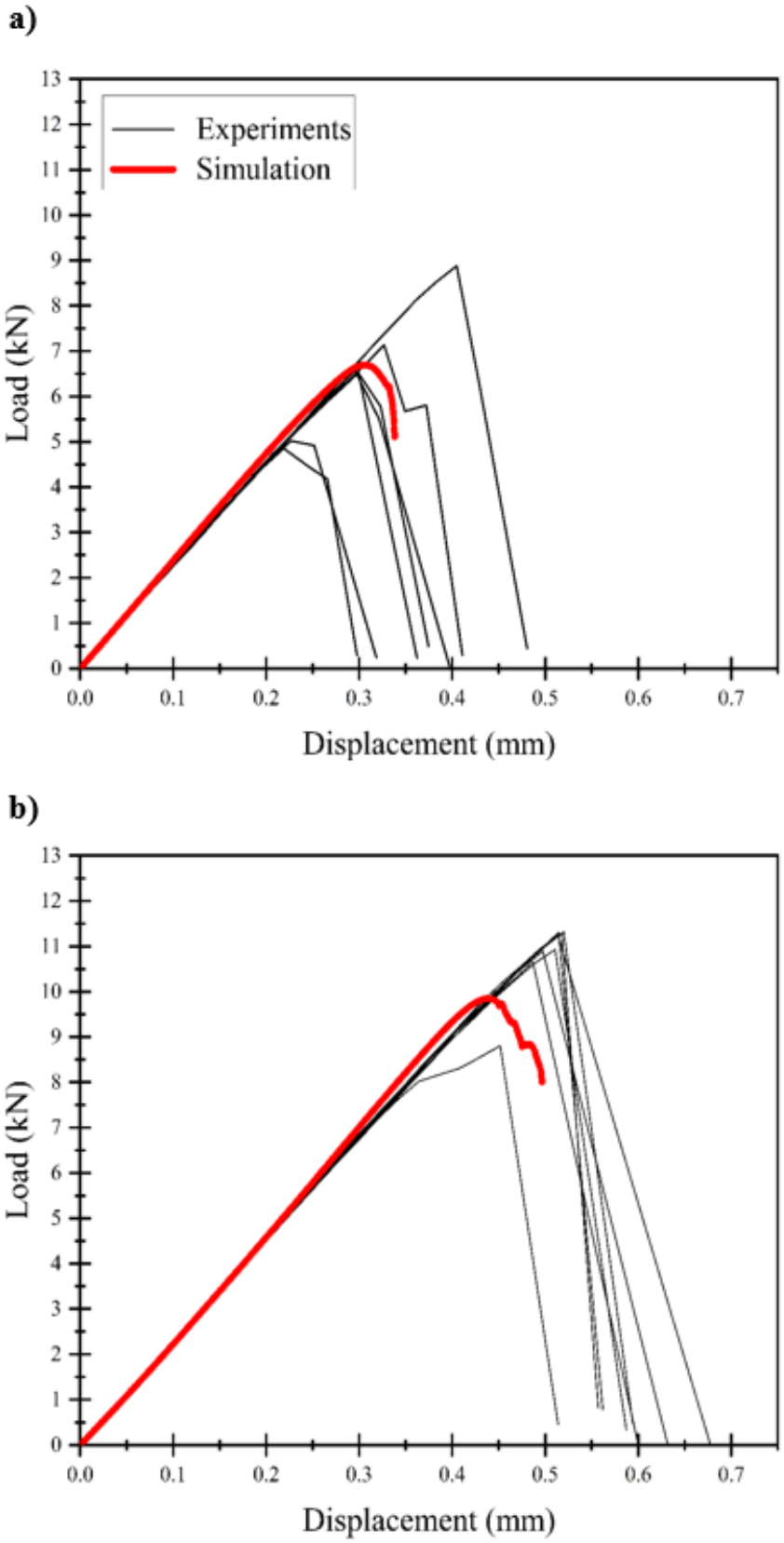

Figure 58. The comparison of the experimental and FEA load-displacement curves of SLJ specimens for a)LSUT and b)LST configurations.

The load-displacement comparisons for both LSUT and LST specimens set forth that the presented FEA methodology with the determination of the CZM parameters by means of the aforementioned characterization study is quite successful in order to predict the adhesive bonding behavior of a CFRP composite SLJ structures. In other words, not only failure load and displacement values but the debonding behavior that starts linearly and ends with a sudden fracture is accurately simulated. The behavior after the failure, on the other hand, does not represent the actual experimental behavior since there is no damage capability implemented to the FEA model for both bulk adhesive and adherent materials.

On top of that, it can be clearly seen from the experimental-numerical comparison results for the LSUT and LST surface conditions that the effects of the surface treatment on the bonding behavior and occurring differences resulting from different surface conditions are exhibited in the simulation, which shows the accomplishment of the presented methodology. Overall, as a result of the comparison of the simulation and averaged experimental results, the deviation rate in the load was calculated as around 4% and 8% for LSUT and LST specimens, which are quite acceptable.

In order to indicate peel and shear stresses that occur on the contact region, where the bonding observe, both peel and shear stress distributions on the interface surface are shown in Figure 59. Those stress distributions, admittedly, correspond to the time when the maximum peel stresses were seen, which is 0.18^{th} second for the LSUT and 0.28^{th} second for the LST configurations.

The stress-location formations in the form of hyperbolic paraboloid curves are in line with the expectations which are commonly seen in the studies for the adhesively bonded structures in the literature and analytical approaches. Thus, both maximum peel and shear stress values are located at the edges of the overlap region where stress singularities are noticed. For the upper and lower adherents, both peel and shear stress values are concentrated on the side of the contact zone closest to the applied force due to adherent rotation and adhesive thickness effects.

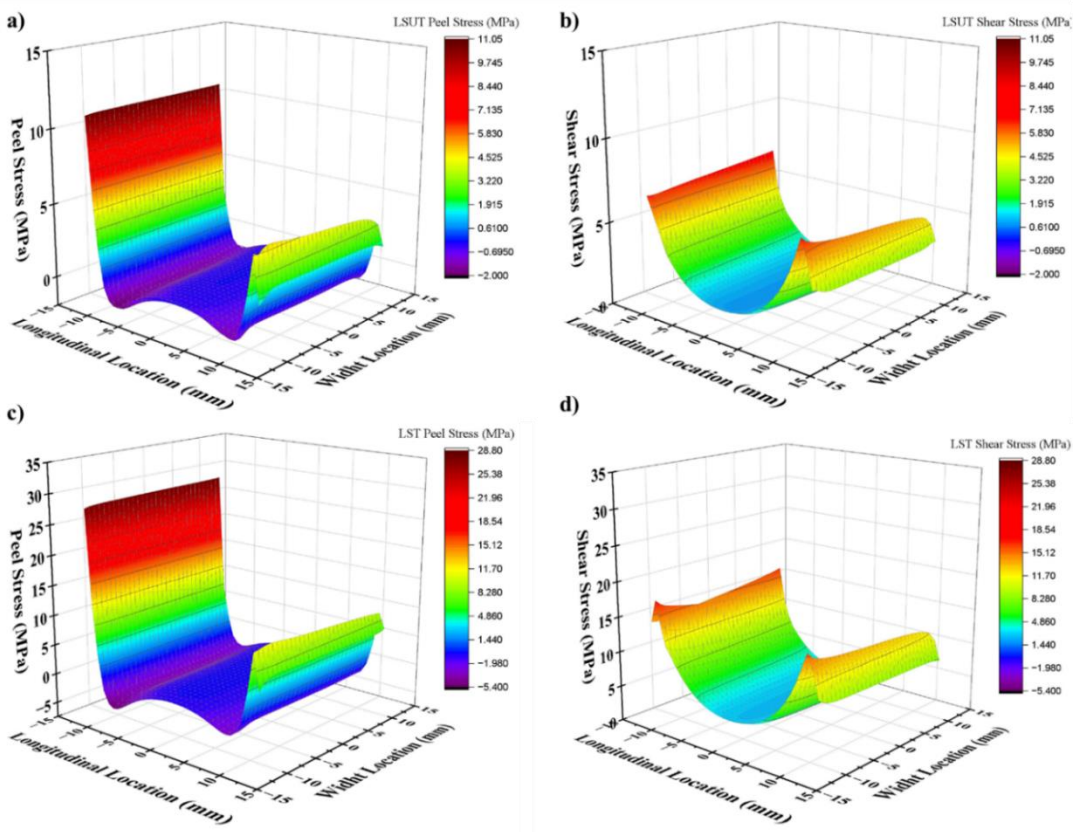

Figure 59. a) Peel and b) shear stress distributions for the LSUT and c) Peel and d) shear stress distributions for the LST SLJ specimens.

One can clearly see when comparing the bonding area maximum stress values of the LSUT and LST specimens that through the laser surface treatment operation, maximum peel and shear stress values increase; on top of that, those increases are seen especially in the region where the crack initiation begins, which leads to debonding failure inside adherents. These results are also correlated with the experimental results, as can be seen in the after-failure bonding surface pictures of the LSUT and LST specimens (Figure 36). Thus, even though it does not provide a definitive interpretation of the failure mode, the predisposition to adherend failure after the laser surface treatment, which was also observed in the experimental results, can successfully be extrapolated by exploiting the present methodology.

In addition to those, as can be seen in Figure 60, the comparisons of the peel and shear stress values during the debonding time are set forth in order to understand the main mechanism behind the fracture during the loading. The stress-time comparisons indicate that the imitation of the crack for the SLJ geometry is intensely based on peel stresses

occurring at the edges of the contact regions; thereafter, the main phenomena behind the propagation of the crack and, eventually, completely debonding are turned out to be shear stresses. Hereby, as general sight, the mix-mode debonding behavior eventuates with the shear stress intensity fracture. This phenomenon can be noticed from the maximum stress-time graph of the LSUT and LST specimens for both peel and shear stress components (Figure 60).

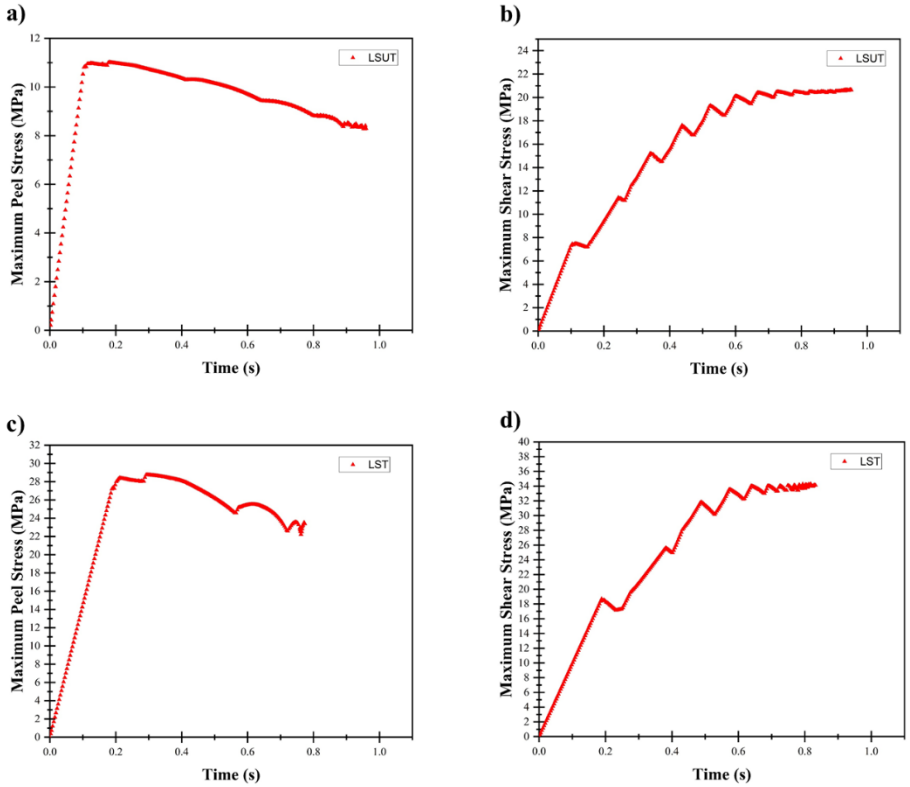

Figure 60. Stress-time graph of the SLJ specimens for a) peel, b) shear stress for LSUT condition, and c) peel, d) shear stress for the LST conditions.

Figure 61 provides the average shear strength comparisons between the numerical and experimental results for the SLJ specimens with both LSUT and LST surface conditions. It can be easily said that when one searches for the compatibility of the presented FEA methodology on a coupon test setup, quite convenient results were obtained; that also reveals the success of the collaborative utilization of the aforementioned characterization and CZM techniques in order to predict the crack initiation, propagation and maximum strength of an adhesively bonded SLJ geometry.

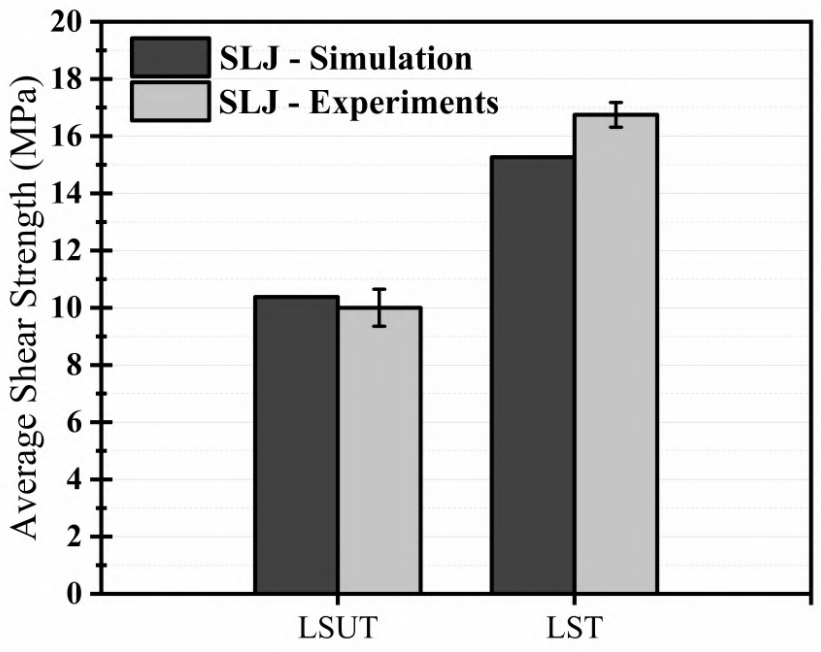

Figure 61. Average shear strength comparisons between the numerical and experimental results for the SLJ specimens with both LSUT and LST surface conditions.

Consequently, for a coupon-level test setup, employing bilinear TSL on the contact region to simulate the interphase region between adherents and adhesive materials is a prospering method for numerical investigation of the bonding behavior. Therefore, though it is open to further development, it is one of the relatively easy and accurate techniques for adhesively bonded CFRP composite structures, provided that it is used together with the method for determining CZM parameters for different surface conditions described in the characterization section.

6.2. Skin-Spar Joint FEA Results

Figure 62 provides the numerical load-displacement curves of the deformed SSJ models for the LSUT and LST configurations. Deformed 3-D SSJ FEA models are presented in Figure 63. This deformation result image is taken at the moment when failure is observed; for this reason, the given deformation distributions and magnitudes belong to the point that complete failure occurs, which is the second that maximum load is detected.

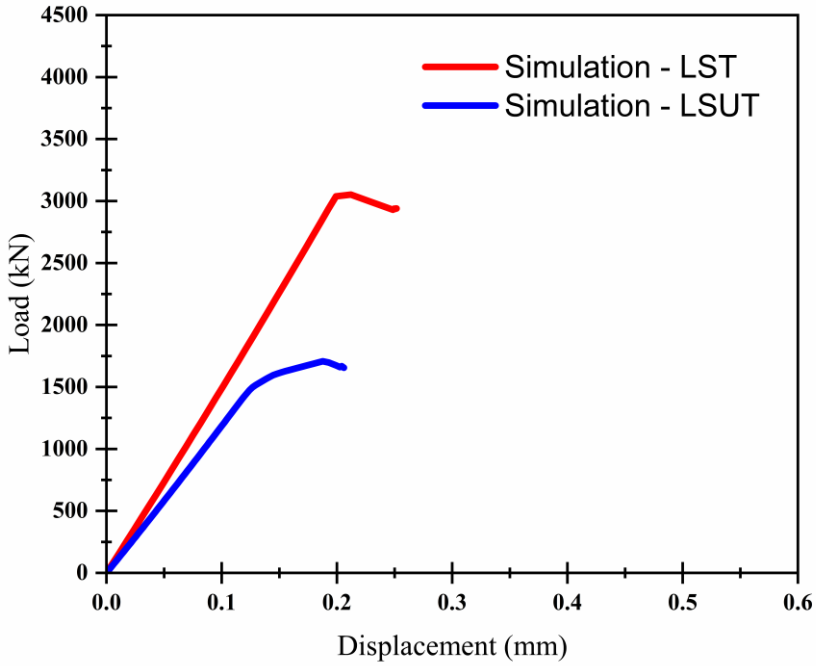

Figure 62. Load-displacement curves for SSJ specimen analysis.

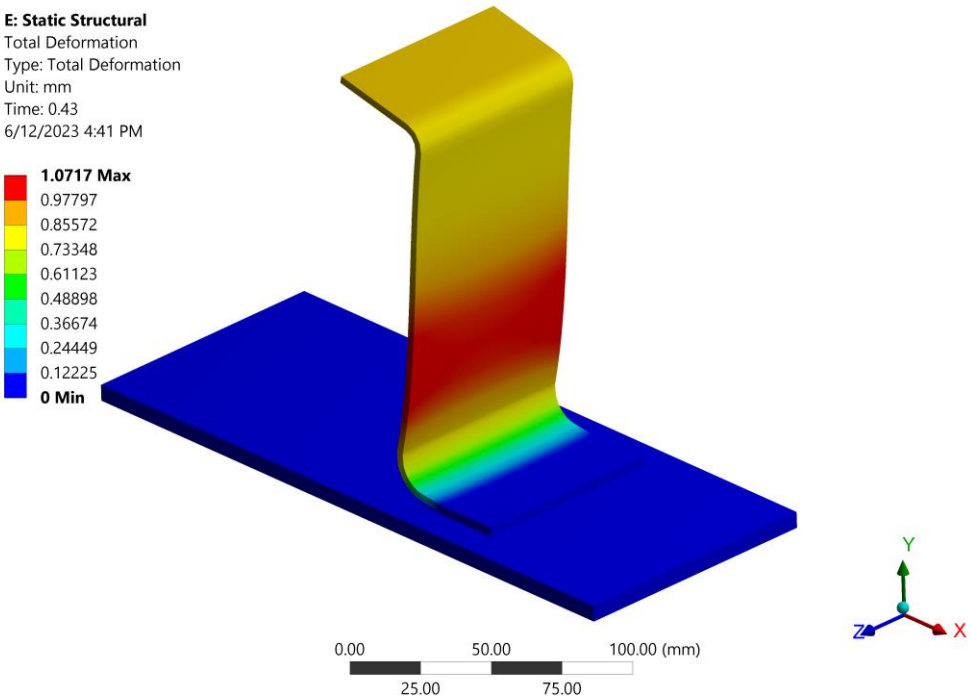

Figure 63. Deformed 3-D SSJ FEA model.

The comparisons of the experimental and FEA results for the SSJ tests are given in Figure 64, comparing load-displacement values of the adhesively bonded specimens with LSUT and LST surface conditions. According to comparison results, the deviation rate in the load was calculated as around 45% and 5% for LSUT and LST specimens. Therefore, proximate results are achieved with the FEA of the SSJ coupons employing the CZM method to simulate adhesive behavior.

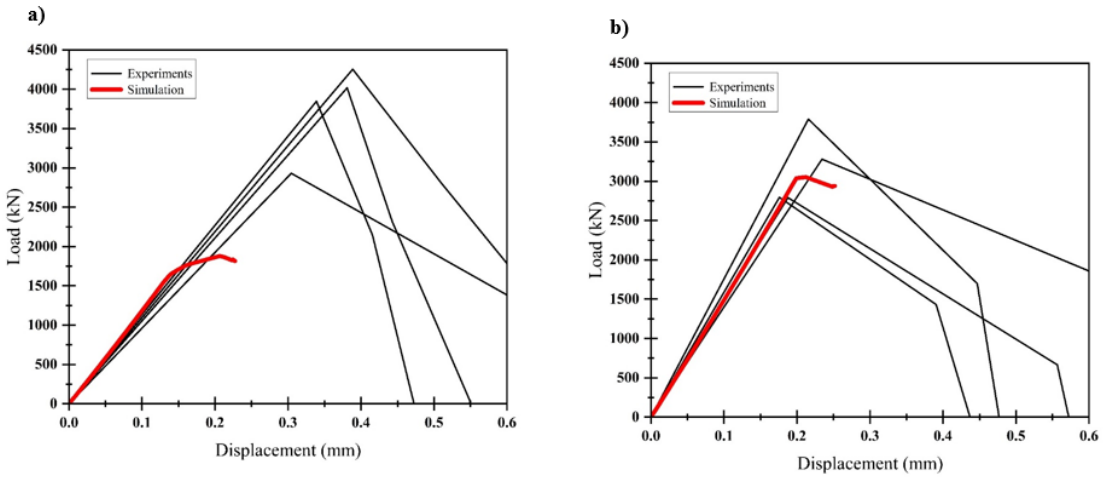

Figure 64. The comparison of the experimental and FEA load-displacement curves of SSJ specimens for a)LSUT and b)LST configurations.

As can be seen from Figure 63, the load-displacement results are nearly compatible with the LST surface configuration. Nevertheless, larger errors were obtained for the load-displacement curves of LSUT specimens. The main reason behind the observing inaccurate results is the manufacturing method utilized in order to joint SSJ test specimens. In other words, while characterizing the bonding using the autoclave technique, employing those characterization outputs for a joint that manufactures with an out-of-autoclave technique triggered the occurrence of results that are not accurate. Therefore, it can be concluded that every condition, including curing technique, between characterization and actual test specimens must be the same in order to obtain the correct result. Unfortunately, utilizing the CZM parameters that are estimated or taken from other studies will not work in terms of giving appropriate results while executing numerical analysis of the adhesively bonded CFRP structures. However, in the case where proper adhesion is achieved, and the importance of manufacturing technique is eliminated, the

applied method has become successful in terms of damage estimation, as seen in the LST specimens. Therefore, comparison results of the SSJ joint with LST configuration indicate that adhesive bonding behavior can also be successfully simulated in an element-level test configuration.

Bonding region peel and shear stress distributions at the second that maximum peel stresses are observed are graphically illustrated for the LST configurations, which is the configuration that accurate result obtained, in Figure 65. Those stress distributions, on the other hand, were taken from the spar surface of the SSJ coupons when the crack initiation begin, which is at 0.869th second of the simulation time. Since the results do not indicate the actual behavior, the stress distribution graphs of the LSUT specimens are not shown. The stress distributions disclose that, as can be noticed from Figure 65, both maximum peel stresses are located at the edge that is nearest to the applied force. The same location results also emanated for the shear stress distributions. One can easily forecast that the failure on the joining region is formed due mainly to the peel stresses since shear stress values are relatively less than the peel stress values at the initiation of the crack. Yet, considerable shear stresses, too, occur on the contact surface because of the applied misaligned force by means of the S shape geometry of the spars.

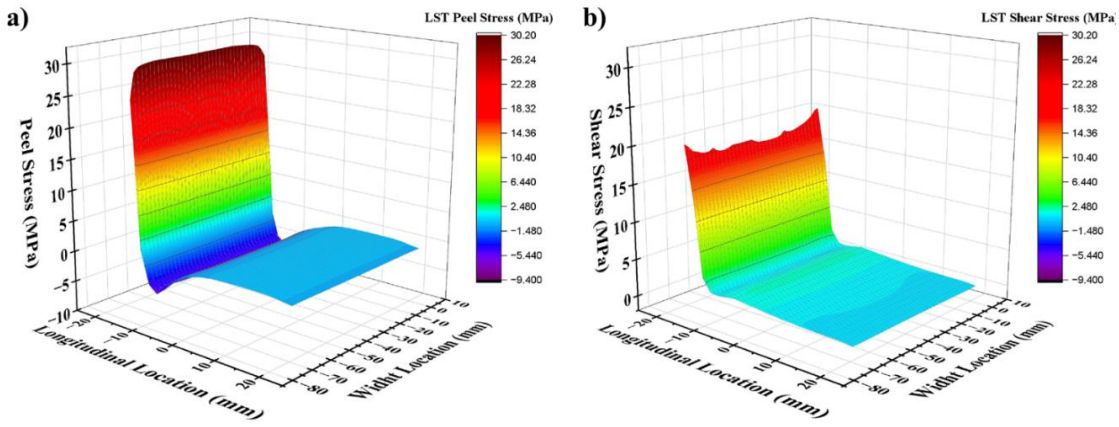

Figure 65. a) Peel and b) shear stress distributions for the SSJ specimens for the LST surface condition.

On top of that, as can be seen in Figure 66, the comparisons of the peel and shear stress values during the debonding time are indicated in order to understand the main mechanism behind the fracture during the loading in the SSJ test specimens. The stress-time comparisons set forth that, even though both maximum peel and shear stresses progressively increase over time, maximum peel stress values are always higher than maximum shear stress values up to the very end. Therefore, the main phenomenon behind the failure showed up as peel stresses, as expected. Yet, the behavior of the SSJ can be concluded as mix-mode debonding with peel stress-intensity fracture.

As an overall assessment, this mix-mode debonding with peel intensity fracture behavior mostly demonstrates the real-life skin-spar relation in the airplane wing-box during a casual flight; because the contact region of the skin and spar parts withstand mostly shear but also peel stresses during a casual flight. Therefore, including an investigation of the shear intensity behavior with the SLJ coupons, the examining the peel intensity behavior with an element level test setup also set light to adhesively bonding behavior of an aerospace structure, on top of that, provided a more detailed discussion in order for the accuracy and practicality of the presented FEA method.

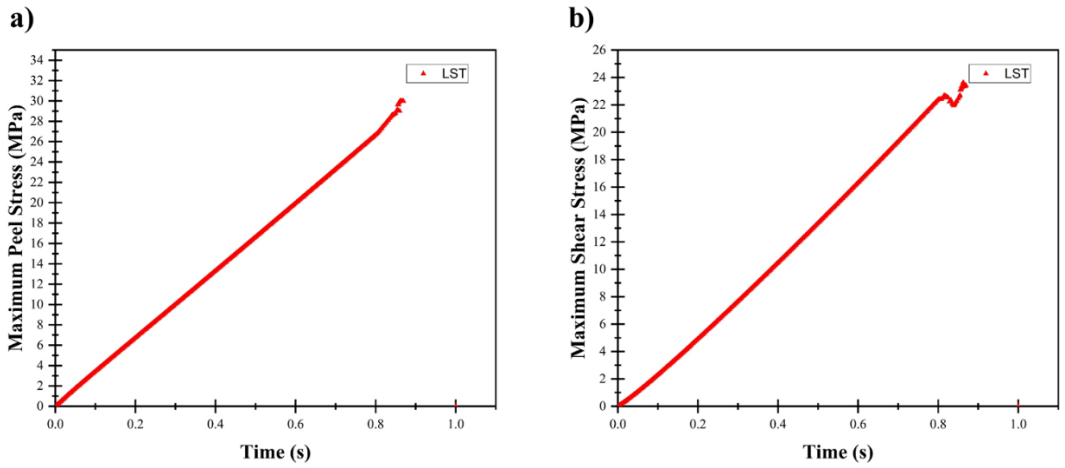

Figure 66. Stress-time graph of the SSJ specimens for a) peel, and b) shear stress for the LST conditions.

The experimental and numerical comparison of the average peel strengths for the LSUT and LST configurations are given in Figure 67.

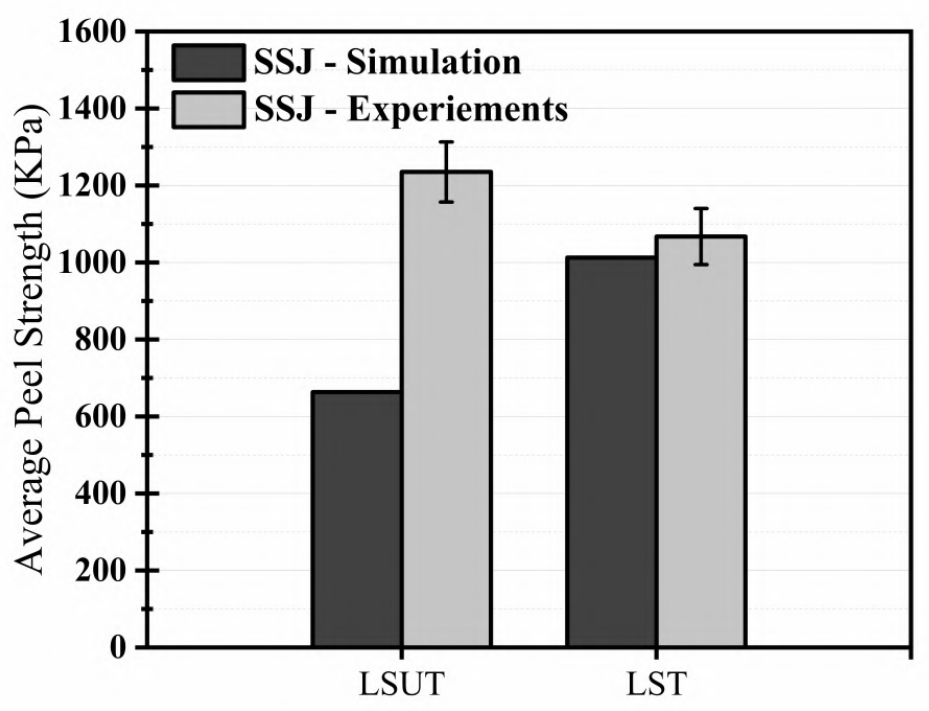

Figure 67. Average shear strength comparisons between the numerical and experimental results for the SSJ specimens for both LSUT and LST surface conditions.

Overall, employing the CZM technique with bilinear TSL is a reasonable method for simulating and CFRP aerospace structure at the element level. Nevertheless, in order to perform accurate FEA instead of obtaining from the literature or estimating by using mechanical property datasheets, one must carry out a special characterization work on the work-specific specimens to dedicate accurate CZM parameters.

CHAPTER 7

CONCLUSION AND FUTURE WORKS

7.1. Conclusion

The main objective of this thesis is to simulate the adhesive bonding behavior of the CFRP aerospace structures, in particular, skin-spar relation in a wing-box assembly, under the laser surface treated and untreated configurations. In this study, the mode I and mode II behavior of the adhesively bonded joints in different surface configurations were characterized in the continuation of the workflow, which started with experimentally observing the effects of laser application on the behavior of the adhesively bonded composite structures. Thereafter, the values obtained as a result of the characterization tests were evaluated in a meaningful frame and transformed into parameters that are used to compensate for the adhesive bonding behavior. In this way, the effect of laser surface treatment on the behavior of composite parts was transferred to the simulation, and the ability to perform numerical analysis on the relevant parts using the FEA method was provided. After providing this capability, FEA models were created by adhering to the real-life test coupon's properties, such as size, fiber orientation, stacking sequences, adhesive thickness, boundary conditions, and then numerical analyzes were carried out. As a result of these numerical analyses, the compatibility and accuracy of the presented method, which consisted of a combination of characterization and numerical analysis stages, were evaluated by comparing the experimental and simulation results.

Subsequently, as a result of the numerical analysis performed, the force-displacement graphs, cohesive area stress distributions and maximum strength values, as well as the onset and progression of the damage were revealed, and thus the main factors causing the fracture and the changes in the fracture behavior as a result of the surface treatment were numerically discussed. Moreover, the above-mentioned experimental and numerical analysis processes were performed on bonded CFRP composite parts at both the coupon level and the element level. In this way, the accuracy of the method applied

for tests at different levels is discussed, and the appropriate and unsuitable aspects of this method for different aircraft parts or full-scale test setups are set forth.

As the general conclusion of the numerical work, the behaviors of adhesively bonded CFRP composite structures were examined - considering the effects of the laser surface treatment application – by means of performing 3-D FEA of both SLJ and SSJ geometry in the case of LSUT and LST surface conditions. In order to simulate bonding behavior, the CZM technique governed with the bilinear TSL together with static-structural simulations, which were carried out with considering nonlinearities on the orthotropic materials to predict the load-displacement curves, stress distribution and details behind the failure for not only coupon but element level specimens.

As an integral component of the applied FEA method, a bonding characterization study was carried out for both mode I and mode II behavior in order to obtain proper CZM parameters for the laser surface treated and untreated surface configurations. A special strategy was utilized in order to obtain CZM parameters; this study follows an amalgamation of experimental and numerical methods to identify CZM parameters for mode I and mode II behavior. This is all to say, Critical Strain Energy Release Rate (G_C) values were evaluated through experimental DCB and ENF tests, obeying and using the calculation in the corresponding ASTM standards. However, Maximum Cohesive Traction (T_{max}) values were estimated by means of the calibration procedure comparing numerical and experimental works via inverse fitting methodology, employing 2-D FEA of the DCB and ENF tests. The presented procedure is not a completely direct or inverse method; however, this work adopts a combination of inverse and direct methods to determine mode I and mode II CZM parameters.

As experimental works, adhesive bonded SLJ and SSJ test specimens with the laser surface treated and untreated configurations. While the SLJ test was executed according to the aforementioned ASTM standard, the SSJ test setup was designed and implemented specifically for this study in order to evaluate the peel intensity behavior of an aircraft skin-spar relation. On top of the main experiments, ENF and DCB tests were carried out during the characterization study. Overall, DCB and ENF test results indicate performance improvement in both mode I and mode II behavior earned thanks to laser surface treatment. Similar enhancements were observed in the SLJ test while evaluating shear intensity mix-mode debonding behavior. Unlike other test setups, there is no considerable performance improvement observed in the SSJ test setup. The main reason

behind this is that the cohesive fracture formation occuring on the bonding surfaces and, obviously, the out-of-autoclave manufacturing technique used for the joint SSJ test specimens. On the whole, by executing laser surface treatment, around 63% and 23% performance improvements were provided for adhesively bonded mode I and mode II behavior, respectively. Additionally, 65% maximum strength enhancement was provided on the secondary bonded SLJ specimens; however, peel strength values for SSJ specimens show that the laser surface treatment application did not positively affect maximum strength magnitudes.

Above all, compatibility analysis between simulation and experimental test results indicates that the presented FEA methodology shows an average 15% accuracy for laser surface treated and untreated surface conditions, on top of that, in coupon and element level analysis; yet, the same success, unfortunately, were not provided for laser surface untreated SSJ specimens. The unsuccess behind this is mainly the manufacturing technique differences between the characterization and SSJ test specimens. Moreover, principal influences behind the failure were predicted by means of introducing both peel and shear stress distributions during the test time. The stress distributions in the case of laser surface treatment for both SLJ and SSJ test setups, too, were presented in order to analyze debonding behavior better and set forth the inhomogeneous stress distributions, which cause mix-mode debonding. With regard to this, this thesis exhibits a successful FEA methodology in order to analyze adhesively bonded aerospace structures, in particular, aircraft joining components. In other words, through combining the aforementioned characterization and FEA methods, one can effectively predict the failure strength and mechanism for the adhesive bonded composite structures, even at different level configurations and laser-surface application cases. Incidentally, it should be noted that, in addition to the success of the applied FEA method, the applied characterization method allowed easier and more accurate parameter determination than the studies seen in the literature, ensuring mutual operation of direct and inverse methods. Notwithstanding, as luck of success in the present FEA methodology, in cases where the cohesive fracture is seen, the method applied is interrupted correctly, and as a suggestion, if it is desired to develop a more precise and suitable analysis for all conditions, the analysis should be equipped with the ability to observe cohesive fracture.

7.2. Future Works

Utilizing the adhesive bonding technique for the joining of the aircraft components offers great potential to avoid the disadvantages of mechanical fastening, in addition, it provides many indispensable advantages. Therefore, adhesive joints will play an active role in not only aircraft but many aerospace applications. In addition to improving the bonding performance of these structures, which are composed of composite components, it is indispensable to simulate this behavior in a computer environment. However, it is clear that the methods currently being performed for finite element analysis of adhesively bonded joints need to be improved. As a result of the development in computer technologies and the increase in the use of adhesive joints, it is inevitable that more advanced methods will emerge.

From a research point of view, there are certain gaps to be filled in terms of better analysis for the adhesively bonded composite structures:

- Debonding behavior between the plies of the CFRP adherents should be implemented in simulation in order to dedicate failure modes.
- Chaotic crack initiation and progression within the adhesive material should be included in the analysis in order to observe cohesive fracture.
- The applicability of the CZM method in different scales needs to be improved.
- The bonding behavior of the CFRP adherents under fatigue loads should be examined, employing the CZM technique.
- The application of the laser surface treatment to create different patterns and the performance differences obtained as a result should be examined, on top of that, the optimum laser pattern should be optimized using artificial intelligence (AI) and machine learning (ML) methods.

BIBLIOGRAPHY

(1) Hsissou, R.; Seghiri, R.; Benzekri, Z.; Hilali, M.; Rafik, M.; Elharfi, A. Polymer Composite Materials: A Comprehensive Review. Compos. Struct. **2021**, 262, 113640. https://doi.org/10.1016/J.COMPSTRUCT.2021.113640.

(2) T. W. Clyne, D. Hull - An Introduction to Composite Materials." Google Books, books.google.com.tr/books/about/An_Introduction_to_Composite_Materials.html ?id=4oKWDwAAQBAJ&redir_esc=y.

(3) Campbell, F. C. Introduction to Composite Materials. Struct. Compos. Mater. **2010**, 1–29. https://doi.org/10.31399/ASM.TB.SCM.T52870001.

(4) Arif, M.; Asif, M.; Ahmed, D. Advanced Composite Material for Aerospace Application-a Review. Int. J. Eng. Manuf. Sci. **2017**, 7 (2), 393–409.

(5) Aamir, M.; Tolouei-Rad, M.; Giasin, K.; Nosrati, A. Recent Advances in Drilling of Carbon Fiber–Reinforced Polymers for Aerospace Applications: A Review. Int. J. Adv. Manuf. Technol. **2019**, 105 (5–6), 2289–2308. https://doi.org/10.1007/S00170-019-04348-Z/FIGURES/14.

(6) Mangalgiri, P. D. Composite Materials for Aerospace Applications. Bull. Mater. Sci. **1999**, 22 (3), 657–664. https://doi.org/10.1007/BF02749982/METRICS.

(7) Soutis, C. Carbon Fiber Reinforced Plastics in Aircraft Construction. Mater. Sci. Eng. A **2005**, 412 (1–2), 171–176. https://doi.org/10.1016/J.MSEA.2005.08.064.

(8) Brockmann, W.; Geiß, P. L.; Klingen, J.; Schröder, B. Adhesive Bonding: Materials, Applications and Technology. **2008**.

(9) Adams, R. Adhesive Bonding: Science, Technology and Applications. **2021**.

(10) Aerospace, D. D.-H. P. M. in; 1995, undefined. Adhesive Bonding for Aerospace Applications. Springer.

(11) Ebnesajjad, S.; Ebnesajjad, C. Surface Treatment of Materials for Adhesive Bonding. **2013**.

(12) Schonhorn, H.; Polymer, R. H.-J. of A.; 1967, undefined. Surface Treatment of Polymers for Adhesive Bonding. Wiley Online Libr. **1967**, 11 (8), 1461–1474. https://doi.org/10.1002/app.1967.070110809.

(13) Marques, Ana C., et al. "Review on Adhesives and Surface Treatments for Structural Applications: Recent Developments on Sustainability and Implementation for Metal and Composite Substrates." Materials, vol. 13, no. 24, MDPI, Dec. 2020, p. 5590. https://doi.org/10.3390/ma13245590.adhesives, J. W.-I. journal of adhesion and; 1993, undefined. Treatment of Composite Surfaces for Adhesive Bonding. Elsevier.

(14) Park, S. Y.; Choi, W. J.; Choi, H. S.; Kwon, H.; Kim, S. H. Recent Trends in Surface Treatment Technologies for Airframe Adhesive Bonding Processing: A Review (1995–2008). http://dx.doi.org/10.1080/00218460903418345 **2010**, 86 (2), 192–221. https://doi.org/10.1080/00218460903418345.

(15) Çoban, O.; Akman, E.; Bora, M. Ö.; Genc Oztoprak, B.; Demir, A. Laser Surface Treatment of CFRP Composites for a Better Adhesive Bonding Owing to the Mechanical Interlocking Mechanism. Polym. Compos. **2019**, 40 (9), 3611–3622. https://doi.org/10.1002/PC.25224.

(16) Lim, S.; Cheon, J.; and, M. K.-C. P. A. A. S.; 2020, undefined. Effect of Laser Surface Treatments on a Thermoplastic PA 6/Carbon Composite to Enhance the Bonding Strength. Elsevier.

(17) Davies, P.; Sohier, L.; Cognard, J.; adhesives, A. B.-… adhesion and; 2009, undefined. Influence of Adhesive Bond Line Thickness on Joint Strength. Elsevier.

(18) Ghumatkar, A.; Budhe, S.; … R. S.-… A. J. of; 2016, undefined. Influence of Adherend Surface Roughness on the Adhesive Bond Strength. SciELO Bras.

(19) Dillard, D. Advances in Structural Adhesive Bonding. **2010**.

(20) Chen, D.; Cheng, S. An Analysis of Adhesive-Bonded Single-Lap Joints. **1983**.

(21) Adhesives, X. H.-I. J. of A. and; 2011, undefined. A Review of Finite Element Analysis of Adhesively Bonded Joints. Elsevier.

(22) Li, G.; Lee-Sullivan, P.; Structures, R. T.-C.; 1999, undefined. Nonlinear Finite Element Analysis of Stress and Strain Distributions across the Adhesive Thickness in Composite Single-Lap Joints. Elsevier.

(23) Thakare, N.; of, A. D.-S. I. J.; 2015, undefined. A Review on Design and Analysis of Adhesive Bonded Joint by Finite Element Analysis. pdfs.semanticscholar.org **2015**, 2.

(24) Campilho, R. D. S. G.; Banea, M. D.; Neto, J. A. B. P.; Da Silva, L. F. M. Modelling of Single-Lap Joints Using Cohesive Zone Models: Effect of the Cohesive Parameters on the Output of the Simulations. J. Adhes. **2012**, 88 (4–6), 513–533. https://doi.org/10.1080/00218464.2012.660834.

(25) Khoramishad, H.; Crocombe, A.; … K. K.-I. J. of; 2010, undefined. Predicting Fatigue Damage in Adhesively Bonded Joints Using a Cohesive Zone Model. Elsevier.

(26) Li, S.; Thouless, M.; Waas, A.; … J. S.-E. fracture; 2006, undefined. Mixed-Mode Cohesive-Zone Models for Fracture of an Adhesively Bonded Polymer–Matrix Composite. Elsevier.

(27) Campilho, R.; Banea, M.; Adhesion, J. N.-… J. of; 2012, undefined. Modelling of Single-Lap Joints Using Cohesive Zone Models: Effect of the Cohesive Parameters on the Output of the Simulations. Taylor Fr.

(28) Jr, F. C. Manufacturing Technology for Aerospace Structural Materials. **2011**.

(29) Pantelakis, S.; Physics, K. T.-S. C.; and, M.; 2014, undefined. Adhesive Bonding of Composite Aircraft Structures: Challenges and Recent Developments. Springer **2014**, 57 (1), 2–11. https://doi.org/10.1007/s11433-013-5274-3.

(30) Wegman, R.; Twisk, J. Van. Surface Preparation Techniques for Adhesive Bonding. **2012**.

(31) Yudhanto, A.; Alfano, M.; Science, G. L.-C. P. A. A.; 2021, undefined. Surface Preparation Strategies in Secondary Bonded Thermoset-Based Composite Materials: A Review. Elsevier.

(32) da Silva, L. F. M.; Campilho, R. D. S. G. Design of Adhesively-Bonded Composite Joints. Fatigue Fract. Adhes. Compos. Joints **2015**, 43–71. https://doi.org/10.1016/B978-0-85709-806-1.00002-1.

(33) Tserpes, K. Adhesive Bonding of Aircraft Structures. Revolutionizing Aircr. Mater. Process. **2020**, 337–357. https://doi.org/10.1007/978-3-030-35346-9_12.

(34) Transactions, L. H.-S.-S.; 1980, undefined. Adhesive Bonding of Aircraft Primary Structures. JSTOR.

(35) Pantelakis, S.; Physics, K. T.-S. C.; and, M.; 2014, undefined. Adhesive Bonding of Composite Aircraft Structures: Challenges and Recent Developments. Springer **2014**, 57 (1), 2–11. https://doi.org/10.1007/s11433-013-5274-3.

(36) technology, L. H.-S.-H. of adhesion; 2011, undefined. Adhesively Bonded Joints in Aircraft Structures. infona.pl.

(37) Hamm, K. R.; Price, D. R.; Imtiaz, K. S.; Raju, I. S. Revisiting Building-Block Approaches for Structures. AIAA Sci. Technol. Forum Expo. AIAA SciTech Forum 2022 **2022**. https://doi.org/10.2514/6.2022-1900.

(38) Silva, L. Da; Dillard, D.; Blackman, B.; Adams, R. Testing Adhesive Joints: Best Practices. **2012**.

(39) bonding, B. D.-A. in structural adhesive; 2010, undefined. Developments in Testing Adhesive Joints. Elsevier.

(40) Kupski, J.; Structures, S. D. F.-C.; 2021, undefined. Design of Adhesively Bonded Lap Joints with Laminated CFRP Adherends: Review, Challenges and New Opportunities for Aerospace Structures. Elsevier.

(41) Ribeiro, T.; Campilho, R.; Silva, L. da; Structures, L. G.-C.; 2016, undefined. Damage Analysis of Composite–Aluminium Adhesively-Bonded Single-Lap Joints. Elsevier.

(42) Zhou, L.; Zhang, D.; Zhao, L.; Zhou, X.; Zhang, J.; Design, F. L.-M. &; 2016, undefined. Design and Analysis of a Novel Bolted Composite π Joint under Bending Load. Elsevier.

(43) Budhe, S.; Banea, M. D.; de Barros, S.; da Silva, L. F. M. An Updated Review of Adhesively Bonded Joints in Composite Materials. Int. J. Adhes. Adhes. **2017**, 72, 30–42. https://doi.org/10.1016/J.IJADHADH.2016.10.010.

(44) Banea, M. D.; M Da Silva, L. F. Adhesively Bonded Joints in Composite Materials: An Overview. **2009**. https://doi.org/10.1243/14644207JMDA219.

(45) Kim, K.; Yoo, J.; Yi, Y.; structures, C. K.-C.; 2006, undefined. Failure Mode and Strength of Uni-Directional Composite Single Lap Bonded Joints with Different Bonding Methods. Elsevier.

(46) Mohan, J.; Ivanković, A.; and, N. M.-I. J. of A.; 2014, undefined. Mode I Fracture Toughness of Co-Cured and Secondary Bonded Composite Joints. Elsevier.

(47) Hasan, Z.; Rader, J.; Olson, A.; Turpin, D.; … R. S. O.-C. P. B.; 2019, undefined. Design, Analysis and Fabrication of Thick Co-Cured Wing Structures. Elsevier.

(48) Encinas, N.; Oakley, B.; Adhesives, M. B.-… and; 2014, undefined. Surface Modification of Aircraft Used Composites for Adhesive Bonding. Elsevier.

(49) Preparation, S. E.-H. of A. and S.; 2011, undefined. Surface Preparation of Thermoplastics, Thermosets, and Elastomers. Elsevier.

(50) Liston, E. M. Plasma Treatment for Improved Bonding: A Review. J. Adhes. **1989**, 30 (1–4), 199–218. https://doi.org/10.1080/00218468908048206.

(51) Awaja, F.; Gilbert, M.; Kelly, G.; Fox, B.; science, P. P.-P. in polymer; 2009, undefined. Adhesion of Polymers. Elsevier.

(52) Marques, A. C.; Mocanu, A.; Tomi´ctomi´c, N. Z.; Balos, S.; Stammen, E.; Lundevall, A.; Abrahami, S. T.; Günther, R.; De Kok, J. M. M.; Teixeira De Freitas, S. Review on Adhesives and Surface Treatments for Structural Applications: Recent Developments on Sustainability and Implementation for Metal and Composite. mdpi.com **2020**, 13, 5590. https://doi.org/10.3390/ma13245590.

(53) Fischer, F.; Kreling, S.; Jäschke, P.; Frauenhofer, M.; Kracht, D.; Dilger, K. Laser Surface Pre-Treatment of CFRP for Adhesive Bonding in Consideration of the Absorption Behaviour. J. Adhes. **2012**, 88 (4–6), 350–363. https://doi.org/10.1080/00218464.2012.660042.

(54) Liu, L.; Liu, X.; Kong, L.; Wang, M.; Hu, P.; Wang, D. Effect of Laser Surface Treatment on Surface and Bonding Properties of Carbon Fiber Reinforced Composites. Int. J. Mater. Form. **2020**, 13 (6), 885–895. https://doi.org/10.1007/S12289-019-01509-Z.

(55) Çoban, O.; Akman, E.; … M. B.-P.; 2019, undefined. Laser Surface Treatment of CFRP Composites for a Better Adhesive Bonding Owing to the Mechanical Interlocking Mechanism. Wiley Online Libr.

(56) Oliveira, V.; Sharma, S.; … M. D. M.-O. and L. in; 2017, undefined. Surface Treatment of CFRP Composites Using Femtosecond Laser Radiation. Elsevier.

(57) Zhan, X.; Li, Y.; Gao, C.; Wang, H.; Technology, Y. Y.-O. & L.; 2018, undefined. Effect of Infrared Laser Surface Treatment on the Microstructure and Properties of Adhesively CFRP Bonded Joints. Elsevier.

(58) Li, Y.; Zhan, X.; Gao, C.; Wang, H.; of, Y. Y.-T. I. J.; 2019, undefined. Comparative Study of Infrared Laser Surface Treatment and Ultraviolet Laser Surface Treatment of CFRP Laminates. Springer **2019**, 102 (9–12), 4059–4071. https://doi.org/10.1007/s00170-019-03368-z.

(59) Kartik Nemani, S.; Kishore Annavarapu, R.; Mohammadian, B.; Raiyan, A.; Heil, J.; Ashraful Haque, M.; Abdelaal, A.; Sojoudi, H.; Nemani, S. K.; Annavarapu, R. K.; Mohammadian, B.; Raiyan, A.; Heil, J.; Haque, M. A.; Abdelaal, A.; Sojoudi, H. Surface Modification of Polymers: Methods and Applications. Wiley Online Libr. **2018**, 5 (24). https://doi.org/10.1002/admi.201801247.

(60) Zhan, X.; Li, Y.; Gao, C.; Wang, H.; Technology, Y. Y.-O. & L.; 2018, undefined. Effect of Infrared Laser Surface Treatment on the Microstructure and Properties of Adhesively CFRP Bonded Joints. Elsevier.

(61) Li, Y.; Zhan, X.; Gao, C.; Wang, H.; of, Y. Y.-T. I. J.; 2019, undefined. Comparative Study of Infrared Laser Surface Treatment and Ultraviolet Laser Surface Treatment of CFRP Laminates. Springer **2019**, 102 (9–12), 4059–4071. https://doi.org/10.1007/s00170-019-03368-z.

(62) Harder, S.; Schmutzler, H.; … P. H.-C. P. A.; 2019, undefined. Effect of Infrared Laser Surface Treatment on the Morphology and Adhesive Properties of Scarfed CFRP Surfaces. Elsevier.

(63) Fischer, F.; Kreling, S.; Jäschke, P.; Frauenhofer, M.; Kracht, D.; Dilger, & K. Laser Surface Pre-Treatment of CFRP for Adhesive Bonding in Consideration of the Absorption Behaviour. Taylor Fr. **2012**, 88 (4–6), 350–363. https://doi.org/10.1080/00218464.2012.660042.

(64) D5573 Standard Practice for Classifying Failure Modes in Fiber-Reinforced-Plastic (FRP) Joints. https://www.astm.org/d5573-99r19.html (accessed 2023-06-01).

(65) Liu, X.; Shao, X.; Li, Q.; Engineering, G. S.-C. P. B.; 2019, undefined. Failure Mechanisms in Carbon Fiber Reinforced Plastics (CFRP)/Aluminum (Al) Adhesive Bonds Subjected to Low-Velocity Transverse Pre-Impact Following By. Elsevier.

(66) da Silva, L. F. M.; Campilho, R. D. S. G. Advances in Numerical Modelling of Adhesive Joints. SpringerBriefs Appl. Sci. Technol. **2012**, No. 9783642236075, 1–93. https://doi.org/10.1007/978-3-642-23608-2_1/COVER/.

(67) Adams, R.; Adams, R.; Comyn, J.; Wake, W.; Wake, W. Structural Adhesive Joints in Engineering. **1997**.

(68) schung, O. V.-L.; 1938, undefined. Die Nietkraftverteilung in Zugbeanspruchten Nietverbindungen Mit Konstanten Laschenquerschnitten. cir.nii.ac.jp.

(69) Adams, R.; analysis, N. P.-J. of strain; 1973, undefined. Effect of Poisson's Ratio Strains in Adherends on Stresses of an Idealized Lap Joint. journals.sagepub.com **2011**, 8 (2), 134–139. https://doi.org/10.1243/03093247V082134.

(70) Adams, R. D.; Peppiatt, n. a. Stress Analysis of Adhesive-Bonded Lap Joints. J. Strain Anal. Eng. Des. **1974**, 9 (3), 185–196. https://doi.org/10.1243/03093247V093185.

(71) Adams, R. D.; Peppiatt, N. A. Stress Analysis of Adhesive Bonded Tubular Lap Joints. J. Adhes. **1977**, 9 (1), 1–18. https://doi.org/10.1080/00218467708075095.

(72) Atkins, R. W.; Adams, R. D.; Harris, J. A.; Kinloch, A. J. Stress Analysis and Failure Properties of Carbon-Fibre-Reinforced-Plastic/Steel Double-Lap Joints. J. Adhes. **1986**, 20 (1), 29–53. https://doi.org/10.1080/00218468608073238.

(73) Banea, M. D.; Silva, L. F. M. da. Adhesively Bonded Joints in Composite Materials: An Overview: http://dx.doi.org/10.1243/14644207JMDA219 **2016**. https://doi.org/10.1243/14644207JMDA219.

(74) Banea, M. D.; da Silva, L. F. M.; Campilho, R. D. S. G. Principles of Adhesive Bonding. Join. Polym. Hybrid Struct. Princ. Appl. **2018**, 3–27. https://doi.org/10.1002/9781119429807.CH1.

(75) Adams, R.; Adams, R.; Comyn, J.; Wake, W.; Wake, W. Structural Adhesive Joints in Engineering. **1997**.

(76) Lee, S. J.; Lee, D. G. Development of a Failure Model for the Adhesively Bonded Tubular Single Lap Joint. J. Adhes. **1992**, 40 (1), 1–14. https://doi.org/10.1080/00218469208030467.

(77) Silva, L. Da; Carbas, R.; … G. C.-I. J. of; 2009, undefined. Effect of Material, Geometry, Surface Treatment and Environment on the Shear Strength of Single Lap Joints. Elsevier.

(78) Silva, L. da; Neves, P. das; … R. A.-I. J. of; 2009, undefined. Analytical Models of Adhesively Bonded Joints—Part I: Literature Survey. Elsevier.

(79) Silva, L. da; Neves, P. das; … R. A.-I. J. of; 2009, undefined. Analytical Models of Adhesively Bonded Joints—Part II: Comparative Study. Elsevier.

(80) Harris, J.; adhesives, R. A.-I. journal of adhesion and; 1984, undefined. Strength Prediction of Bonded Single Lap Joints by Non-Linear Finite Element Methods. Elsevier.

(81) Hart-Smith, L. Adhesive-Bonded Single-Lap Joints. **1973**.

(82) Zhao, X.; Adams, R. D.; Da Silva, L. F. M. Single Lap Joints with Rounded Adherend Corners: Stress and Strain Analysis. J. Adhes. Sci. Technol. **2011**, 25 (8), 819–836. https://doi.org/10.1163/016942410X520871.

(83) Zhao, X.; Adams, R. D.; Da Silva, L. F. M. Single Lap Joints with Rounded Adherend Corners: Experimental Results and Strength Prediction. J. Adhes. Sci. Technol. **2011**, 25 (8), 837–856. https://doi.org/10.1163/016942410X520880.

(84) Chaves, F. J. P.; Da Silva, L. F. M.; De Moura, M. F. S. F.; Dillard, D. A.; Esteves, V. H. C. Fracture Mechanics Tests in Adhesively Bonded Joints: A Literature Review. J. Adhes. **2014**, 90 (12), 955–992. https://doi.org/10.1080/00218464.2013.859075.

(85) da Silva, L. F. M.; Campilho, R. D. S. G. Advances in Numerical Modelling of Adhesive Joints. SpringerBriefs Appl. Sci. Technol. **2012**, No. 9783642236075, 1–93. https://doi.org/10.1007/978-3-642-23608-2_1.

(86) Griffits, A. A. The Phenomena of Rupture and Flow in Solids. Masinovedenie **1995**, No. 1, 9–14. https://doi.org/10.1098/RSTA.1921.0006.

(87) Irwin, G. Analysis of Stresses and Strains near the End of a Crack Traversing a Plate. **1957**.

(88) Erdogan, F. Fracture Mechanics. Int. J. Solids Struct. **2000**, 37 (1–2), 171–183. https://doi.org/10.1016/S0020-7683(99)00086-4.

(89) Rice, J. R. A Path Independent Integral and the Approximate Analysis of Strain Concentration by Notches and Cracks. **1968**.

(90) Rybicki, E.; mechanics, M. K.-E. fracture; 1977, undefined. A Finite Element Calculation of Stress Intensity Factors by a Modified Crack Closure Integral. Elsevier.

(91) Wu, H.; Settgast, R. R.; Fu, P.; Morris, J. P. An Enhanced Virtual Crack Closure Technique for Stress Intensity Factor Calculation along Arbitrary Crack Fronts and the Application in Hydraulic Fracturing Simulation. Rock Mech. Rock Eng. **2021**, 54 (6), 2943–2957. https://doi.org/10.1007/S00603-021-02428-9.

(92) Machado, R. M. D.; Campilho, R. D. S. G.; Rocha, R. J. B. Extended Finite Element Modelling of Aluminium Stepped-Adhesive Joints. J. Adhes. **2019**, 95 (5–7), 450–473. https://doi.org/10.1080/00218464.2018.1548966.

(93) Campilho, R.; Banea, M.; Adhesives, A. P.-… and; 2011, undefined. Strength Prediction of Single-and Double-Lap Joints by Standard and Extended Finite Element Modelling. Elsevier.

(94) Moës, N.; Dolbow, J.; for, T. B.-I. journal; 1999, undefined. A Finite Element Method for Crack Growth without Remeshing. Wiley Online Libr.

(95) mechanics, G. B.-A. in applied; 1962, undefined. The Mathematical Theory of Equilibrium Cracks in Brittle Fracture. Elsevier.

(96) Solids, D. D.-J. of the M. and P. of; 1960, undefined. Yielding of Steel Sheets Containing Slits. Elsevier.

(97) Elices, M.; Guinea, G.; Gomez, J.; mechanics, J. P.-E. fracture; 2002, undefined. The Cohesive Zone Model: Advantages, Limitations and Challenges. Elsevier.

(98) Workbench User's Guide. https://ansyshelp.ansys.com/account/secured?returnurl=/Views/Secured/corp/v221/en/wb2_help/wb2_help.html%23wb2_help (accessed 2023-06-01).

(99) Campilho, R. D. S. G.; Banea, M. D.; Neto, J. A. B. P.; Da Silva, L. F. M. Modelling Adhesive Joints with Cohesive Zone Models: Effect of the Cohesive Law Shape of the Adhesive Layer. Int. J. Adhes. Adhes. **2013**, 44, 48–56. https://doi.org/10.1016/J.IJADHADH.2013.02.006.

(100) Zhang, J.; Wang, J.; Yuan, Z.; Adhesives, H. J.-J. of A. and; 2018, undefined. Effect of the Cohesive Law Shape on the Modelling of Adhesive Joints Bonded with Brittle and Ductile Adhesives. Elsevier.

(101) Ribeiro, T.; Campilho, R.; Silva, L. da; Structures, L. G.-C.; 2016, undefined. Damage Analysis of Composite–Aluminium Adhesively-Bonded Single-Lap Joints. Elsevier.

(102) Campilho, R.; Banea, M.; Adhesives, A. P.-… and; 2011, undefined. Strength Prediction of Single-and Double-Lap Joints by Standard and Extended Finite Element Modelling. Elsevier.

(103) Li, S.; Thouless, M.; Waas, A.; … J. S.-E. fracture; 2006, undefined. Mixed-Mode Cohesive-Zone Models for Fracture of an Adhesively Bonded Polymer–Matrix Composite. Elsevier.

(104) Li, S.; Thouless, M.; Waas, A.; … J. S.-I. J. of; 2006, undefined. Competing Failure Mechanisms in Mixed-Mode Fracture of an Adhesively Bonded Polymer-Matrix Composite. Elsevier.

(105) Blackman, B. R. K.; Hadavinia, H.; Kinloch, A. J.; Williams, J. G. The Use of a Cohesive Zone Model to Study the Fracture of Fibre Composites and Adhesively-Bonded Joints. Int. J. Fract. **2003**, 119 (1), 25–46. https://doi.org/10.1023/A:1023998013255.

(106) Liljedahl, C. D. M.; Crocombe, A. D.; Wahab, M. A.; Ashcroft, I. A. Damage Modelling of Adhesively Bonded Joints. Int. J. Fract. **2006**, 141 (1–2), 147–161. https://doi.org/10.1007/S10704-006-0072-9.

(107) Moura, M. De; Gonçalves, J.; Adhesives, J. C.-… adhesion and; 2008, undefined. Cohesive and Continuum Mixed-Mode Damage Models Applied to the Simulation of the Mechanical Behaviour of Bonded Joints. Elsevier.

(108) Diaz, J.; Romera, L.; Hernandez, S.; of, A. B.-I. J.; 2010, undefined. Benchmarking of Three-Dimensional Finite Element Models of CFRP Single-Lap Bonded Joints. Elsevier.

(109) Sun, L.; Li, C.; Tie, Y.; Hou, Y.; and, Y. D.-I. J. of A.; 2019, undefined. Experimental and Numerical Investigations of Adhesively Bonded CFRP Single-Lap Joints Subjected to Tensile Loads. Elsevier.

(110) Banea, M.; of, L. da S.-P. of the I.; 2009, undefined. Adhesively Bonded Joints in Composite Materials: An Overview. journals.sagepub.com **2009**, 223 (1), 1–18. https://doi.org/10.1243/14644207JMDA219.

(111) Sadeghi, M.; Gabener, A.; … J. Z.-I. J. of; 2020, undefined. Failure Load Prediction of Adhesively Bonded Single Lap Joints by Using Various FEM Techniques. Elsevier.

(112) Silva, D. F. O.; Campilho, R. D. S. G.; Silva, F. J. G.; Carvalho, U. T. F. Application a Direct/Cohesive Zone Method for the Evaluation of Scarf Adhesive Joints. Appl. Adhes. Sci. https://doi.org/10.1186/s40563-018-0115-2.

(113) Allen, D. H.; Searcy, C. R. Micromechanical Model for a Viscoelastic Cohesive Zone. Int. J. Fract. **2001**, 107 (2), 159–176. https://doi.org/10.1023/A:1007693116116.

(114) Xie, D.; mechanics, A. W.-E. fracture; 2006, undefined. Discrete Cohesive Zone Model for Mixed-Mode Fracture Using Finite Element Analysis. Elsevier.

(115) Li, S.; Thouless, M.; Waas, A.; Technology, J. S.-… S. and; 2005, undefined. Use of a Cohesive-Zone Model to Analyze the Fracture of a Fiber-Reinforced Polymer–Matrix Composite. Elsevier.

(116) Yang, B.; Mall, S.; and, K. R.-C.-I. J. of solids; 2001, undefined. A Cohesive Zone Model for Fatigue Crack Growth in Quasibrittle Materials. Elsevier.

(117) Baney, J.; technology, C. H.-J. of adhesion science and; 1997, undefined. A Cohesive Zone Model for the Adhesion of Cylinders. Taylor Fr. **1997**, 11 (3), 393–406. https://doi.org/10.1163/156856197X00778.

(118) Song, S.; Paulino, G.; Mechanics, W. B.-E. F.; 2006, undefined. A Bilinear Cohesive Zone Model Tailored for Fracture of Asphalt Concrete Considering Viscoelastic Bulk Material. Elsevier.

(119) Khoramishad, H.; Crocombe, A.; … K. K.-I. J. of; 2010, undefined. Predicting Fatigue Damage in Adhesively Bonded Joints Using a Cohesive Zone Model. Elsevier.

(120) Sockalingam, S.; Dey, M.; … J. G. J.-C. P. A.; 2014, undefined. Finite Element Analysis of the Microdroplet Test Method Using Cohesive Zone Model of the Fiber/Matrix Interface. Elsevier.

(121) Sorrentino, L.; Marfia, S.; Parodo, G.; Sacco, E. Laser Treatment Surface: An Innovative Method to Increase the Adhesive Bonding of ENF Joints in CFRP. Compos. Struct. **2020**, 233, 111638. https://doi.org/10.1016/J.COMPSTRUCT.2019.111638.

(122) Leone, C.; Genna, S. Effects of Surface Laser Treatment on Direct Co-Bonding Strength of CFRP Laminates. Compos. Struct. **2018**, 194, 240–251. https://doi.org/10.1016/j.compstruct.2018.03.096.

(123) (PDF) Laser surface preparation and bonding of aerospace structural composites. https://www.researchgate.net/publication/268383738_Laser_surface_preparation_and_bonding_of_aerospace_structural_composites (accessed 2021-07-02).

(124) Fischer, F.; Kreling, S.; Dilger, K. Surface Structuring of CFRP by Using Modern Excimer Laser Sources. In Physics Procedia; Elsevier B.V., 2012; Vol. 39, pp 154–160. https://doi.org/10.1016/j.phpro.2012.10.025.

(125) Sun, C.; Min, J.; Lin, J.; Wan, H.; Yang, S.; of, S. W.-I. J.; 2018, undefined. The Effect of Laser Ablation Treatment on the Chemistry, Morphology and Bonding Strength of CFRP Joints. Elsevier.

(126) Genna, S.; Leone, C.; … N. U.-P. E. &; 2017, undefined. Increasing Adhesive Bonding of Carbon Fiber Reinforced Thermoplastic Matrix by Laser Surface Treatment. Wiley Online Libr. **2017**, 57 (7), 685–692. https://doi.org/10.1002/pen.24577.

(127) İplikçi, H. Development of Joining Techniques for Carbon Fiber Based Polymer Matrix Composites. **2020**.

(128) Barisik, M.; Türkdo, C.; Martin, S.; Yeke, M.; Nuho, K.; Eseno, ozde; Tano, M.; Aktas, E.; Dehneliler, S.; Erdem, M. Effects of Nanosecond Laser Ablation Parameters on Surface Modification of Carbon Fiber Reinforced Polymer Composites. journals.sagepub.com **2023**, 2023 (0), 1–13. https://doi.org/10.1177/00219983231178892.

(129) Hexcel | Composite Materials and Structures. https://www.hexcel.com/ (accessed 2022-07-16).

(130) FM 300 | Solvay. https://www.solvay.com/en/product/fm-300 (accessed 2022-07-16).

(131) Gao, Y. F.; Bower, A. F. A Simple Technique for Avoiding Convergence Problems in Finite Element Simulations of Crack Nucleation and Growth on Cohesive Interfaces. Model. Simul. Mater. Sci. Eng. **2004**, 12 (3), 453. https://doi.org/10.1088/0965-0393/12/3/007.

(132) D5868 Standard Test Method for Lap Shear Adhesion for Fiber Reinforced Plastic (FRP) Bonding. https://www.astm.org/d5868-01r14.html (accessed 2023-06-01).

(133) Standard Test Method for Mode I Interlaminar Fracture Toughness of Unidirectional Fiber-Reinforced Polymer Matrix Composites. https://www.astm.org/standards/d5528 (accessed 2022-07-16).

(134) Standard Test Method for Determination of the Mode II Interlaminar Fracture Toughness of Unidirectional Fiber-Reinforced Polymer Matrix Composites. https://www.astm.org/d7905_d7905m-14.html (accessed 2022-07-16).

(135) Hamitouche, L.; Tarfaoui, M.; Vautrin, A. An Interface Debonding Law Subject to Viscous Regularization for Avoiding Instability: Application to the Delamination Problems. Eng. Fract. Mech. **2008**, 75 (10), 3084–3100. https://doi.org/10.1016/J.ENGFRACMECH.2007.12.014.

(136) Turon, A.; Dávila, C. G.; Camanho, P. P.; Costa, J. An Engineering Solution for Mesh Size Effects in the Simulation of Delamination Using Cohesive Zone Models. Eng. Fract. Mech. **2007**, 74 (10), 1665–1682. https://doi.org/10.1016/J.ENGFRACMECH.2006.08.025.

(137) Hillerborg, A.; Modéer, M.; Petersson, P. E. Analysis of Crack Formation and Crack Growth in Concrete by Means of Fracture Mechanics and Finite Elements. Cem. Concr. Res. **1976**, 6 (6), 773–781. https://doi.org/10.1016/0008-8846(76)90007-7.

(138) Mantzaroudis, V.; Computation, D. S.-; 2022, undefined. Cohesive Zone Model Modification Techniques According to the Mesh Size in Finite Element Models of Stiffened Panels with Debonding. mdpi.com **2022**. https://doi.org/10.3390/computation10010005.